Michela Romanini

Relaxation Dynamics in Disordered Systems

Universitat Politècnica
de Catalunya

RELAXATION DYNAMICS in DISORDERED SYSTEMS

Michela Romanini

Relaxation Dynamics

in

Disordered Systems

Michela Romanini

Supervisors:

Prof. Dr. Josep Lluís TAMARIT MUR

Prof. Dr. Maria DEL BARRIO CASADO

Barcelona, June 2015

PhD programme in Computational and Applied Physics

Departament de Física
i Enginyeria Nuclear
UNIVERSITAT POLITÈCNICA DE CATALUNYA

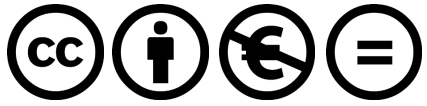

All the contents of this work are licensed under the Creative Commons
Attribution-NonCommercial-NoDerivs 4.0 International Licence
(CC BY-NC-ND 4.0).
For more informations visit
https://creativecommons.org/licenses/by-nc-nd/4.0/.

Cover designed by Martina Romanini (romanini.martina@yahoo.it)

A Roberto

A Leonardo

“ The true method of knowledge is experiment ”

- *William Blake* -

Abstract

The nature of the glass transition and of the glassy state is a fundamental and still unsolved problem of condensed matter physics. As stated by the Nobel prize winner P.W.Anderson in 1977: *"The deepest and most interesting unsolved problem in solid state theory is probably the nature of glass and the glass transition"*. Upon cooling, many systems do not crystallize right away, but rather they can be supercooled below the melting point without acquiring translational and orientational order. As the temperature of a supercooled liquid is lowered, the characteristic timescale of molecular motions, called relaxation time, increases, apparently diverging to infinity at some finite temperature. This divergence of the relaxation time leads to a non-equilibrium state of matter, called a glass, in which a liquid-like lack of order is combined with solid-like elastic properties. As the temperature is further lowered, the system finally reaches a state in which the relaxation time is comparable to the timescale of human experimentation τ_{exp}. This occurrence, which takes place at a temperature T_g, marks the experimental glass transition through which the dynamic disorder of the system freezes into a static disorder. The phase formed thereby is called "structural glass" and maintains the orientational and translational molecular disorder of the liquid phase from which it derives.

When the system is formed by molecular entities, a rich variety of

dynamic processes and phase behaviours appears. For example, another type of glassy behaviour arises when there is only a dynamic orientational disorder, rather than a full structural disorder. This is the case of the so-called "plastic-crystalline phase", which is intermediate between the (translationally and orientationally ordered) crystal and the (fully disordered) liquid phase. The molecular compounds which display translational order and at the same time orientational disorder are called orientationally disordered (OD) crystals or plastic crystals. In these compounds, the average molecular centres of mass form a regular crystalline lattice but the molecules undergo rotations that modify the molecular orientations; such orientational disorder can "freeze" upon cooling, yielding a so-called orientational glass.

In molecular materials forming structural or orientational glasses, the most important molecular dynamic process is the cooperative motion of the molecules, referred to as primary relaxation or α process, whose freezing marks the transition to the glass state characterized by static disorder (and in which the ergodicity is therefore broken). The main difference between orientational and structural glasses is that in the former the freezing involves exclusively the rotational degrees of freedom of the molecules, while in the latter all six molecular degrees of freedom (*i.e.*, both orientational and translational ones) are frozen. Orientational glasses are therefore systems with fewer degrees of freedom than structural glasses. This simplification, together with the fact that many OD phases are characterized by a crystal lattice with high symmetry, makes orientationally disordered phases a model playground to investigate the nature of the glass transition.

Molecular dynamic processes in glass formers other than the α relaxation are termed "secondary relaxations", and are usually characterized by

shorter relaxation time than the primary process associated with the glass transition. Secondary relaxations in OD phases may have different origins; for example, the constituent molecules generally exhibit intramolecular dynamics, such as conformational motions or vibrations of inter-atomic bonds; in other cases a single-molecule precursor of the α process is observed, called Johari-Goldstein relaxation. The spectral landscape of secondary relaxations of structural glass formers is further enriched by the existence of the so-called excess wing, that is, an excess dielectric loss on the high-frequency side of the α-relaxation process.

This thesis focuses on the dynamics of several pure compounds and binary mixtures forming structural glasses or plastic crystalline phases. We study the effect of pressure and temperature on the dynamics processes displayed by these systems, both primary and secondary. In particular, we present a comparative study between two structural glass formers (ternidazole and the mixture of m-fluoroaniline with m-xylene), a plastic mixed crystal (neopentyl alcohol mixed with neopenthyl glycol), and two materials displaying statistical orientational disorder (2-adamantanone and pentachloronitrobenzene). Concerning the orientationally disordered materials, in chapter 4 we focus on the dynamics of 2-adamantanone which displays a well defined crystalline metastable phase with statistical occupational disorder; in chapter 5 we deal with the OD mixed crystals formed by mixing $(CH_3)_3CCH_2OH$ (NPA) and $(CH_3)_3C(CH_2OH)_2$ (NPG), in which collective dynamics of the two-component mixed crystals are determined. In chapter 6 we concentrate on a OD crystal with fewer degrees of freedom than conventional plastic crystals, namely the layered solid phase of the hexasubstituted pentachloronitrobenzene derivative, in which we report the presence of a double primary (collective) relaxation which is related to the anisotropy of the system, and which gives rise to a

spectral landscape reminiscent of α relaxations characterized by an excess wing. In chapter 7 we study the suppression of the hydrogen-bond clusters in m-fluoroaniline upon mixing it with m-xylene, a similar aromatic compound which forms no H-bonds, in order to probe the microscopic mechanism behind the clustering phenomenon. Finally, in chapter 8 we study the ternidazole drug, which posses two distinct conformers (in the liquid and in the crystalline state), and we analyse the effects that the presence of these two conformers may have on the dynamics of the system and the kinetics of the recrystallization process from the supercooled state.

Contents

Chapter 1

INTRODUCTION

Ordinary matter is made of molecules held together by forces whose strength and range determine the bulk properties of condensed phases. A macroscopic manifestation of intermolecular forces is the fact that upon cooling a collection of molecules, their physical state changes from a gas to a liquid, and on further cooling there is another change of state from the liquid to a solid. At high temperature, the energy of attractive forces between molecules is small compared to their thermal energy and the molecules are in a state of constant motion and interact only through occasional collisions. As the temperature is reduced, attractive interactions between molecules become more and more important and, on colliding, pairs of molecules stay together longer and correlations between the motions of different molecules start to appear. When these correlations become more permanent, a new, dense phase appears, the liquid. In this phase the molecules do not occupy well-defined positions on a lattice, and the density is determined by the tension between the attractive part of the intermolecular potential, which tries to pack the molecules as closely as possible, and the repulsive part of the potential,

which imposes a minimum separation between them. The relative position of a molecule with respect to its neighbours varies on a characteristic time (called relaxation time) which depends on how the random thermal motion of the molecules is modified by intermolecular forces.

The relaxation time determines how easily the liquid will flow when a stress is applied, that is, it determines the viscosity of the liquid. Characteristic relaxation times for soft condensed matter are often in a range of values easily discernible to the human senses and the resulting phase appears to behave in a way that is neither entirely solid-like or liquid-like. Materials with such characteristics are called viscoelastic. As the temperature of the liquid is decreased further, the molecules starts to pack themselves together in a more regular way to avoid the tension between repulsive and attractive part of potential, reaching a higher density state. The liquid has crystallized, with each molecule occupying a specific location on a lattice. Upon cooling, many systems do not crystallize right away, but rather they can be supercooled below the melting point without acquiring translational and orientational order. As the temperature is lowered in the supercooled state, the relaxation time increases, apparently diverging to infinity at some finite temperature. This divergence of the relaxation time leads to a non-equilibrium state of matter, called a glass, in which a liquid-like lack of order is combined with solid-like elastic properties.

1.1 Glasses

The nature of the glass transition and of the glassy state is a fundamental and still unsolved problem of condensed matter physics [1–3]. As stated by the Nobel prize winner P.W.Anderson: *"The deepest and most*

interesting unsolved problem in solid state theory is probably the nature of glass and the glass transition" [1]. A glass may be defined simply as a non-crystalline solid. Glassy materials are omnipresent in our daily life and in classical technical applications (e.g. windows, optical components, containers) as well as in communication techniques (optical fibre) and medicine (bioactive implants). The range of materials that can form glasses is very wide. Examples of glasses are:

- Oxide glasses formed by oxides of elements from groups III, IV and V of the periodic table. These kind of glasses are useful for their structural and optical properties; the most familiar example is window glass.

- Chalcogenide glasses formed by the combination of chalcogens (sulphur, selenium and tellurium) and elements such as arsenic and germanium. The applications of chalcogenide glasses are wide: they can be used to fabricate diffraction gratings, planar channel waveguides, optical fibres amplifiers and lasers and optical switches [4].

- Organic molecules. Many organic molecules including solvents such as toluene and methanol and low molecular weight compounds such as glycerol and sucrose, as well as solutions of such molecules in water or organic solvents, form glasses.

- Polymer glasses. Almost all polymers form glasses. Examples are poly(methyl methacrylate) and polycarbonates which are extensively used for their transparency and good mechanical properties in different fields such as electronic components, construction materials or medical applications.

- Metallic glasses are formed when some metal alloys are cooled very quickly. The resulting metallic glasses have unique magnetic and mechanical properties that find applications in recording heads and transformer cores.

1.2 Relaxation time and viscosity: phase changes in glass-forming liquids

At relatively high temperatures, the relaxation times in liquids (and consequently their viscosity η) depends on temperature according to the Arrhenius law [5, 6]:

$$\eta = \frac{G_0}{\nu} exp\left(\frac{E}{k_B T}\right) \tag{1.1}$$

where G_0 is an instantaneous modulus that characterizes the elastic response of the materials at times much shorter than the relaxation time, ν is the characteristic vibration frequency of the constituent atoms, E is the activation energy and k_B is the Boltzmann's constant. At lower temperatures, assuming that the liquid has not first crystallized, the relaxation time associated with changes in configuration of the atoms or molecules, τ_{config}, assumes a temperature dependence that strongly departs from the temperature dependence of the characteristic time of vibrations, τ_{vib} (Figure 1.1).

As the temperature is lowered, the system reaches a state in which the (configurational) relaxation time is comparable to the timescale of human experimentation τ_{exp}. This occurrence, which takes place at a temperature T_g, marks the onset of the experimental glass transition. T_g is defined phenomenologically as the temperature at which the time scale for molecular rearrangements becomes long compared to the time

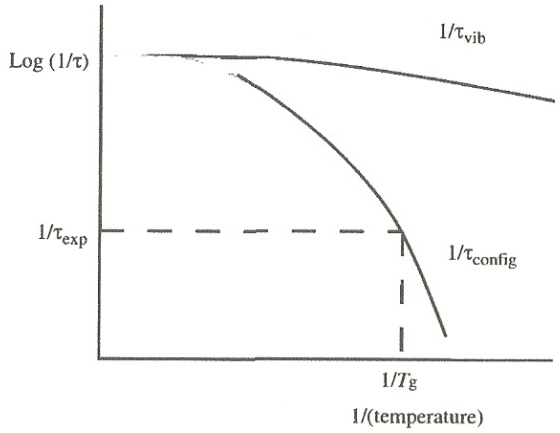

Figure 1.1: Temperature dependence of the relaxation times in a glass-forming liquid.

scale of dynamic observations, i.e., around 100 seconds or, equivalently, when the viscosity becomes higher than 10^{13} Poise. When a liquid goes through such a transition, a glass is formed. A glass is a material which is identical, in its state of order, to a liquid, which means that it has short-range order but not long-range order; contrary to the liquid state, however, a glass behaves mechanically like a solid.

The transition between a liquid state to a glass is marked by discontinuities in thermodynamics quantities such as the heat capacity or the thermal expansivity, at a well defined temperature (the glass transition temperature T_g). Figure 1.2 displays the change of volume of a glass-forming liquid as a function of temperature.

If the liquid can form a crystal, it will follow the path marked "Crystal": at some well defined temperature T_m, the volume will change discontinuously as the liquid forms a crystalline phase having a different degree of freedom with respect to the liquid one (first-order phase transition). It is

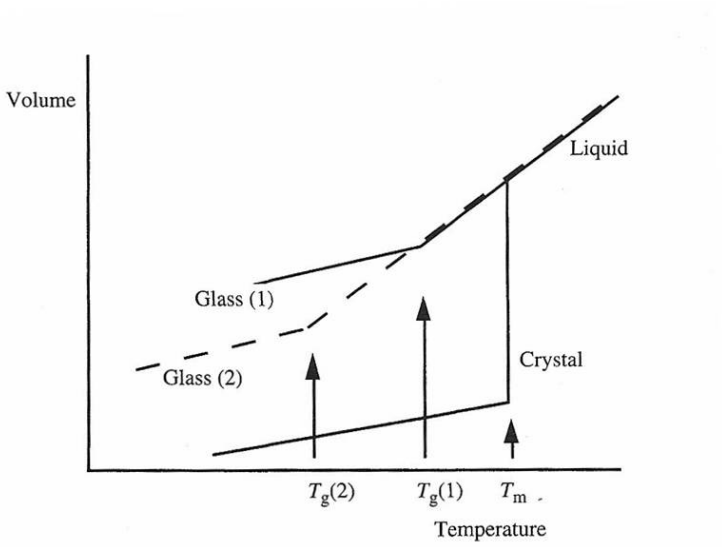

Figure 1.2: Volume changes on cooling a glass-forming liquids

however possible to cool down a liquid below its freezing point without crystallization. This can happen because the cooling rate is so fast that the liquid does not have the time to crystallize, or it may be because the molecules have some permanent disorder that prevents the formation of a crystal.

If the liquid does not crystallize it will follow the "Glass (1)" path. The change of slope at the glass transition temperature in Figure 1.2 is similar to a second-order phase transition, but it is not a true thermodynamic phase transition because the value of T_g depends on the rate at which the experiment is done (generally, T_g decreases with decreasing cooling rate, so that upon cooling it more slowly the system might follow the "Glass (2)" line in Figure 1.2), on the technique used to measure it and on its thermal history. The thermodynamic and dynamic properties of a glass therefore depend upon how it is formed. Further cooling below T_g forces the system

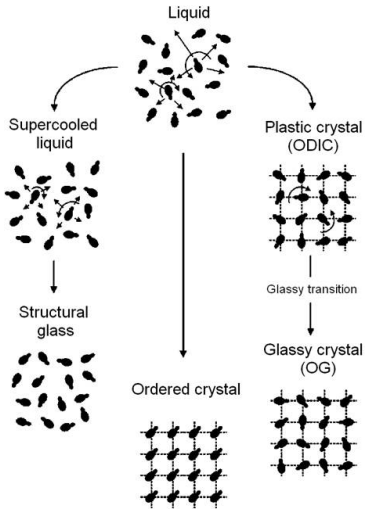

Figure 1.3: Schematic representation of the possible transitions from the liquid state of dipolar molecules into a structural glass (SG), an ordered crystal or an orientational glassy phase (OG) [9].

to freeze into a disordered state, leading to a so-called structural glass (SG) which maintains the molecular disorder (orientational and translational) of the liquid phase from which it derives.

Another type of glassy behaviour arises when there is only orientational disorder, rather than a full structural disorder (see Figure 1.3). This gives rise to a characteristic state, called "plastic phase" [7], intermediate between the crystalline (translationally and orientationally ordered) state and the liquid phase. The molecular compounds which display a plastic state are called Orientationally Disordered Crystals (ODIC) or plastic crystals. In this phase, the centres of mass of the molecules form a regular crystalline lattice but the molecular orientations are dynamically disordered. This orientational disorder can freeze yielding a glassy crystal or orientational glass (OG) [8].

1.2.1 Temperature dependence of the relaxation time

For some glass-forming liquids the temperature dependence of the relaxation time follows an Arrhenius law [10]:

$$\tau(T) = \tau_\infty exp\left(\frac{E_a}{RT}\right) \tag{1.2}$$

where E_a, in the case of Arrhenius behaviour, is a constant called activation energy (in general it depends on temperature). The liquids that display this behaviour are classified as strong liquids. However, for most glass-forming liquids the temperature dependence of $\tau(T)$ is more complex and follows the Vogel-Fulcher-Tammann (VFT) phenomenological law [11–18]:

$$\tau(T) = \tau_\infty exp\left(\frac{DT_0}{T - T_0}\right) \tag{1.3}$$

where T_0 is the so-called Vogel temperature associated with the estimated ideal glass transition, τ_∞ is a characteristic time of the order of the atomic oscillation time ($\approx 10^{-14}s$) and D is the so-called strength coefficient, which measures the fragility of the compound. Figure 1.4 represents the logarithmic relaxation time variation as a function of a reduced inverse temperature scale T_g/T. This so-called Angell plot [19] is used to classify supercooled liquids into strong and fragile.

The slope of $log\tau$ vs. T_g/T (Angell plot) calculated at $T = T_g$ is called "fragility" m of a glass [20]:

$$m = \left(\frac{dlog\tau(T)}{dT_g/T}\right)_{T=T_g} \tag{1.4}$$

The fragility index m is considered an essential parameter of the kinetic and relaxational behaviour of supercooled liquids and it is used to classify the slowing down of the dynamics of the glass-forming liquids,

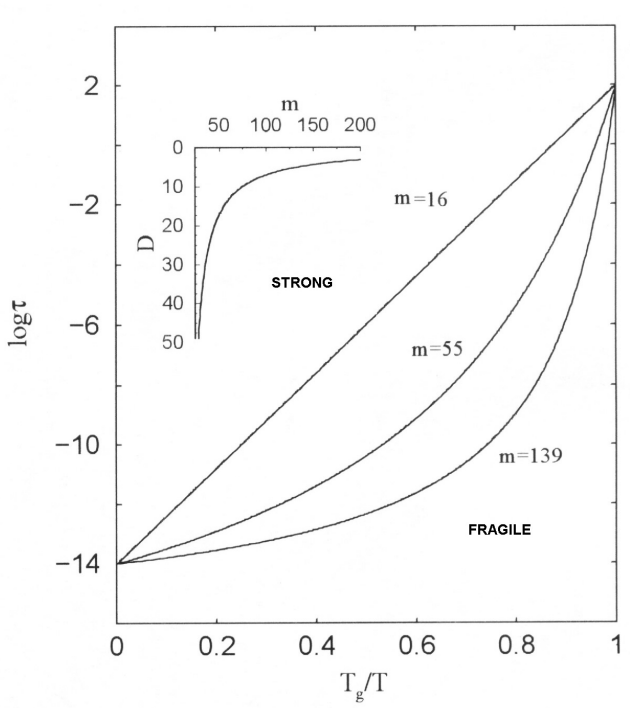

Figure 1.4: Temperature dependence (normalized to T_g) of the logarithmic relaxation time. This graphical representation, called Angell plot, is used to classify supercooled liquid as strong or fragile according to their deviation from the Arrhenius-like behaviour. The inset exhibits the strength coefficient D as a function of the fragility parameter m.

by measuring the degree of deviation from the Arrhenius behaviour. A fragility m equal to 16 is the upper limit for strong liquids, whereas larger values of m indicate that the liquid is fragile. Only a few glass formers have fragility below 25; most are therefore fragile.

A useful method to check the validity of the VFT relation in different temperature ranges is the derivative-based analysis by Stickel and coworkers [21, 22]. In most supercooled liquids the plot of the derivative $[dlog(\tau)/d(1/T)]^{-1/2}$ versus $1/T$ exhibits a linear behaviour consistent with VFT dependence only in a restricted temperature range and it is

characterized by a critical temperature T_B at which the dynamics changes from a VFT behaviour (for $T < T_B$) to a different VFT or a non-VFT behaviour ($T > T_B$). This can be modelled by considering the relation between activation energy $E_a(T)$, activation enthalpy $H_a(T)$ and entropy S ($E_a(T) = H_a(T) - TS(T)$) [23]:

$$\frac{dln\tau(T)}{d(1/T)} = \frac{d[E_a(T)/RT]}{d(1/T)} = \frac{H_a(T)}{R} \tag{1.5}$$

By combining this equation with the derivative of the VFT relation (1.3), we can obtain:

$$\left(\frac{dln\tau(T)}{d(1/T)}\right)^{-\frac{1}{2}} = \left(\frac{H_a(T)}{R}\right)^{-\frac{1}{2}} = ((D_T T_0)^{-\frac{1}{2}}) - \frac{[T_0(D_T T_0)^{-\frac{1}{2}}]}{T} = A - \frac{B}{T} \tag{1.6}$$

with $T_0 = B/A$ and $D_T = 1/AB$. R is the gas constant and $H_a(T)$ is the apparent, temperature-dependent, activation enthalpy related to the activation energy and to the entropy S as $E_a(T) = H_a(T) - TS(T)$. Since the temperature dependence of the relaxation dynamics is one of the most prominent features of glass forming liquids, many other models have been proposed with the aim of portraying experimental data in the cases in which the VFT is applicable only in a limited range of temperature. Cohen and Grest (CG) [24, 25] developed a model resulting in a single equation which is usually valid in a temperature region wider than that described by the VFT model. The relaxation time in the CG model is given by:

$$\tau(T) = \tau_0^{CG} exp\left[\frac{B}{T - T_{CG} + [(T - T_{CG})^2 + CT]^{1/2}}\right] \tag{1.7}$$

The four parameters τ_0^{CG}, B, C and T_{CG} are material constants. In the CG model it is assumed that for every temperature the mobility of

the molecules is a function of the free available volume, which is closely related to the viscosity.

Among the variety of theoretical models that describe the glassy dynamics, the mode coupling theory (MCT) introduced in 1992 by Götze and Sjögren [14, 26], yields the most extensive set of predictions at high temperatures which can be matched with experiments. In this model the correlation between the positions of the molecules, *i.e.* the probability to find a molecule in a certain position at a time t, is described by the autocorrelation function $\phi(t)$ of the density fluctuations. From this function it is possible to extrapolate the relaxation function to describe the dynamics of the system. This theoretical model describes the relaxation time evolution in terms of a phase transition at a critical temperature T_x (with $T_x >> T_g$):

$$\tau(T) = \tau_0^{MCT} \left(\frac{T - T_x}{T_x} \right)^{-\gamma} \tag{1.8}$$

where γ is a power exponent. From this equation one obtains [23]:

$$\frac{H_a(T)}{R} = \left(\frac{dln\tau}{d(1/T)} \right) = \frac{\gamma T^2}{T - T_x} \tag{1.9}$$

Hence the plot $RT^2/H_a(T) = A+BT$ should have a linear temperature-dependence in the region of validity of the MCT relation. A simple linear regression yields in such case the parameters $T_x = |A/B|$ and $\gamma = |B - 1|$. In Figure 1.5 is represented a comparison between the scaling behaviours described by the Arrhenius equation, the VFT equation and the MCT theory.

Another useful model in the study of glass transitions is the Dynamic Scaling Model (DSM) based on the idea of cooperative motion introduced by Adam and Gibbs [28]. Near the glass transition temperature, the

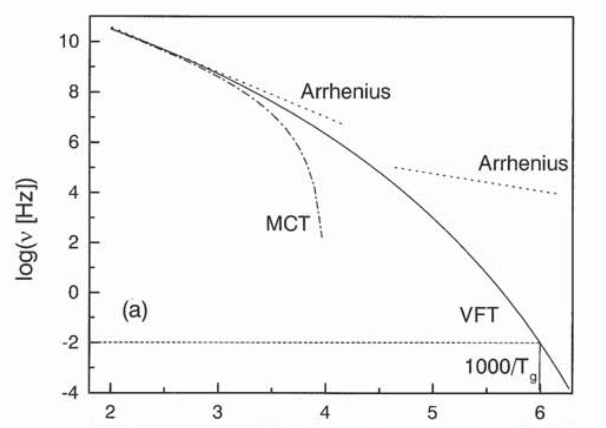

Figure 1.5: Comparison between the scaling behaviours described by the Arrhenius equation, the VFT equation and the MCT theory [27].

glass-forming liquids are dynamically heterogeneous, which means that only some small fraction of the material at a given position is able to move at each moment in time. Hence some regions of the sample have to wait for their immediate neighbours to move before they can move. Using this simple idea it is possible to write an equation linking the relaxation time to the size ξ of these cooperatively rearranging regions; this equation diverges at a critical temperature T_C ($T_C < T_g$) [29, 30]:

$$\xi^z \approx \tau(T) = \tau_0 \left(\frac{T - T_C}{T_C} \right)^{-\nu z} \tag{1.10}$$

Here, z is the dynamic exponent which describes the divergence of the correlation length ξ. For a glass-forming liquid, usually $\nu = 3/2$ and $\nu z = 9$ (hence $z = 6$). It is worth pointing out that Eq.1.10 is formally identical to Eq.1.8, hence T_C and νz can be calculated from equation (1.9) with $\gamma = \nu z$ and $T_C = T_x$. At the same time, it must be remembered that in the DSM $T_C < T_g$, while in the MCT $T_x >> T_g$, so that although formally equivalent the two models have different physical assumptions and parameters.

1.2.2 Pressure dependence of the relaxation time

As we already mentioned, the glass state can be obtained by lowering the temperature of a glass-forming system to below the glass temperature T_g. Another way to observe the glass transition is by compressing the system at constant temperature. The glass state is obtained in such case above a glass transition pressure P_g. While an isobaric change of temperature influences both the volume and the thermal energy of a sample, an isothermal change of pressure only affects its volume. As a consequence, by means of high-pressure measurements it is possible to separate the effects of temperature and volume on the dynamics of the system. As already mentioned in section 1.2.1, near the glass transition the temperature dependence of the structural relaxation time can be described by the phenomenological VFT equation (Eq. 1.3). An analogous equation for the pressure dependence of the relaxation time can be obtained observing that, from a dynamic point of view, decreasing the temperature and increasing the pressure both results in a slowing down of the molecular rearrangements dynamics. Thus, dynamically, T and P can be considered as "equivalent" thermodynamic variables ($P \leftrightarrow T^{-1}$).

A phenomenological VFT law can be given for the variation of the relaxation time as a function of pressure, as follows [31, 32]:

$$\tau(T,P) = \tau_0(T,0) exp\left(\frac{CP}{P_0 - P}\right) \tag{1.11}$$

Here τ_0 is the relaxation time at ambient pressure, which can be estimated directly from the experimental measurements, and C and P_0 are empirical parameters that are functions of T only. Experimentally, the C parameter is found to be constant over a wide range of P and T [33–38]. In some cases the pressure dependence of the relaxation time of

the α-process follows a simply-activated exponential law. In such a case the structural relaxation time as a function of P can be described by a volume-activated law:

$$\tau(P) = \tau_0 exp\left(\frac{P\Delta V^{\#}}{RT}\right) \tag{1.12}$$

where R is the gas constant, $\tau_0(T, 0)$ is the value of τ_α at atmospheric pressure and $\Delta V^{\#}$ is the molar activation volume. The activation volume can be used to characterize the relaxation process in the glass-forming liquids since it can be considered as the minimum volume around the molecule necessary to promote the local molecular motions, just as the activation energy represents the typical energy barrier to overcome. Usually, the activation volume decreases with increasing temperature [39].

If the relaxation time is not simply (volume-)activated, one may define an apparent molar activation volume as:

$$\Delta V^{\#} = RT\frac{\partial ln\tau}{\partial P} \tag{1.13}$$

Such a quantity is a function of pressure, besides of temperature. Both equations 1.11 and 1.12 have been introduced phenomenologically, and they are not able to explain satisfactory the pressure dependence of the structural relaxation time in all the cases.

A combined description can sometimes be given of the pressure and temperature dependence of the dynamics of glass formers. Such approach, called "thermodynamic scaling", originates from the observation that, near the glass transition, the relaxation time can be plotted independently of the thermodynamics conditions onto a single master curve described by the scaling equation:

$$log\tau = f(T^{-1}V^{-\gamma}) \tag{1.14}$$

where the function f might be a VFT like equation and γ is a material constant. The scaling of $log(\tau)$ with the quantity $T^{-1}V^{-\gamma}$ can be rationalized by considering a generalized Lennard-Jones (LJ) potential [40] for the intermolecular interactions, with a repulsive part proportional to $r^{-3\gamma}$ and an attractive term proportional to $r^{-3\gamma/2}$.

The thermodynamic scaling was first observed to hold for orthoterphenyl (OTP) with $\gamma = 4$ [41, 42], and then it has be shown to be generally valid for various materials with $0.13 \leq \gamma \leq 8.5$ [43–46]. Equation 1.14 can describe the relaxation time obtained by dielectric spectroscopy [43–46], light scattering [42, 47], and viscosity [48] measurements, with comparable values of γ for a given material. The scaling behaviour has been also confirmed by simulations [49].

The value of the parameter γ gives an idea of the relative importance of V and T on the dynamics. In particular, a value of γ equal to 0 corresponds to a thermally activated behaviour, while $\gamma \to \infty$ corresponds to the (volume-activated) hard sphere limit [40]. If an activated process is volume-dominated, the dependence of the relaxation time on T and V can be written as $\tau(T,V) = \tau_0 exp(C/TV^{\gamma})$. The value of γ depends on the ratio between the activation enthalpy at constant volume ($E_V = R[\partial log\tau/\partial T^{-1}]_V$) and the activation enthalpy at constant pressure ($E_P = R[\partial log\tau/\partial T^{-1}]_P$) in the following manner:

$$\frac{E_V}{E_P}\Big|_{T_g} = \frac{1}{1+\gamma\alpha_P T_g}, \tag{1.15}$$

where α_P is the value that the constant-pressure expansion coefficient has at T_g. In the case of a temperature-dominated dynamics this ratio

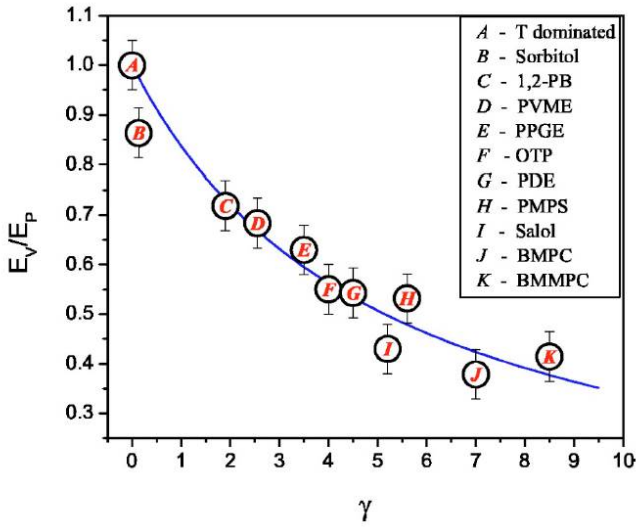

Figure 1.6: Ratio of the activation enthalpy at constant volume, E_V, and at constant pressure, E_P, as a function of the γ parameter for different glass formers (B: D-sorbytol; C: 1,2-polybutadiene; D: poly(vinyl methyl ether); E: poly(phenyl glycidy ether)-coformaldehyde; F: ortho-terphenyl; G: phenolphthalein-dimethylether; H: polymethylphenylsiloxane; I: phenyl salicylate; J: 1,1'-bis(p-methoxyphenyl)cyclohexane; K: 1,1'- di(4-methoxy-5-methylphenyl)cyclohexane) [43].

tends to 1, while it tends to 0 in the case of volume-dominated processes [50]. Figure 1.6 reports the value of the E_V/E_P ratio for different glass formers as a function of the γ parameter [43]. It can be observed that the parameter γ is, as expected, larger for glass formers in which the volume is the more dominant variable. In this case applying the thermodynamic scaling against the variable TV^γ removes the volume contribution to the Arrhenius behaviour near T_g.

If the behaviour of the relaxation time at constant pressure is known, it is possible to determine the behaviour at constant volume by using the

equation of state V(T,P) and the value of γ for the glass-former under study [51]. A general equation of state is given by the Tait equation [52]:

$$V(T,P) = V_0[1+\alpha_V(T-T_0)]\left[1 - Cln\left(1+\frac{P}{b_1 exp(-b_3 T)}\right)\right] \quad (1.16)$$

where the parameters V_0, T_0, α_V, C, b_1 and b_3 can be found by using this equation to fit the measurements of the volume as a function of pressure at fixed temperature values (obtained *e. g.* by using a PVT apparatus, see section 3.1.2).

If we define the isochoric fragility as $m_V = \partial \log\tau/\partial(T_g/T)|_{T=T_g,V=cte}$, it follows from eq. 1.14 that the isobaric fragility, defined as $m_P = \partial \log\tau/\partial(T_g/T)|_{P=P_g}$, can be calculated as [43, 44]:

$$m_P = m_V(1+\gamma\alpha_P T_g) \quad (1.17)$$

where $\alpha_P = 1/V(\partial V/\partial T)_P$ is the isobaric (volume) expansion coefficient at T_g. By comparing the value of m_V and m_P (measured at atmospheric pressure) for more than 38 glass-formers, it has been found that the two fragilities are indeed linearly correlated: $m_P = (37 \pm 3) + (0.83 \pm 0.05)m_V$. Moreover, the isochoric fragility is related to the scaling parameter according to $\gamma = -1.042 + 217/m_V$ [53]. The consequence of this is that the dependence of the relaxation time on volume on one hand, and on temperature on the other, are actually correlated, so that the scaling parameter γ can be used (and is sufficient) to classify the glass-formers.

Another way to calculate the fragility is by knowing the isothermal dependence of the relaxation time on pressure. From the apparent activation volume and the pressure coefficient of the glass transition temperature, the fragility can be calculated as [54]:

$$m_P = \frac{\Delta V^{\#}}{2.303R(dT_g/dP)} \tag{1.18}$$

For the majority of glass-formers, the variation of T_g with pressure is roughly linear at low pressures and sublinear at higher pressures and, in general, it can be described by using the Andersson and Andersson empirical equation [55]:

$$T_g = k_1 \left(1 + \frac{k_2}{k_3} P\right)^{1/k_2} \tag{1.19}$$

where k_1, k_2 and k_3 are material constants. It should be noted that this equation is not valid for negative pressures, and it can be used only if T_g increases upon increasing the applied pressure [56]. According to ref. [14, 57, 58], under extreme pressures $T_g(P)$ can display, rather than a monotonic increase, an asymptotic behaviour or a maximum.

Bibliography

[1] P. W. Anderson *Science*, vol. 267, p. 1615, 1995.

[2] P. Lunkenheimer, U. Schneider, R. Brand, and A. Loidl *Contemporany Physics*, vol. 41, p. 15, 2000.

[3] M. D. Ediger, C. A. Angell, and S. R. Nagel *J. Phys. Chem.*, vol. 100, p. 13200, 1996.

[4] A. Zakery and S. R. Elliott *J. Non-Cryst. Solids*, vol. 330, p. 1, 2003.

[5] R. A. L. Jones, *Soft Condensed Matter*. New York: Oxford University press, 2002.

[6] S. G. Brush *Chem. Rev.*, vol. 62, p. 513, 1962.

[7] J. Timmermans *J. Phys. Chem. Biol.*, vol. 35, p. 331, 1938.

[8] K. Binder and A. Young *Phys. Rev. B*, vol. 29, p. 2864, 1984.

[9] R. Brand, P. Lunkenheimer, and A. Loidl *J. Chem. Phys.*, vol. 116, p. 10386, 2002.

[10] S. Arrhenius *Z. Phys. Chem.*, vol. 4, p. 226, 1889.

[11] H. Vogel *Phys. Z.*, vol. 22, p. 645, 1921.

[12] G. S. Fulcher *J. Am. Ceram. Soc.*, vol. 8, p. 339, 1925.

[13] G. Tammann and W. Hesse *Z. Anorg. Allg. Chem.*, vol. 156, p. 245, 1926.

[14] E. J. Donth, *The Glass Transition: Relaxation Dynamics in Liquids and Disordered Materials*. Berlin: Springer, 2001.

[15] J. C. Dyre *Rev. Mod. Phys.*, vol. 78, p. 953, 2006.

[16] C. A. Angell *Proc. Natl. Acad. Sci.*, vol. 92, p. 6675, 1995.

[17] G. Floudas *Prog. Polym. Sci.*, vol. 29, p. 1143, 2004.

[18] C. M. Roland, S. Hensel-Bielowka, M. Paluch, and R. Casalini *Prog. Prog. Phys.*, vol. 68, p. 1405, 2005.

[19] C. A. Angell and H. Kanno *Science*, vol. 193, p. 1121, 1976.

[20] R. Böhmer, K. L. Ngai, C. A. Angell, and D. J. Plazek *J. Chem. Phys.*, vol. 99, p. 4201, 1993.

[21] F. Stickel, E. W. Fischer, and R. Richert *J. Chem. Phys.*, vol. 104, p. 2043, 1996.

[22] C. Hansen, F. Stickel, T. Berger, R. Richert, and E. W. Fischer *J. Chem. Phys.*, vol. 107, p. 1086, 1997.

[23] A. Drozd-Rzoska and S. J. Rzoska *Phys. Rev. E*, vol. 73, p. 041502, 2006.

[24] G. S. Grest and M. H. Cohen *Phys. Rev. B*, vol. 21, p. 4113, 1980.

[25] M. H. Cohen and G. S. Grest *J. Non-Cryst. Solids*, vol. 61-62, p. 749, 1984.

[26] W. Göetze and L. Sjöegren *Rep. Prog. Phys.*, vol. 55, p. 241, 1992.

[27] F. Kremer and A. Schönhals, *Broadband Dielectric Spectroscopy.* Berlin: Springer, 2002.

[28] G. Adam and J. H. Gibbs *J. Chem. Phys.*, vol. 43, p. 139, 1965.

[29] R. Colby *Phys. Rev. E*, vol. 61, p. 1783, 2000.

[30] B. M. Erwin and R. H. Colby *J. Non-Cryst. Solids*, vol. 307-310, p. 225, 2002.

[31] M. Paluch, S. Rzoska, P. Habdas, and J. Ziolo *J. Phys.: Condens. Matter*, vol. 8, p. 10885, 1996.

[32] S. Corezzi, P. Rolla, M. Paluch, J. Ziolo, and D. Fioretto *Phys. Rev. E*, vol. 60, p. 4444, 1999.

[33] M. Paluch, S. J. Rzoska, P. Habdas, and J. Ziolo *J. Phys.: Condens. Matter*, vol. 10, p. 4131, 1998.

[34] M. Paluch *J. Chem. Phys.*, vol. 115, p. 10029, 2001.

[35] M. Paluch, C. M. Roland, and S. Pawlus *J. Che. Phys.*, vol. 116, p. 10932, 2002.

[36] M. Paluch, S. Pawlus, and C. M. Roland *Macromolecules*, vol. 35, p. 7338, 2002.

[37] M. Paluch, R. Casalini, S. Hensel-Bielowka, and C. M. Roland *J. Chem. Phys.*, vol. 116, p. 9839, 2002.

[38] C. M. Roland and R. Casalini *Macromolecules*, vol. 36, p. 1361, 2003.

[39] A. Grzybowski, K. Koperwas, A. Swiety-Pospiech, K. Grzybowska, and M. Paluch *Phys. Rev. B*, vol. 87, p. 054105, 2013.

[40] W. G. Hoover and M. Ross *Contemp. Phys.*, vol. 12, p. 339, 1971.

[41] A. Tölle *Rep. Prog. Phys.*, vol. 64, p. 1473, 2001.

[42] C. Dreyfus, A. Aouadi, J. Gapinski, M. Matos-Lopes, W. Steffen, A. Patkowski, and R. M. Pick *Phys. Rev. E*, vol. 68, p. 011204, 2003.

[43] R. Casalini and C. M. Roland *Phys. Rev. E*, vol. 69, p. 062501, 2004.

[44] C. M. Roland and R. Casalini *Colloid Polym. Sci*, vol. 283, p. 107, 2004.

[45] C. M. Roland, R. Casalini, and M. Paluch *J. Polym. Sci., Polym. Phys. Ed.*, vol. 42, p. 4313, 2004.

[46] C. M. Roland and R. Casalini *J. Non-Cryst. Solids*, vol. 351, p. 2581, 2005.

[47] C. Dreyfus, A. Le Grand, J. Gapinski, W. Steffen, and A. Patkowski *Eur. Phys. J. B*, vol. 42, p. 309, 2004.

[48] C. Alba-Simionesco, A. Calliaux, A. Alegria, and G. Tarjus *Europhys. Lett.*, vol. 68, p. 58, 2004.

[49] J. Budzien, J. D. McCoy, and D. B. Adolf *J. Chem. Phys.*, vol. 121, p. 10291, 2004.

[50] M. Naoki, H. Endou, and K. Matsumoto *J. Phys. Chem.*, vol. 91, p. 4169, 1987.

[51] R. Casalini and C. M. Roland *Phys. Rev. B*, vol. 71, p. 014210, 2005.

[52] R. K. Jain and R. Simha *Macromolecules*, vol. 22, p. 464, 1989.

[53] R. Casalini, S. Capaccioli, and C. M. Roland *J. Phys. Chem. B*, vol. 110, p. 11491, 2006.

[54] M. Paluch, J. Gapinski, A. Patkowski, and E. W. Fischer *J. Chem. Phys.*, vol. 114, p. 8048, 2001.

[55] S. P. Andersson and O. Andersson *Macromolecules*, vol. 31, p. 2999, 1998.

[56] A. Drozd-Rzoska, S. J. Rzoska, C. M. Roland, and A. R. Imre *J. Phys.: Condens. Matter*, vol. 20, p. 244103, 2008.

[57] A. Drozd-Rzoska, S. J. Rzoska, and A. R. Imre *J. Non-Crust. Solids*, vol. 353, p. 3915, 2007.

[58] A. Drozd-Rzoska, S. J. Rzoska, M. Paluch, A. R. Imre, and C. M. Roland *J. Chem. Phys.*, vol. 126, p. 164504, 2007.

Chapter 2

DIELECTRICS UNDER AN APPLIED ELECTRIC FIELD

2.1 Static response

When a constant electric field is applied to a dielectric (for example inside a capacitor at fixed potential difference), the atomic and/or molecular charges in the dielectric are displaced or reoriented from their equilibrium position or orientation causing the polarization of the material and the formation of a macroscopic dipolar moment. The polarization $\mathbf{P}$ is defined as the average dipole moment per unit volume and quantifies how the material reacts to an applied electric field. Usually, a linear relation can be written between $\mathbf{P}$ and the macroscopic field $\mathbf{E}$ inside the dielectric as:

$$\mathbf{P} = \chi \varepsilon_0 \mathbf{E} \tag{2.1}$$

Defining a displacement field $\mathbf{D}$ as $\mathbf{D} = \mathbf{P} + \varepsilon_0 \mathbf{E}$, this linear relationship

can be also written as:

$$\mathbf{D} = \varepsilon_r \varepsilon_0 \mathbf{E} \tag{2.2}$$

In the previous equations, ε_0 is the permittivity of vacuum, χ the susceptibility of the material and $\varepsilon_r = 1 + \chi$ is its relative dielectric constant. Both ε_r and χ are real dimensionless numbers. Assuming that the dielectric contains no free charges, the polarization $\mathbf{P}$ is the sum of a contribution due to the induced dipoles $\mathbf{P}_{id}$ plus a contribution due to the permanent dipoles $\mathbf{P}_{pd}$. In detail, the first contribution is caused by the electronic polarization ($\mathbf{P}_e$) due to the displacement of the electrons with respect to the nuclei and by the atomic (or ionic) polarization ($\mathbf{P}_a$) due to the displacement of the atoms (ions) with respect to one another. If the material in the capacitor is made of polar molecules, there is an additional contribution to polarization due to the preferential orientation of permanent dipoles with the electric field, the so-called orientational polarization ($\mathbf{P}_o$). The total polarization can then be written as:

$$\mathbf{P} = \mathbf{P}_{id} + \mathbf{P}_{pd} = \mathbf{P}_e + \mathbf{P}_a + \mathbf{P}_o \tag{2.3}$$

Besides the contribution of permanent dipole moments, and especially if there are none, it is necessary to take in account the induced molecular dipole moment, which can be expressed as $\mathbf{p}_{induced} = \alpha \mathbf{E}_{loc}$, where $\mathbf{E}_{loc} = \mathbf{E} + \mathbf{P}/3\varepsilon_0$ is the local electric field at the molecular position and α_{id} is the polarizability of each molecule. The relation between the macroscopic electric field and the polarization due to N induced dipoles per unit volume V was deduced by Mosotti [1] and Clausius [2] as:

$$\mathbf{P}_{id} = \frac{N}{V}\mathbf{p}_{induced} = \frac{N}{V}\alpha_{id}\boldsymbol{E}_{loc} = \frac{\frac{N}{V}\alpha_{id}}{1 - \frac{N\alpha_{id}}{3V\varepsilon_0}}\boldsymbol{E} \tag{2.4}$$

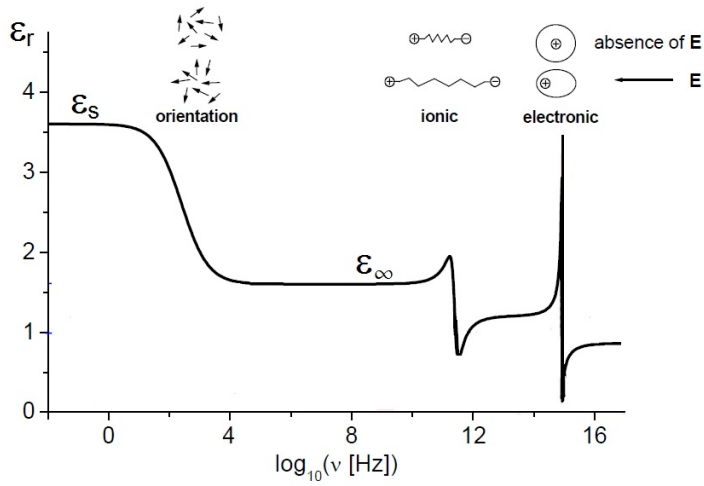

Figure 2.1: Types of polarization and relative dielectric permittivity ε_r as a function of frequency.

Using the linear constitutive equation $P = \varepsilon_0(\varepsilon_r - 1)E$, this yields the Clausius-Mosotti formula:

$$\frac{\varepsilon_r - 1}{\varepsilon_r + 2} = \frac{N\alpha_{id}}{3V\varepsilon_0} \tag{2.5}$$

The relations 2.4 and 2.5 are valid only below the characteristic frequency of ionic and electronic motions (around 10^{12} and 10^{15} Hz respectively) and in this case the relative permittivity ε_r is replaced with the constant value ε_∞ (see Figure 2.1) and the Clausius-Mosotti equation can be rewritten as:

$$\frac{\varepsilon_\infty - 1}{\varepsilon_\infty + 2} = \frac{N}{V}\frac{\alpha_{id}}{3\varepsilon_0} \tag{2.6}$$

The orientational polarization can be expressed as the macroscopic volume density of the vectorial sum over all N permanent dipoles contained in the unit volume V as:

$$\mathbf{P}_o = \frac{\sum \boldsymbol{\mu}_i}{V} = \frac{N}{V} < \boldsymbol{\mu} > \tag{2.7}$$

Here $< \boldsymbol{\mu} >$ is the mean dipole moment and it depends on the interaction between dipoles and the strength of the electric field at the location of each dipole.

Let us assume that the dipoles do not interact which each other and thus that the local electric field at the position of the dipole is equal to the external electric field (as in a gas). In this case the mean value of the dipole moment is given by the balance between the thermal energy and the interaction energy $W = -\boldsymbol{\mu} \cdot \boldsymbol{E}$ of a dipole with the electric field. Using the Boltzmann statistics [3] one gets:

$$< \boldsymbol{\mu} >= \frac{\int_{4\pi} \boldsymbol{\mu}\ exp\left(\frac{\boldsymbol{\mu}\cdot\boldsymbol{E}}{k_B T}\right) d\Omega}{\int_{4\pi} exp\left(\frac{\boldsymbol{\mu}\cdot\boldsymbol{E}}{k_B T}\right) d\Omega} \tag{2.8}$$

where T is the absolute temperature, k_B is the Boltzmann constant and $d\Omega$ is the elementary solid angle. Only the component parallel to the electric field contributes to the polarization. In fact $W = -\mu E cos\theta = -\mu_{\parallel} E$, where θ is the angle between the orientation of the dipole moment and the electric field. Therefore it is:

$$< \mu >= \frac{\int_0^{\pi} \mu\ cos\theta\ exp\left(\frac{\mu E cos\theta}{k_B T}\right) \frac{sin\theta}{2} d\theta}{\int_0^{\pi} cos\theta\ exp\left(\frac{\mu E cos\theta}{k_B T}\right) \frac{sin\theta}{2} d\theta} \tag{2.9}$$

With a variable change and considering W to be small compared to the thermal energy, equation 2.9 reduces to:

$$< \boldsymbol{\mu} >= \frac{\mu^2}{3 k_B T} \boldsymbol{E} = \alpha_o \boldsymbol{E} \tag{2.10}$$

being α_o the orientational polarizability.

Finally the polarization due to the permanent dipoles can be written as:

$$\mathbf{P}_{dp} = \mathbf{P}_o = \frac{N}{V}\alpha_o \boldsymbol{E}_{loc} = \frac{\mu^2}{3k_BT}\frac{N}{V}\boldsymbol{E}_{loc} \tag{2.11}$$

The total polarization due to both the permanent and the induced molecular dipoles is the sum of equations 2.4 and 2.11:

$$\mathbf{P} = \frac{N}{V}(\alpha_{id} + \alpha_o)\boldsymbol{E}_{loc} \tag{2.12}$$

Using again the expression for the local field ($\mathbf{E}_{loc} = \mathbf{E} + \mathbf{P}/3\varepsilon_0$) and the linear constitutive relation, this time starting from eq. 2.12, we arrive at the following expression:

$$\frac{\varepsilon_s - 1}{\varepsilon_s + 2} = \frac{N}{V3\varepsilon_0}(\alpha_{id} + \alpha_o) \tag{2.13}$$

where ε_s is the static permittivity taking into account the polarization due to both permanent and induced dipoles (see Figure 2.1). Using eq. 2.6 this gives:

$$\frac{\varepsilon_s - 1}{\varepsilon_s + 2} - \frac{\varepsilon_\infty - 1}{\varepsilon_\infty + 2} = \frac{N}{V}\frac{\mu^2}{9\varepsilon_0 k_B T} \tag{2.14}$$

The last equation is known as Debye formula which takes into account self-consistently the electric dipole interaction between induced dipoles but treats permanent dipoles as non-interacting.

Onsager [4] extended the Debye formula to include the enhancement of the permanent dipole of a molecule due to the polarization of the environment. His result can be written in terms of the dielectric strength $\Delta\varepsilon$ as:

$$\Delta\varepsilon = \varepsilon_s - \varepsilon_\infty = \frac{1}{3\varepsilon_0}F\frac{\mu^2 N}{k_B T V} \tag{2.15}$$

where the factor F is given by:

$$F = \frac{\varepsilon_s(\varepsilon_\infty + 2)^2}{3(2\varepsilon_s + \varepsilon_\infty)} \tag{2.16}$$

To take into account the local interactions between dipoles, a further correction is necessary. Kirkwood [5–7] and Fröhlich [8] introduced a correlation factor g_K to model the interaction between dipoles:

$$g_K = \frac{< \sum_i \boldsymbol{\mu}_i \sum_j \boldsymbol{\mu}_j >}{N\mu^2} = \frac{\mu^2}{\mu_{gas}^2} \tag{2.17}$$

where μ_{gas}^2 is the mean-square dipole moment for non-interacting dipoles, which can be measured in the gas phase or in diluted solutions. If we consider only the first neighbours of a given dipole, the g_K factor can be approximated as:

$$g_K = 1 + z\langle cos\psi \rangle \tag{2.18}$$

where z is the coordination number and ψ is the angle between the selected dipole and one of the neighbours. If there is a correlation between the orientations of the neighbouring dipoles, then the correlation factor will differ from 1 ($\langle cos\psi \rangle \neq 1$). Values of g_K grater than 1 are indicative of a tendency towards parallel alignment of dipoles, values lower than 1 correspond to an anti-parallel alignment and a value of 1 marks the absence of orientational ordering. In practice g_K is very difficult to calculate theoretically, but it can be estimated from the experimental value of the dielectric strength $\Delta\varepsilon$:

$$\Delta\varepsilon = \varepsilon_s - \varepsilon_\infty = \frac{1}{3\varepsilon_0} F g_K \frac{\mu^2 N}{k_B T V} \tag{2.19}$$

2.2 Dynamic response

When a time-dependent electric field $E(t) = E_0 exp(i\omega t)$ of angular frequency $\omega = 2\pi\nu$ is applied to a group of dipoles, both types of polarization (permanent and induced) are affected. While the induced polarization is very fast (between 10^{-17} and 10^{-14} seconds for the electronic polarization and between 10^{-13} and 10^{-12} seconds for the atomic polarization) and changes instantaneously with the field, the orientational polarization is slow (between 10^{3} and 10^{-12} seconds) and lags behind the changes in the electric field. This implies that only a certain time after the application of an external electric field will the maximum polarization in the material be reached (equilibrium state of the distribution of dipoles). Similarly, if the applied electric field is suddenly switched off, the polarization does not go to zero instantaneously (Figure 2.2). These phenomena occur because the dipole orientation can change only through certain interactions, for example collisions, with other dipoles. The time-delay necessary for a dielectric to respond to a change in the applied field is called characteristic relaxation time. The correlation decay function of the orientational polarization defined as:

$$\phi(t) = \frac{\mathbf{P}_O(t)}{\mathbf{P}_O(0)} = exp\left(\frac{-t}{\tau}\right) \tag{2.20}$$

usually has an exponentially decaying shape (Figure 2.2).

In the frequency domain, the linear relationship (constitutive equation) between the polarization, the displacement field and the macroscopic field may be written as:

$$\mathbf{P}(\omega) = \chi(\omega)\varepsilon_0\mathbf{E}(\omega) \Rightarrow \mathbf{D}(\omega) = \varepsilon_r(\omega)\varepsilon_0\mathbf{E}(\omega) \tag{2.21}$$

In this expression, χ and ε_r are not only functions of the frequency,

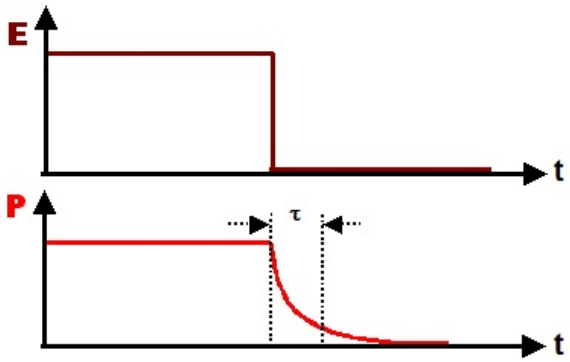

Figure 2.2: Time dependence of the electrical field E(t) and the corresponding polarization function P(t)

but they are moreover complex quantities. The function $\varepsilon_r(\omega)$ is the (complex) dielectric function of the material. The complex dielectric function is usually written as $\varepsilon^*(\omega) = \varepsilon'(\omega) - i\varepsilon''(\omega)$ The real part is called permittivity (since in the DC limit it becomes the real permittivity) and it is a measure of the energy stored in the oscillation of the dipolar units. The imaginary part is called dielectric loss because it is related to the energy dissipated in the material due to the internal friction. When plotted in logarithmic scale vs. $log(\omega)$, the graph of the imaginary part has the lineshape of an asymmetric peak whose maximum defines the relaxation time $\tau(T)$ as a function of the temperature of the system (Figure 2.3). The origin and shape of such loss peak, which we indicate as $\varepsilon_r(\omega)$, depend on the sample and on the type of molecular dynamics, and will be discussed further in the next section. From the loss peak it is possible to extract quantitative information about molecular dynamics and interactions. In correspondence with the loss peak, the real part displays a step like change whose height $\Delta\varepsilon = \varepsilon_s - \varepsilon_\infty$ is related with the dielectric strength, defined as the area under the loss peak. The quantity $\varepsilon_s = \lim_{\omega\tau \ll 1} \varepsilon'(\omega)$ is static permittivity and corresponds to the highest observable relative

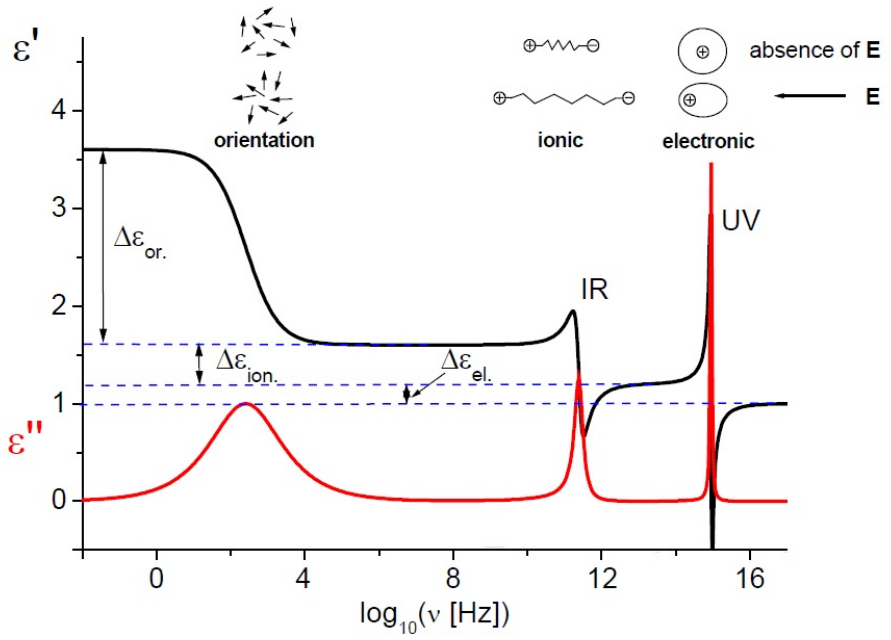

Figure 2.3: Types of polarization and real (ε') and imaginary (ε'') part of the complex dielectric function in the frequency domain.

permittivity and corresponds to the maximum value of the polarization. $\varepsilon_\infty = \lim_{\omega\tau \gg 1} \varepsilon'(\omega)$ is the relative permittivity measured just after the electric field is applied (short time means very high frequencies). This so-called relaxed permittivity represents the contribution to the overall polarization due only to deformational effects (electronic and atomic).

At very low frequencies (DC limit) it is necessary to take into account other phenomena because in this regime also the movement of charge carriers through the sample becomes important. This motion gives rise to the electrical conduction and to include it, it is necessary to add a conductivity contribution to the dielectric response of the material. The relationship between the complex dielectric permittivity and the complex

conductivity is, in general, given by:

$$\sigma^*(\omega) = i\omega\varepsilon_0\varepsilon^*(\omega) \tag{2.22}$$

To take into account the contribution of charge carriers it is necessary to add a term to the imaginary part of the dielectric permittivity:

$$\varepsilon^*(\omega) = \varepsilon_{or}(\omega) + \frac{\sigma_0}{(\varepsilon_0\omega)^s} \tag{2.23}$$

where ε_{or} contains the dielectric relaxation information, σ_0 is the DC electrical conductivity and s is a phenomenological exponent that is equal to 1 in the case of pure ohmic conduction (Figure 2.4(a)). In this case ($s = 1$) the real part of $\varepsilon^*(\omega)$ is independent of frequency in the DC regime.

Another effect related to the motion of charges is the electrode polarization effect (non-ohmic behaviour), which is visible as a large rise of $\varepsilon'(\omega)$ at low frequency (Figure 2.4(b)). This phenomena is caused by the mobile charge carriers that cannot cross the electrodes, and thus build up a charge layer at the electrode-sample interface when a slowly varying electric field is applied. This charge layer masks the electric field in the bulk of the sample and is responsible for the increase in $\varepsilon'(\omega)$ and the change of slope in the conductivity contribution to $\varepsilon''(\omega)$. Such electrode polarization effect does not yield useful information on the sample, and is normally excluded from the analysis.

2.3 Types of relaxations

2.3.1 The primary α relaxation

In the study of glass forming system, the most important dynamic process is the so-called primary α-relaxation process, which corresponds

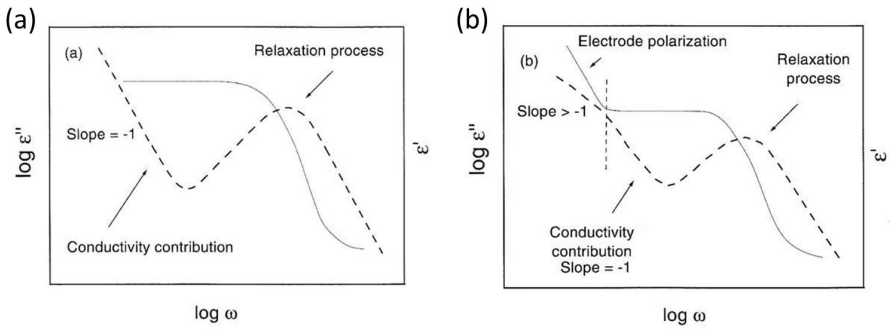

Figure 2.4: Scheme of the real ($\varepsilon'(\omega)$) and imaginary ($\varepsilon''(\omega)$) part of the complex dielectric permittivity for a relaxation process and an ohmic (a) or non-ohmic (b) conductivity. In the latter case the electrode polarization is considered [9].

to the structural cooperative and collective rearrangement of the constituent molecules and is closely associated with the glass transition. This structural loss peak (α peak) moves to higher frequency with increasing temperature. In general, the α relaxation differs from a Debye relaxation corresponding to a simple exponential function (see section 3.3.1), and it is described more accurately by a stretched exponential function (see section 3.3.4), whose width increases with decreasing temperature. This deviation from the simple to the stretched exponential function when a liquid is supercooled may be described in two ways:

1) the "cage effect", due to which molecular motions are slowed down by the presence of the other molecules in the surroundings. This phenomenon is already present in the liquid state and it becomes more important when the temperature decreases or the pressure increases, *i.e.*, when the density of the system increases. The intermolecular interactions result in non-equivalent molecular environments and therefore to a (more o less wide) distribution of relaxation times. Molecules with longer relaxation time are strongly interacting with their neighbours. Hence, on approaching

the glass transition their motion becomes more and more cooperative as the packing increases, resulting in yet longer relaxation times. On the other hand, molecules with shorter relaxation time (faster motion) interact only weakly with neighbouring molecules, being more or less free to move within a certain "cage" volume. The dynamics of the latter molecules is thus less affected by the freezing of the "cages". This difference explains the stretching as well as the increased temperature dependence of the relaxation times, which are dominated by the longer-time tail of the distribution [10].

2) the dynamic heterogeneity: the system is divided in clusters that are mutually independent and spatially separated from one another (typical cluster size several nm [11–14]). In each spatial domain, some molecules are faster than others but due to the mutual interactions the fast molecules can becomes slower and vice versa. The typical relaxation time differs from one domain to another. The average over all the different dynamic domains will lead to a distribution of relaxation times. From this idea, Ediger [15] proposed a spatially heterogeneous model of translational and rotational diffusion in supercooled liquids. The translational diffusion is found less temperature dependent than the rotational one and this decoupling could be due to the different effects that fast and slow motions have on translational and rotational diffusion, respectively. Thus, if spatial heterogeneity reflects into a given distribution of relaxation times for the α relaxation, wider is the distribution stronger is the decoupling between translational and rotational diffusion.

The Coupling Model (CM, see section 2.3.2.1) gives yet another explanation of these heterogeneities: glass-forming liquids are made of fundamental units packed together and interacting with each other.

It is clear from discussion that the structural relaxation of glass-

formers is a many-body relaxation problem. Although many-body relaxation remains an unsolved problem, some of its characteristics, such as the stretched exponential lineshape of the correlation function of the α relaxation or the dynamic heterogeneity of the relaxation, are manifested in experiments.

2.3.2 The secondary relaxation processes

Processes occurring in addition to the primary structural relaxation and at shorter times are called secondary or β relaxations (or γ, δ,... relaxations if there are more than one). These secondary relaxations, which usually exhibit smaller strength than the α process, can be divided in slow and fast β relaxations, depending on whether they display similar or much shorter relaxation times than the α process.

The typical phenomenology of slow secondary processes is: an Arrhenius temperature dependence of the relaxation time; the persistence of the mode in the glassy state below T_g and wide and symmetric loss profiles described often by the Cole-Cole function (see section 3.3.2). This slow kind of β process is often due to the motion of polar side groups or to some internal change of the molecular conformation. However, Johari and Goldstein [16] demonstrated that slow β relaxations can appear also in rigid molecules, where internal modes are absent and they are also present in polymers without rotable side group [17]. This kind of slow β relaxation, which is related to the glassy state of the material, is called JG β relaxation to distinguish it from the one due to internal motions. The JG β relaxation has been observed in many glass-former materials such as, for example, propylene glycol [18], diethylphtalate [19] and benzophenone (see Figure 2.5) [20], or in the plastic crystalline mixture of 60% succinonitrile and 40% glutaronitrile [21], or in the pharmaceutical products such

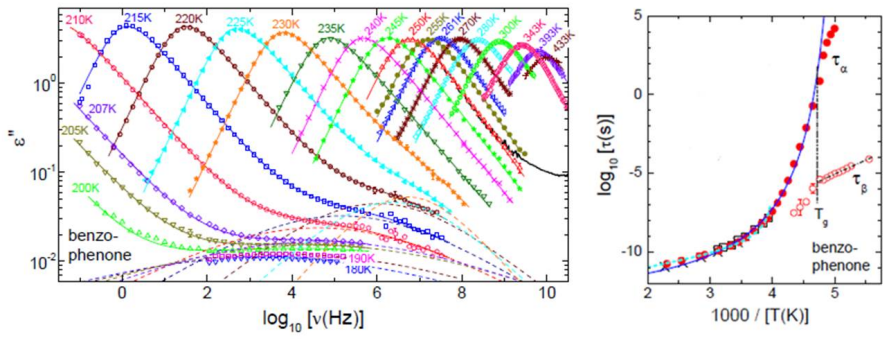

Figure 2.5: Left: dielectric loss spectra of benzophenone for various temperature. Right: relaxation times determined from the fits of the dielectric loss spectra. [20].

as indomethacin [22], acetyl salycilic acid [23] or ibuprophen [24].

Some experiments show that the JG β relaxation has a fixed frequency separation from the α relaxation: by applying pressure and raising temperature to maintain τ_α constant it was found that the ratio τ_{JG}/τ_α is invariant for different (T,P) conditions. This was found, for example, in benzoin-isobutylether [25] and diglycidyl ether of bisphenol A [26], or in binary mixtures such as 10% of quinaldine in tristyrene [27]. Figure 2.6 shows the superposition of the loss spectra of 10% quinaldine in tristyrene for different T and P combinations giving the same relaxation time τ_α: the position of the β peak with respect to the α one is not changing by changing the (T,P) conditions. The only difference in the spectra is the strength of the secondary peak, that increases slightly by increasing pressure and temperature. This may be due to the fact that the change in temperature (thermal energy) affects the dynamics more than the change in pressure (compression), leading to enhanced molecular motions.

At present there is no common accepted explanation about the microscopic origin of this JG relaxation. One possible explanation is in

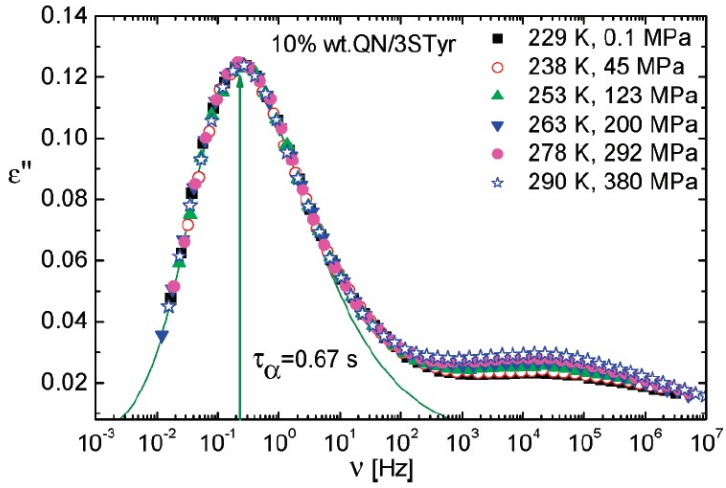

Figure 2.6: Superposition of the loss spectra of 10% quinaldine in tristyrene for different T and P combinations with the same relaxation time τ_α [27].

terms of so-called "islands of mobility", *i.e.*, locals regions in which the molecules have higher mobility thus giving rise to the β relaxation [16]. According to a different view (see below), all the molecules contribute to the secondary relaxation, which originates from motions taking place on a smaller length scale than the α relaxation [28–31].

Figure 2.7 provides a schematic view of the frequency dependence of the dielectric loss in glass-forming materials near the glass temperature T_g. The intense peak on the left corresponds to the α relaxation. Instead of a well-defined β-relaxation peak (Figure 2.7(b)), only an asymmetric tail may be visible in the spectrum at the high-frequency flank of the α peak (Figure 2.7(a)). This feature is know as "excess wing" [32] and it appears as an excess intensity at the high-frequency side of the α peak. An example is shown in Figure 2.8 where the dielectric spectra of propylene carbonate are reported [33].

Similarly to the case of the β relaxation, the origin of the excess wing

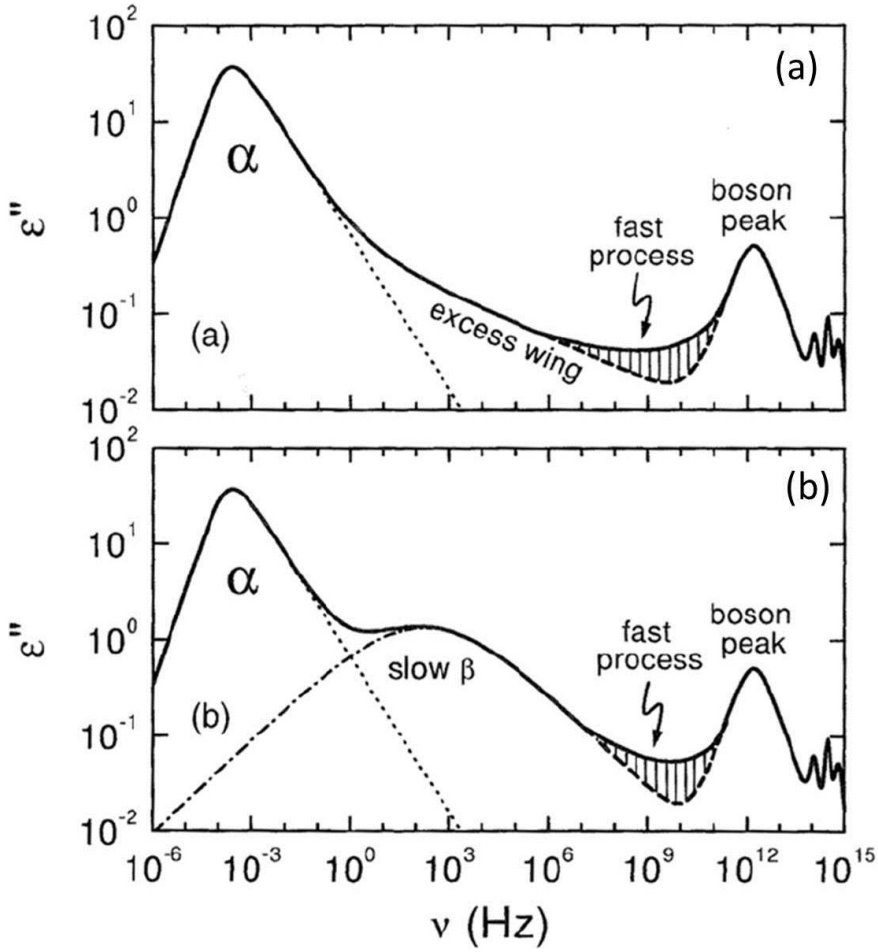

Figure 2.7: Schematic representation of the frequency dependence of the dielectric loss for a supercooled material near T_g. The response of a glass former is represented in (a) showing an excess wing; in (b) showing a well-defined β-relaxation peak [9].

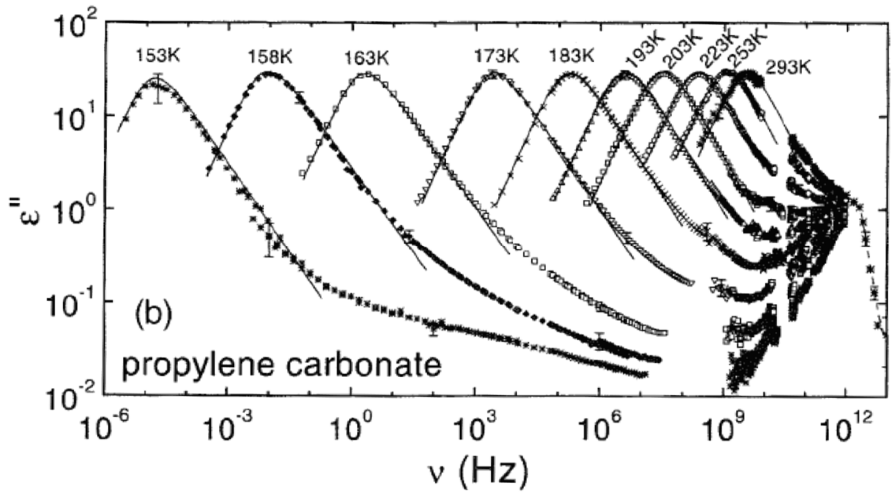

Figure 2.8: Frequency dependence of the imaginary part of the dielectric permittivity in propylene-carbonate at various temperature [33].

is highly debated. Both features have in common that they are rather universal and it seems that each glass-forming material displays one of the two processes or both as in the case, for example, of 1,4-polyisoprene (see Figure 2.9 [34]). Hence it can be assumed that the two features have the same origin and that the excess wing simply arises from a β-relaxation peak that is partially hidden under the α peak. Indeed, new evidence obtained by aging measurements [35] and by the application of pressure [36, 37] indicates that the excess wing can be ascribed to a secondary relaxation process. However, it is still a matter of debate whether it is a JG β relaxation [18, 35] or a distinct slow β process [38, 39].

An additional spectral contribution, called "fast β relaxation", is sometimes visible at very high frequencies (100MHz-1THz, see Figure 2.10). This fast process, predicted by the Mode Coupling Theory (section 1.2.1) [41–45], is thought to arise from a "rattling" movement of a particle in the "cage" formed by its neighbours. Evidence of this fast process was

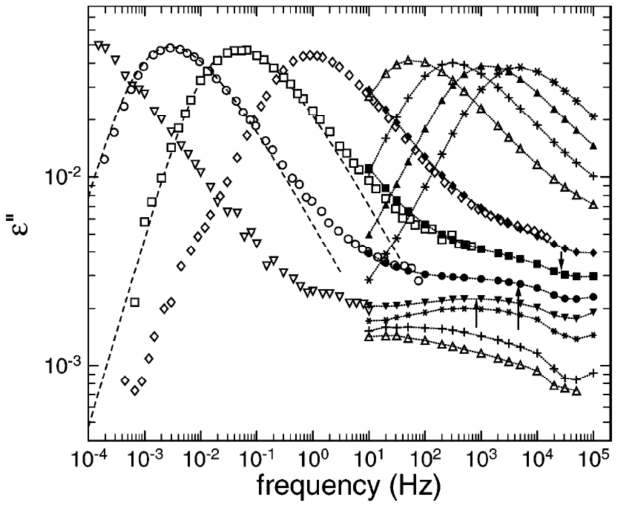

Figure 2.9: Dielectric loss spectra of 1,4-polyisoprene at different temperatures showing the presence of the excess wing together with the JG relaxation [34].

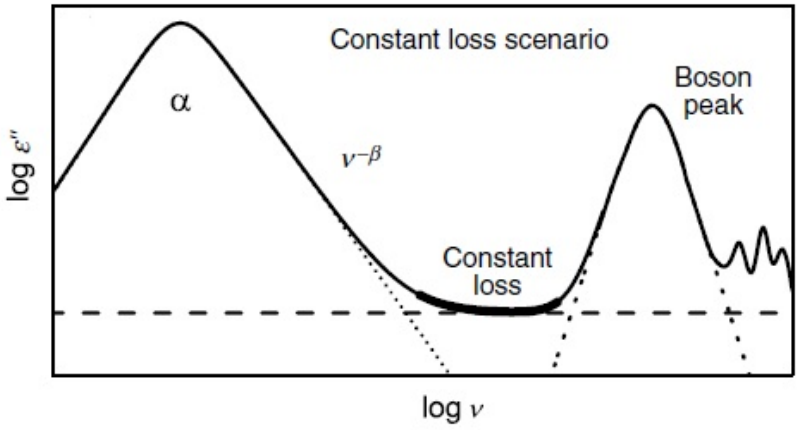

Figure 2.10: Schematic loss spectra in a constant loss scenario explaining the excess intensity in the gigahertz-terahertz region [40].

obtained mainly by scattering methods [46–49], as performing dielectric spectroscopy measurements at such high frequencies is quite challenging. Nevertheless, technical advances have allowed to perform dielectric measurements in this frequency range allowing the detection of fast glassy dynamics also with this technique [33, 50–54].

Beyond the minimum in the terahertz frequency region, another peak, called the Boson peak, is observed (Figure 2.10). At the moment there are no satisfactory explanations of the origin of this feature, although it appears in the frequency range corresponding to inter-atomic vibrations and might therefore be related to collective vibrational modes of the system. Several models have been proposed to explain its existence, among others the MCT [55].

2.3.2.1 The Coupling Model

Glass-forming materials (as any solid phase) consist of fundamental units that are densily-packed together and strongly interacting. This means that relaxation and diffusion in these systems can be described as many-body processes. While a many-body theory of the glass transition is still lacking, there are a lot of experimental evidences to support the many-body interpretation of the relaxation dynamics. An example is the spectral lineshape of the structural α relaxation which can be described with the stretched Kohlraush correlation function [56]:

$$\phi(t) = exp\left[-\left(\frac{t}{\tau_\alpha}\right)^{1-n}\right], 0 < n < 1 \tag{2.24}$$

The stretch exponent n appearing into Eq. 2.24 can be used as a measure of the cooperativity of the many-body relaxation dynamics. This exponent is related to the Kohlrausch-Williams-Watts exponent β_{KWW} as $n = 1 - \beta_{KWW}$ (see section 3.3.4).

The Coupling Model (CM) is able to account for the properties of the structural α relaxation originating from the many-body relaxation, and provides an explanation to the existence of a slow (JG) β relaxation in systems with no internal degrees of freedom, in terms of a "precursor" relaxation called primitive secondary relaxation. According to the CM, the many-body cooperative molecular dynamics evolve and develop as a function of time. Starting from the primitive (JG) relaxation, the number of molecules involved in the dynamics increases, building a many-body heterogeneous cluster. The final stage is the cooperative α relaxation, with the participation of a maximum possible number of molecules (determined by the intermolecular interactions and by the pressure and the temperature of the glass-former) [57–62].

In this model it is assumed that the many-body relaxation (characterized by a stretched Kohlrausch correlation function) starts at a time t_c which is determined by the interaction and is insensitive to temperature [57–60, 63]. Before t_c, the relaxation has an exponential correlation function $exp(-t/\tau_0)$, where τ_0 is the primitive relaxation time. From experiments [63, 64], molecular dynamics simulations [65], and solutions of simple models [57–60], it appears that the crossover from $exp(-t/\tau_0)$ to $exp[-(t/\tau_\alpha)^{1-n}]$ happens at a time $t_c = 2ps$. In the CM, the terminal α-relaxation time follows the equation [66]:

$$\tau_\alpha = [t_c^{-n}\tau_0]^{1/1-n} \tag{2.25}$$

where t_c is the crossover time, τ_0 is the primitive relaxation time and n is the correlation exponent equal to $1 - \beta_{KWW}$.

According to the Coupling Model, the primitive relaxation that initiates the evolution of the many-body dynamics should also be observed as JG secondary relaxation. The JG relaxation has a relaxation time, τ_{JG},

with dynamic properties that are correlated with that of the α-relaxation time τ_α [67–74] which would confirm the interpretation of the JG as precursor of the α relaxation. This fact, together with the local nature of the relaxation and the involvement of the entire molecule in the relaxation, are the characteristics that can be used to distinguish the JG relaxation from the other kind of (intramolecular) secondary relaxations. The relation between the primitive relaxation time τ_0 and τ_{JG} is simply:

$$\tau_{JG} \approx \tau_0 = t_C^n(\tau_\alpha)^{1-n} \tag{2.26}$$

The relation $\tau_{JG} \approx \tau_0$ holds experimentally for many small molecular and polymeric glass-formers, with τ_{JG} calculated from experimental results and τ_0 obtained by calculations [67–74]. This last equation can be rewritten as:

$$log(\tau_\alpha) - log(\tau_{JG}) = n(11.7 + log(\tau_\alpha)) \tag{2.27}$$

indicating that the separation between τ_α and τ_{JG} in logarithmic scale is proportional to n at constant τ_α. By decreasing the temperature or by increasing the pressure, the molecular dynamics becomes more and more correlated, so that the width of the α feature increases and the value of β_{KWW} diminishes (or equivalently, n increases). According to eq. 2.27, this results in a bigger separation between the α and JG relaxations, allowing one to distinguish and separate both processes.

Considering that at temperature below T_g the relaxation time of the β relaxation follows an Arrhenius dependence, it is possible to calculate the activation energy of the β relaxation at $T_g$from the CM equation, as [75]:

$$\frac{E_{a_\beta}(T_g)}{RT_g} = 2.303[2 - 13.7n - log\tau_\infty] \tag{2.28}$$

where R is the gas constant, τ_∞ is the prefactor and n is the correlation exponent of the α relaxation.

Bibliography

[1] P. F. Mosotti *Bibl. Univ. Modena*, vol. 6, p. 193, 1847.

[2] R. Clausis, *Die mechanische Wärmelehre*, vol. II. 1879.

[3] C. J. F. Böttcher, *Theory of electric polarization: Dielectrics in Static Fields*, vol. I. Amsterdam: Elsevier Science Ltd, 1973.

[4] L. Onsager *J. Am. Chem. Soc.*, vol. 58, p. 1486, 1936.

[5] J. G. Kirkwood *J. Chem. Phys.*, vol. 58, p. 911, 1939.

[6] J. G. Kirkwood *Ann. NY Acad. Sci.*, vol. 40, p. 315, 1940.

[7] J. G. Kirkwood *Trans. Faraday Soc.*, vol. 42A, p. 7, 1946.

[8] H. Fröhlich, *Theory of Dielectrics.* London: Oxford Univ. Press, 1958.

[9] F. Kremer and A. Schönhals, *Broadband Dielectric Spectroscopy.* Berlin: Springer, 2002.

[10] H. Sillescu *J. Non-Cryst. Solids*, vol. 243, p. 81, 1999.

[11] S. A. Reinsberg, X. H. Qiu, M. Wilhelm, H. W. Spiess, and M. D. Ediger *J. Chem. Phys.*, vol. 114, p. 7299, 2001.

[12] X. H. Qiu and M. D. Ediger *J. Chem. Phys. B*, vol. 107, p. 459, 2003.

[13] S. A. Reinsberg, A. Heuer, B. Doliwa, H. Zimmermann, and H. W. Spiess *J. Non-Cryst. Solids*, vol. 307, p. 208, 2002.

[14] R. Richert *J. Non-Cryst. Solids*, vol. 351, p. 2716, 2005.

[15] M. D. Ediger *Ann. Rev. Phys. Chem.*, vol. 51, p. 99, 2000.

[16] G. P. Johari and M. Goldstein *J. Chem. Phys.*, vol. 53, p. 2372, 1970.

[17] N. G. McCrum, B. E. Read, and G. Williams, *Anelastic and dielectric effects in polymeric solids.* New York: Dover Publications, 1991.

[18] K. L. Ngai, P. Lunkenheimer, C. León, U. Schneider, R. Brand, and A. Loidl *J. Chem. Phys.*, vol. 115, p. 1405, 2001.

[19] S. Pawlus, M. Paluch, M. Sekula, K. L. Ngai, S. J. Rzoska, and J. Ziolo *Phy. Rev. E*, vol. 68, p. 021503, 2003.

[20] P. Lunkenheimer, L. C. Pardo, M. Köhler, and A. Loidl *Phy. Rev. E*, vol. 77, p. 031506, 2008.

[21] T. Bauer, M. K$'$ohler, P. Lunkenheimer, A. Loidl, and C. A. Angell *J. Chem. Phys.*, vol. 133, p. 144509, 2010.

[22] Z. Wojnarowska, K. Adrjanowicz, P. Wlodarczyk, E. Kaminska, K. Kaminski, K. Grzybowska, R. Wrzalik, M. Paluch, and K. L. Ngai *J. Phys. Chem. B*, vol. 113, p. 12536, 2009.

[23] R. Nath, A. Nowaczyk, B. Geil, and R. Böhmer *J. Non-Cryst. Solids*, vol. 353, p. 3788, 2007.

[24] K. Adrjanowicz, K. Kaminski, Z. Wojnarowska, M. Dulski, L. Hawelek, S. Pawlus, M. Paluch, and W. Sawicki *J. Phys. Chem. B*, vol. 114, p. 6579, 2010.

[25] S. Capaccioli, D. Prevosto, M. Lucchesi, P. Rolla, R. Casalini, and K. L. Ngai *J. Non-Cryst. Solids*, vol. 351, p. 2643, 2005.

[26] D. Prevosto, S. Capaccioli, M. Lucchesi, P. A. Rolla, and K. L. Ngai *J. Non-Cryst. Solids*, vol. 355, p. 705, 2009.

[27] K. Kessairi, S. Capaccioli, D. Prevosto, M. Lucchesi, S. Sharifi, and P. Rolla *J. Phys. Chem. B*, vol. 112, p. 4470, 2008.

[28] F. H. Stillinger *Science*, vol. 267, p. 1935, 1995.

[29] M. Vogel and E. Rössler *J. Chem. Phys.*, vol. 114, p. 5802, 2001.

[30] J. S. Harmon, M. D. Demetriou, W. L. Johnson, and K. Samwer *Phys. Rev. Lett.*, vol. 99, p. 135502, 2007.

[31] C. Gainaru, O. Lips, A. Troshagina, R. Kahlau, A. Brodin, F. Fujara, and E. A. Rössler *J. Chem. Phys.*, vol. 128, p. 174505, 2008.

[32] R. Brand, P. Lunkenheimer, U. Schneider, and A. Loidl *Phys. Rev. Lett.*, vol. 82, p. 1951, 1999.

[33] U. Schneider, P. Lunkenheimer, R. Brand, and A. Loidl *Phys. Rev. E*, vol. 59, p. 6924, 1999.

[34] C. M. Roland, M. J. Schroeder, J. J. Fontanella, and K. L. Ngai *Macromolecules*, vol. 37, p. 2630, 2004.

[35] U. Schneider, R. Brand, P. Lunkenheimer, and A. Loidl *Phys. Rev. Lett.*, vol. 84, p. 5560, 2000.

[36] A. Reiser, G. Kasper, and S. Hunklinger *Phys. Rev. Lett.*, vol. 92, p. 125701, 2004.

[37] S. Hensel-Bielowka, M. Paluch, and K. L. Ngai *J. Chem. Phys.*, vol. 123, p. 014502, 2005.

[38] A. Kudlik, S. Benkhof, T. Blochowicz, C. Tschirwitz, and E. Rössler *J. Mol. Struct.*, vol. 479, p. 201, 1999.

[39] S. Hensel-Bielowka and M. Paluch *Phys. Rev. Lett.*, vol. 89, p. 025704, 2002.

[40] P. G. Wolynes and V. Lubchenko, eds., *Structural Glasses and Supercooled Liquids: Theory, Experiment, and Applications.* John Wiley & Sons, 2012.

[41] U. Bengtzelius, W. Götze, and A. Sjölander *J. Phys. C*, vol. 17, p. 5915, 1984.

[42] E. Leutheusser *Phys. Rev. A*, vol. 29, p. 2765, 1984.

[43] W. Götze *Z. Physik B*, vol. 60, p. 195, 1985.

[44] W. Götze and L. Sjögren *Rep. Prog. Phys.*, vol. 55, p. 241, 1992.

[45] W. Götze, *Complex Dynamics of Glass-Forming Liquids.* Oxford: Oxford Univ. Press, 2009.

[46] G. Li, W. M. Du, X. K. Chen, and H. Z. Cummins *Phys. Rev. A*, vol. 45, p. 3867, 1992.

[47] G. Li, W. M. Du, A. Sakai, and H. Z. Cummins *Phys. Rev. A*, vol. 46, p. 3343, 1992.

[48] H. Z. Cummins, W. M. Du, M. Fuchs, W. Götze, S. Hildebrand, A. Latz, G. Li, and N. J. Tao *Phys. Rev. E*, vol. 47, p. 4223, 1993.

[49] J. Wuttke, J. Hernandez, G. Li, G. Coddens, H. Z. Cummins, F. Fujara, W. Petry, and H. Sillescu *Phys. Rev. Lett.*, vol. 72, p. 3052, 1994.

[50] P. Lunkenheimer, U. Schneider, R. Brand, and A. Loidl *Contemporany Physics*, vol. 41, p. 15, 2000.

[51] U. Schneider, P. Lunkenheimer, R. Brand, and A. Loidl *J. Non-Cryst. Solids*, vol. 235-237, p. 173, 1998.

[52] M. Köhler, P. Lunkenheimer, Y. Goncharov, R.Wehn, and A. Loidl *J. Non-Cryst. Solids*, vol. 356, p. 529, 2010.

[53] P. Lunkenheimer, A. Pimenov, M. Dressel, Y. G. Goncharov, R. Böhmer, and A. Loidl *Phys. Rev. Lett.*, vol. 77, p. 318, 1996.

[54] P. Lunkenheimer, A. Pimenov, and A. Loidl *Phys. Rev. Lett.*, vol. 78, p. 2995, 1997.

[55] W. Götze and M. R. Mayr *Phys. Rev. E*, vol. 61, p. 587, 2000.

[56] R. Kohlrausch *Pogg. Ann. Phys.*, vol. 12(3), p. 393, 1847.

[57] K. Ngai *Comment. Solid State Phys.*, vol. 9, p. 141, 1979.

[58] K. L. Ngai and K. Y. Tsang *Phys. Rev. E*, vol. 60, p. 4511, 1999.

[59] K. Y. Tsang and K. L. Ngai *Phys. Rev. E*, vol. 54, p. R3067, 1997.

[60] K. Y. Tsang and K. L. Ngai *Phys. Rev. E*, vol. 56, p. R17, 1997.

[61] K. L. Ngai *IEEE Trans. Dielectr. Electr. Insul.*, vol. 8, p. 329, 2001.

[62] K. L. Ngai *J. Non-Cryst. Solids*, vol. 351, p. 2635, 2005.

[63] K. L. Ngai and R. W. Rendell, *Supercooled Liquids, Advances and Novel Applications*, vol. 676 of *ACS Symposium Series*. Washington DC: American Chemical Society, 1997.

[64] J. Colmenero, A. Arbe, G. Coddens, B. Frick, C. Mijangos, and H. Reinecke *Phys. Rev. Lett.*, vol. 78, p. 1928, 1997.

[65] A. Neelakantan and J. K. Maranas *J. Chem. Phys.*, vol. 120, p. 465, 2004.

[66] K. L. Ngai *J. Non-Cryst. Solids*, vol. 353, p. 709, 2007.

[67] K. L. Ngai *J. Phys.: Condens. Mat.*, vol. 15, p. S1107, 2003.

[68] K. L. Ngai *J. Chem. Phys.*, vol. 109, p. 6982, 1998.

[69] K. L. Ngai, J. Habasaki, C. Leon, and A. Rivera *Z. Phys. Chem.*, vol. 219, p. 47, 2005.

[70] K. L. Ngai and M. Paluch *J. Chem. Phys.*, vol. 120, p. 857, 2004.

[71] C. M. Roland, M. J. Schroeder, J. J. Fontanella, and K. L. Ngai *Macromolecules*, vol. 37, p. 2630, 2004.

[72] S. Capaccioli, D. Prevosto, M. Lucchesi, P. A. Rolla, R. Casalini, and K. L. Ngai *Macromolecules*, vol. 351, p. 2643, 2005.

[73] K. L. Ngai, R. Casalini, S. Capaccioli, M. Paluch, and C. M. Roland *J. Phys. Chem. B*, vol. 109, p. 17356, 2005.

[74] D. Prevosto, S. Capaccioli, M. Lucchesi, P. A. Rolla, and K. L. Ngai *J. Chem. Phys.*, vol. 120, p. 4808, 2004.

[75] K. L. Ngai and S. Capaccioli *Phys. Rev. E*, vol. 69, p. 031501, 2004.

Chapter 3

EXPERIMENTAL TECHNIQUES AND DATA ANALYSIS

3.1 Experimental preliminary techniques

3.1.1 Differential Scanning Calorimetry

Differential scanning calorimetry (DSC) can be used for determining the transition temperature of characteristic phase transformations of a sample, such as melting (T_m) and crystallization as well as the glass transition (T_g). With DSC it is possible to measure the difference in the amount of heat required to increase the temperature of a sample and of a reference as a function of temperature, hence the transition enthalpy can be calculated. The reference has a well-defined heat capacity that varies slowly over the range of temperatures measured; indium is normally used as a standard for calibration of temperature and enthalpy changes. Both sample and reference are maintained at nearly the same temperat-

ure throughout the experiment. When the sample undergoes a physical transformation such as a phase transition it will need a bigger or lower heat flow than the reference to remain at the same temperature as the reference. Whether less or more heat must flow to the sample depends on whether the process is exothermic or endothermic. For example, as a solid sample melts to a liquid it will require an extra heat flow corresponding to the latent heat of transformation, because the phase transition from solid to liquid is a endothermic process. On the other hand, as the sample undergoes exothermic processes (such as crystallization) it releases energy in the form of heat. By observing the difference in heat flow between the sample and reference, differential scanning calorimetry is able to measure the amount of heat absorbed or released during such transitions [1, 2].

The DSC experiments were performed with a Q100 analyser from TA instruments equipped with a refrigerated cooling systems yielding an operating range from 183 to 823 K, with cooling/heating rates between 2 and 10 K/min. The sample atmosphere during DSC experiments is controlled by connecting purge gases (nitrogen or helium) to the setup and a mass flow controller is used to control the flow rate of the gas. The sample (with a mass between 0.5 and 40 mg) is placed in an aluminum pan (TA instruments) or in a high-pressure stainless steel pan with gold plated seal (Perkin-Elmer). The last one is used for materials that can react with the sample holder or in the case of samples with high vapour pressure.

An example of DSC thermogram is shown in Figure 3.1. The thermogram was acquired upon heating a glass. The glass transition is visible as a small variation (bump) in the baseline at T_g due to a change in the heat capacity of the sample (see inset). Above T_g the sample is in the supercooled liquid state. Upon further raising the temperature, an

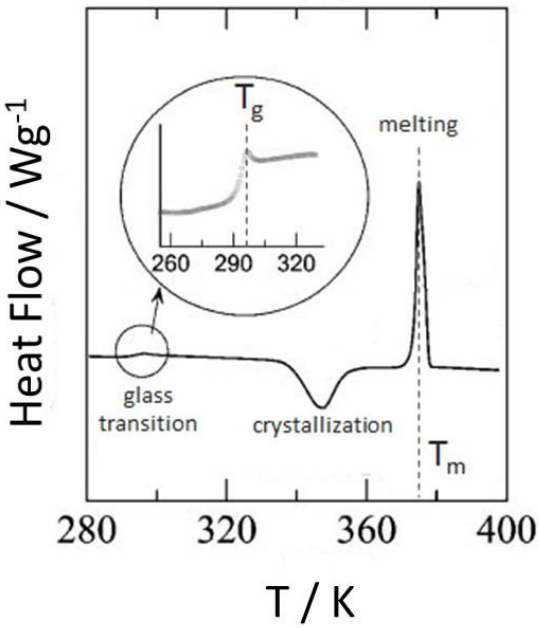

Figure 3.1: Example of a DSC thermogram in which the glass transition, the crystallization and the melting peaks are visible.

exothermic peak is observed, corresponding to the crystallization process (the supercooled liquid is not the stable phase below the melting temperature T_m). As the crystal phase is further heated, endothermic melting is observed at T_m.

3.1.2 Pressure-Volume-Temperature (PVT) measurements

The purpose of this kind of measurements is to measure volume changes in the sample by varying the pressure while maintaining the temperature constant. Figure 3.2 shows a scheme of the sample holder. The sample is melted inside a cylindrical cell made of stainless steel, which is then closed at its top part by a mobile piston. During the measurement any volume change of the sample causes a movement of the piston, which

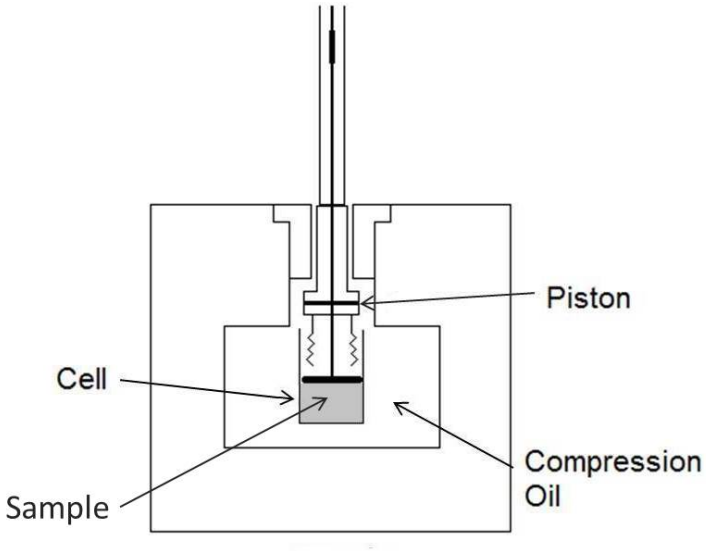

Figure 3.2: Scheme of the sample holder used for a PVT measurements.

induces a voltage difference in an induction coil that is recorded. By converting back this difference in voltage into physical displacement the volume change can be calculated. The pressure is increased gradually with a manual pump connected to the sample holder through a system of capillary lines filled with compression oil. The temperature is maintained fixed by a thermal bath with a liquid flow circuit connected to the sample holder with a working range between 185 and 473 K and it is controlled with an accuracy of 0.1 K. For every change in pressure the corresponding change in volume is recorded, and in this manner it is possible to create a volume-pressure graph at constant temperature.

3.1.3 X-ray powder diffraction

X-ray powder diffraction (XRD) is an analytical technique used for phase identification of a crystalline material. It can also provide information on unit cell parameters. X-ray diffractometers consist of three basic

elements: an x-ray tube, a sample holder and an x-ray detector. X-ray diffraction is based on the constructive interference of monochromatic X-rays diffracted by a crystalline sample. The x-rays are generated by a cathode ray tube, filtered to obtain monochromatic radiation and collimated to achieve a beam with a well defined direction, which impinges on the sample. The scattering of the incident rays from the sample yields constructive interference (and thus a diffraction peak) when Bragg's Law ($n\lambda = 2dsin\theta$) is satisfied. This law provides, for a given wavelength λ of electromagnetic radiation, the connection between the diffraction angle θ and the lattice spacing d along a particular crystallographic direction in the sample. The diffracted x-rays are then detected at different scattering angles to obtain an angular diffraction pattern. While a single crystal sample yields diffraction spots in well defined 3D directions, in a powdered sample the random orientation of crystalline domains results in a series of diffraction "cones", each one at a different scattering angle θ. By varying the scattering angle all possible diffraction directions of the lattice should be obtained, independently on the direction of rotation, due to the random orientation of the crystalline grains. From the conversion of the angular position θ of the diffraction peaks to d-spacings it is possible to identify the material's lattice symmetry as well as the lattice parameters.

The high-resolution X-ray powder diffraction profiles used in this work were recorded by means of a vertically mounted INEL cylindrical position-sensitive detector (CPS120). The detector was used in the Debye-Scherrer geometry (transmission mode), enabling simultaneous recording of the profile over a 2θ-range between 4° and 120° (angular step ca. 0.029° (2θ)). Monochromatic Cu Kα1 radiation ($\lambda = 1.54059$ Å) was selected with an asymmetrically focusing curved quartz monochromator. The generator power is commonly set to 35 kV and 35 mA. External calibration was

applied to convert the measured 4096 channels to 2θ-degrees, using a cubic spline fitting [3] of the diffraction pattern of the cubic phase of $Na_2Ca_2Al_2F_4$. Temperature control is achieved with a liquid nitrogen 700 series Cryostream Cooler from Oxford Cryosystems operating from 500 K to 90 K with a temperature accuracy of 0.1 K. The powder or liquid sample is placed into 0.5 mm-diameter Lindemann capillary at room temperature and is continuously rotated perpendicularly to the X-ray beam during data collection to minimize possible effects of preferred orientations. The peak positions are determined by pseudo-Voigt fits performed with dedicated software and in some cases Rietveld refinement is applied.

3.1.4 Fourier-transform infrared spectroscopy

Fourier-transform Infrared spectroscopy (FTIR) is an optical absorption spectroscopy technique in which an IR radiation is passed through a sample: some of the radiation is absorbed by the sample and some of it is transmitted through the sample. The resulting spectrum is an infrared spectrum of a sample with absorption peaks which correspond to the frequencies of vibrational modes involving a change in the dipolar character of intramolecular chemical bonds. Because each molecule is a unique combination of atoms, the IR spectrum is like a molecular fingerprint. Infrared spectroscopy can thus be used to identify the chemical composition of a material; the intensity of the peaks in the spectrum is a direct indication of the amount of each molecule present. FTIR can be employed to investigate the presence of impurities or of specific intermolecular bonds and supermolecular structures [4].

For the measurements presented in this work we used a Thermo Scientific Nicolet^{TM} 6700 FT-IR spectrometer with a spectral range

between 27000 and 15 cm^{-1} and a resolution of 0.01 cm^{-1}.

3.2 Broadband Dielectric Spectroscopy technique

3.2.1 Temperature dependent measurements

Dielectric spectroscopy is one of the most widely applied experimental tools for the investigation of glassy dynamics. The broad accessible frequency range (between 10^{-6} Hz and 10^{15} Hz) makes this technique suited to follow, for example, the slowing down of the $\alpha-$relaxation dynamics during the transition from the liquid to the solid glass state [5–7]. Dielectric spectroscopy is performed in the frequency domain and the measurements are carried out by varying the frequency of the applied AC field. Depending on the frequency range, different setups based on different measurement principles have to be used (Figure 3.3).

The measurements performed in this thesis covered the low frequency range between 10^{-2} Hz and 10^{7} Hz by using the Novocontrol Alpha-analyzer and the high frequency range from 10^{6} Hz to $1.8 \cdot 10^{9}$ Hz by using the Agilent HP4291 impedance analyzer.

With both setups the sample is placed in a capacitor cell and the quantity that is measured is the complex impedance $Z^*(\omega)$ of the sample from which the complex dielectric permittivity is obtained as:

$$\varepsilon^*(\omega) = \frac{1}{i\omega Z^*(\omega) C_0} \tag{3.1}$$

where C_0 is the vacuum capacitance of the capacitor where the sample is placed. At high (microwave) frequency the geometrical dimensions of the sample capacitor become important and different cells have to be used in the two different experimental setups.

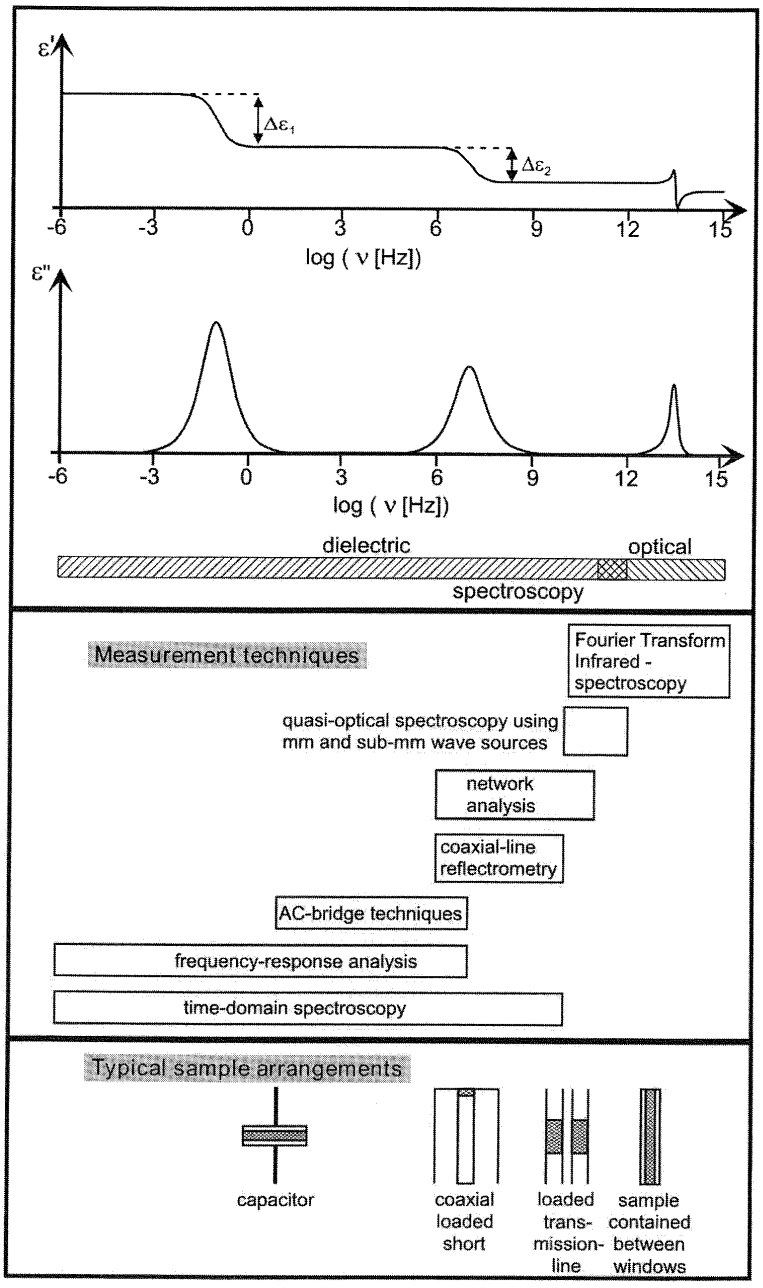

Figure 3.3: Types of measurements techniques and setups in the frequency range between 10^{-6} Hz and 10^{15} Hz [6].

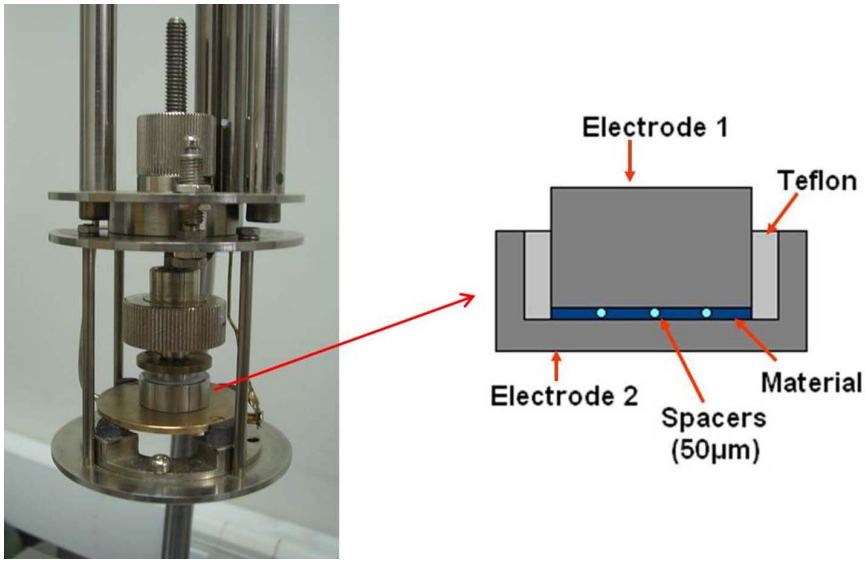

Figure 3.4: Picture of the sample holder with a scheme of the capacitor used for liquid samples.

For the Alpha-analyzer a parallel plate capacitor is used. In the case of liquid samples a special capacitor that can be filled directly with the material under investigation is used (Figure 3.4). For the detection of low dielectric loss, for example at low temperatures, small plate distances and large areas of the capacitor plate are necessary. By using glass fibres spacers it is possible to fix the distance between the plates at 50 nm and 100 nm. In the case of solid samples, the cell is prepared by pressing the material between to electrode plates by using an hydraulic press. The separation between both electrodes is determined by the pellet thickness and thus by the quantity of material which is being compressed. The capacitor filled with the sample is placed in a sample holder (Figure 3.4) and then inserted inside the cryostat.

The measurements in the high-frequency range are performed by using a coaxial reflection technique. The material under investigation is

placed in a small capacitor that is mounted at the end of a home-made coaxial line (Figure 3.5) that is connected to the test head of the HP4291 impedance analyzer. The electromagnetic wave travelling along the line is reflected by the sample and by current-voltage measurements it is possible to obtain the real part of the parallel capacitance C_p' and the real part of the conductance G' that are related to the real and imaginary part of the complex dielectric permittivity as follows:

$$\varepsilon' = \frac{C_p'}{C_0} \tag{3.2}$$

$$\varepsilon'' = \frac{G'}{C_0 2\pi\nu} \tag{3.3}$$

Here $C_0 = \varepsilon_0 S/d$ is the capacitance of the empty capacitor with electrodes of surface area S separated by a distance d; ε_0 is the vacuum permittivity and ν is the frequency.

In this technique the perfect construction of the coaxial line and the proper mounting of the sample are essential, and a careful calibration of the system is required in order to correct any contributions of the coaxial line itself and of the sample holder.

A scheme of the experimental station common to both setups is shown in Figure 3.6. The station allows controlling the sample temperatures by means of a nitrogen-gas heating/cooling stage.

In both low- and high-frequency measurements, temperature control is achieved using the Novocontrol Quatro Cryosystem, that consists of a cryostat in which the samples cell is placed, a gas heating unit, a liquid nitrogen vaporizing unit and a liquid nitrogen Dewar with pressure sensor and a vacuum system (Figure 3.6). The sample temperature is measured by using a Platinum resistor sensor (PT100) in thermal contact with one of the capacitor plates. The system can work in the temperature range

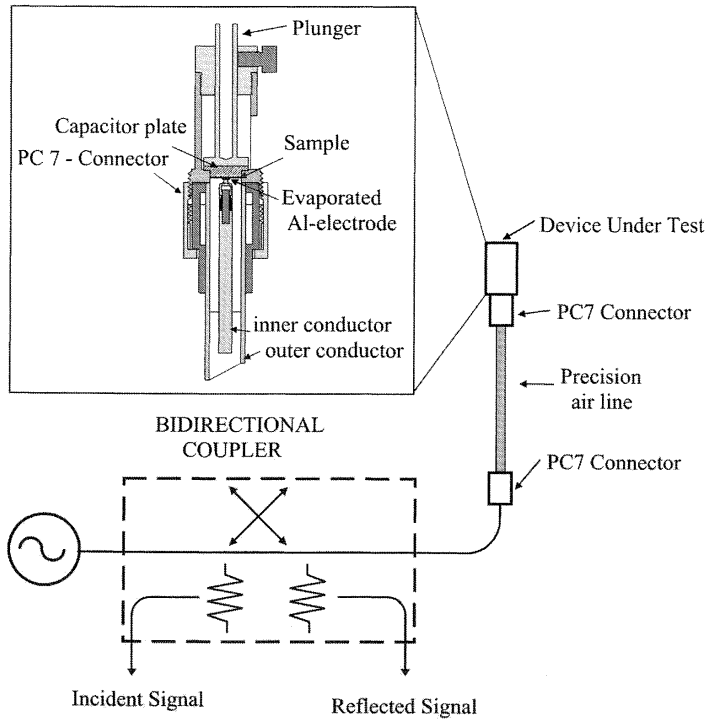

Figure 3.5: Scheme of the coaxial line used for high-frequency dielectric measurements [6].

between 116 K and 773 K with a precision of 0.01 K.

The Alpha-analyzer was also used with a second cryostat connected to a closed-cycle helium compressor (not shown). This cryostat, that originally was employed to produce liquid nitrogen, has been modified to use it as a vacuum chamber with temperature control. For this purpose I have designed a dedicated hermetic capacitor and I developed a home-made heating stage with temperature sensors. For the low-temperature measurements, I have assembled a vacuum chamber connecting it to the vacuum pump and compressor. For measurements at liquid helium temperatures the home-built capacitor is placed directly on the top of the cold finger inside the cryostat, which allows reaching a temperature

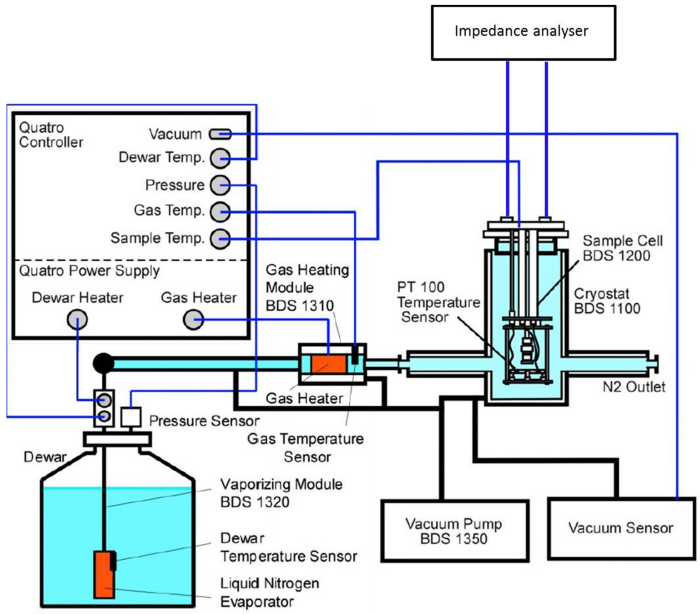

Figure 3.6: Experimental setup for temperature broadband dielectric measurements [8].

as low as 16 K. A silicon diode sensor, placed inside the cold finger and in thermal contact with the capacitor, is used to measure the temperature in a range between 16 and 320 K with an accuracy of ±12 mK.

3.2.2 Pressure dependent measurements

Pressure-dependent dielectric measurements were performed between ambient pressure and 0.6 GPa using the lower frequency Novocontrol Alpha-analyzer (10^{-2} Hz - 10^{7} Hz). The material under investigation is placed between two stainless steel parallel plates separated by silica spacers. To prevent the contamination with the pressurizing fluid (thermal fluid by Huber), the capacitor is covered by a Teflon membrane and latex wrapping. The sample is placed in a high-pressure chamber (by Unipress) made of a Cu-Be alloy, which is filled with the oil. The chamber is

connected to a manual pump with which it is possible to apply pressure from ambient value up to 0.6 GPa, and a pressure transducer with an accuracy of ±0.5% is used to measure it.

The temperature is controlled by a thermal bath (Lauda Proline RP 1290) with a liquid flow circuit connected to the high-pressure chamber. The working range of the bath is between 185 and 473 K and it is controlled with an accuracy of 0.02 K. In order to keep as stable as possible the temperature inside the chamber, it is necessary to insulate the chamber itself and all the connections between the chamber and the bath using foam material. In addition to the Lauda Proline bath, a Huber Unistat Thermal Control System has been used with a working temperature range between 198 and 523 K with a temperature stability of $\pm 0.01 K$. The experimental setup is schematized in Figure 3.7.

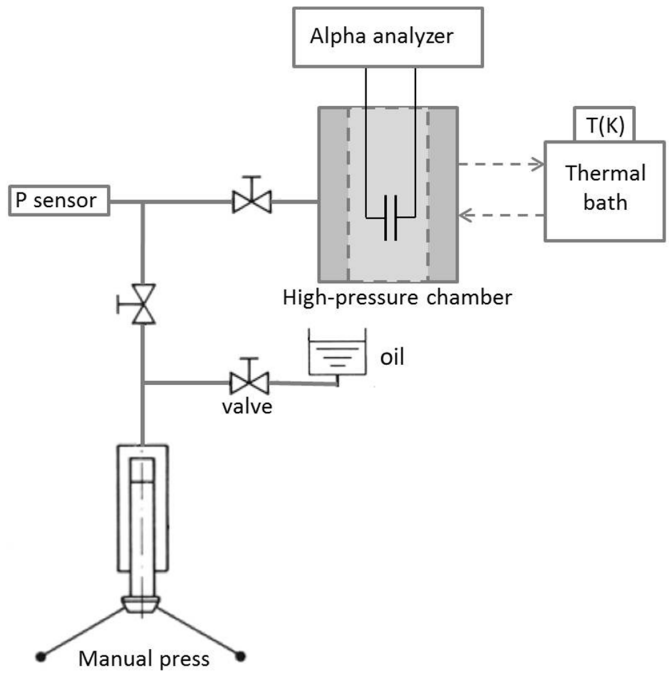

Figure 3.7: Experimental setup for the high-pressure dielectric measurements

3.3 Phenomenological relaxation models

Figure 3.8 represents a typical spectrum of the complex permittivity as measured with broadband dielectric spectroscopy, plotted in logarithmic scale both as real and imaginary part of the permittivity. In the imaginary part, the dielectric relaxation process (loss) is visible as a broad peak appearing in the radiofrequency range and spanning more than one decade. At low frequency, the imaginary part of the permittivity (loss spectrum) displays a background proportional to inverse frequency, which is due to electrical conductivity. The information about the dipolar dynamics is extracted from the loss peak by means of a fitting procedure.

There exist different models to describe the loss peak related to a dielectric relaxation. The shape of the loss peak of a relaxation depends on the extent of the interactions that take place between dipoles. Different lineshape functions are then required to describe the loss feature in different cases.

3.3.1 Debye model

In 1929, Debye proposed that relaxation for a dipolar system in non-equilibrium takes place with a rate that increases linearly with the distance from equilibrium. This behaviour can be described with the following first order differential equation [9]:

$$\frac{dP(t)}{dt} = -\frac{P(t)}{\tau_D} \tag{3.4}$$

where τ_D is a characteristic relaxation time. Equation 3.4 leads to an exponential decay of the correlation decay function:

$$\phi(t) = exp\left(-\frac{t}{\tau_D}\right) \tag{3.5}$$

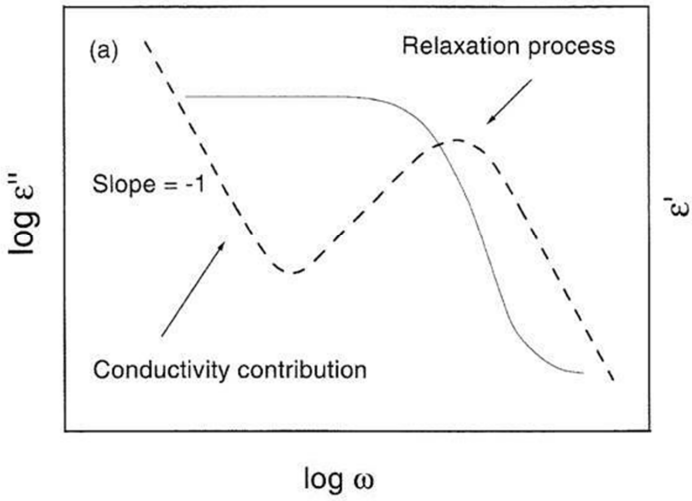

Figure 3.8: Real and imaginary part of the complex permittivity of a typical spectrum as measured with broadband dielectric spectroscopy [6].

This is valid under the following assumptions: a) the dipoles are non-interacting, b)the equilibrium is reached with only one type of process, c) all the dipoles are equivalent, this means that all of them relax with only one characteristic time. The complex permittivity in the frequency domain has the form [10]:

$$\varepsilon_D(\omega) = \epsilon_\infty + \frac{(\epsilon_s - \epsilon_\infty)}{1 + i\omega\tau_D} \tag{3.6}$$

The real and imaginary part of the complex permittivity can be separated as:

$$\varepsilon' = \epsilon_\infty + \frac{\Delta\epsilon}{1 + (\omega\tau_D)^2} \tag{3.7}$$

$$\varepsilon'' = \Delta\epsilon \frac{\omega\tau_D}{1 + (\omega\tau_D)^2} \tag{3.8}$$

The imaginary part gives rise to a symmetric loss peak with half width of 1.14 decades (Figure 3.9).

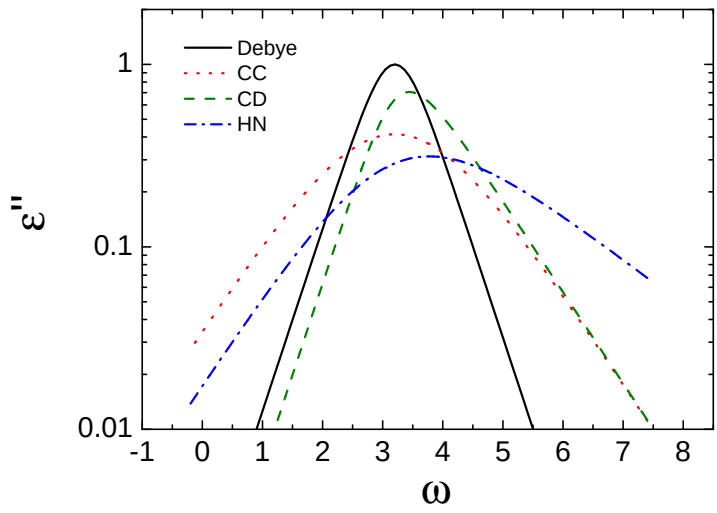

Figure 3.9: Immaginary part of the dielectric permittivity for Debye, Cole-Cole (CC), Cole-Davidson (CD) and Havriliak-Negami (HN) equations

Derived within certain models for molecular reorientation, e.g., isotropic rotational diffusion [6], the Debye relaxation is not suited to describe the dielectric response of glass-forming liquids. Other semi-empirical expressions have been introduced to add an additional stretching parameter or asymmetry to interpolate the relaxation peaks.

3.3.2 The Cole-Cole and the Cole-Davidson function

In most cases the experimental half-width is much broader than predicted by the Debye equation. This broadening can be described by the Cole-Cole (CC) function (Figure 3.9) [11]:

$$\varepsilon_{CC}(\omega) = \epsilon_\infty + \frac{(\epsilon_s - \epsilon_\infty)}{1 + (i\omega\tau_{CC})^\alpha} \tag{3.9}$$

The real and imaginary part of the complex permittivity can be written as:

$$\varepsilon'(\omega) = \epsilon_\infty + \frac{\Delta\epsilon(1+\omega\tau_{CC})^\alpha \cos(\alpha\pi/2)}{1+2(\omega\tau_{CC})^\alpha \cos(\alpha\pi/2)+(\omega\tau_{CC})^{2\alpha}} \tag{3.10}$$

$$\varepsilon''(\omega) = \Delta\epsilon \frac{(\omega\tau_{CC})^\alpha \sin(\alpha\pi/2)}{1+2(\omega\tau_{CC})^\alpha \cos(\alpha\pi/2)+(\omega\tau_{CC})^{2\alpha}} \tag{3.11}$$

where $0 < \alpha \leq 1$ leads to a symmetrical broadening of the relaxation function. For $\alpha = 1$ the Debye function is obtained. The position of maximal loss is related to the Cole-Cole relaxation time by the relation $\omega_{max} = 1/\tau_{CC}$. Many experimental results, especially on liquids or molecular glass forming materials, show that the complex permittivity function can have an asymmetric broadening (Figure 3.9). This behaviour is better described by the Cole-Davidson equation, introduced in 1950 by Davidson and Cole [12]:

$$\varepsilon_{CD}(\omega) = \epsilon_\infty + \frac{(\epsilon_s - \epsilon_\infty)}{(1+i\omega\tau_{CD})^\beta} \tag{3.12}$$

and it can be separated in the real and imaginary part as follow:

$$\varepsilon'(\omega) = \epsilon_\infty + \Delta\epsilon \cos(\phi)^\beta \cos(\beta\phi) \tag{3.13}$$

$$\varepsilon''(\omega) = \Delta\epsilon \cos(\phi)^\beta \sin(\beta\phi) \tag{3.14}$$

with $\tan\phi = \omega\tau_{CD}$ and $0 < \beta \leq 1$. The CD function gives an asymmetrically broadened peak for the imaginary part $\varepsilon''(\omega)$) with a power-law proportional with ω on the low frequency side and another proportional with $\omega^{-\beta}$ on the high frequency side. Again, for $\beta = 1$ the Debye function is obtained. For an asymmetric model function the Cole-Davidson time parameter τ_{CD} of the model does not coincide with the relaxation time related to the maximal loss. The relation between these two quantities depends on the shape parameter β as follows:

$$\omega_{max} = \frac{1}{\tau_{CD}} \tan\left[\frac{\pi}{2\beta+2}\right] \tag{3.15}$$

3.3.3 The Havriliak-Negami function

A more general function to model the relaxation response is the Havriliak-Negami (HN)function defined as [13, 14]:

$$\varepsilon_{HN}(\omega) = \varepsilon_\infty + \frac{(\varepsilon_s - \varepsilon_\infty)}{[1 + (i\omega\tau_{HN})^\alpha]^\beta} \tag{3.16}$$

where α and β are the shape parameters with values between 0 and 1 (see Figure 3.9). The separation of the real and imaginary part of the complex permittivity gives rather complex expressions:

$$\begin{aligned}\varepsilon'(\omega) = \varepsilon_\infty + \Delta\varepsilon \left[1 + 2(\omega\tau_{HN})^\alpha \cos\left(\frac{\alpha\pi}{2}\right) + (\omega\tau_{HN})^{2\alpha}\right]^{-\beta/2} \\ \cdot \cos\left[\beta \arctan\left(\frac{sin(\alpha\pi/2)}{(\omega\tau_{HN})^{-\alpha} + \cos(\beta\pi/2)}\right)\right]\end{aligned} \tag{3.17}$$

$$\begin{aligned}\varepsilon''(\omega) = \Delta\varepsilon \left[1 + 2(\omega\tau_{HN})^\alpha \cos\left(\frac{\alpha\pi}{2}\right) + (\omega\tau_{HN})^{2\alpha}\right]^{-\beta/2} \\ \cdot \sin\left[\beta \arctan\left(\frac{sin(\alpha\pi/2)}{(\omega\tau_{HN})^{-\alpha} + \cos(\beta\pi/2)}\right)\right]\end{aligned} \tag{3.18}$$

It is worth noticing that the HN function is a combination of the CC ($\beta = 1$) and CD ($\alpha = 1$) functions and it reduces to the Debye behaviour for $\alpha = \beta = 1$. The frequency of maximal loss depends on the α, β and τ_{HN} parameters and is given by:

$$\omega_{max} = \frac{1}{\tau_{HN}} \left[\sin\frac{\alpha\pi}{2\beta+2}\right]^{1/\alpha} \left[\sin\frac{\alpha\beta\pi}{2\beta+2}\right]^{-1/\alpha} \tag{3.19}$$

Usually, only the HN function is able to describe the experimental data in the whole frequency range of BDS. This means that for a complete description of the frequency behaviour of a relaxation region, at least a

set of four parameters is needed. If several relaxation regions are observed in the measured frequency window, a combination of several HN functions can be used to describe and separate the different processes. Provided that the different relaxation regions are independent and hence that the contribution of each process to the complex dielectric function is additive, the total dielectric function will be given by $\sum_k \varepsilon_{HN,k}(\omega_i)$, where k runs over all the relaxation processes.

3.3.4 The Kohlrausch-Williams-Watts function

In the time domain, the decay function $\phi(t)$ is more stretched than the simple exponential function that would correspond to a Debye process. To model this non-exponential character it is possible to use the Kohlrausch-Williams-Watts (KWW) function, introduced by Kohlrausch in 1847 [15] and modified by Williams and Watts to describe relaxation processes in polymers [16]. The KWW equation for the permittivity in the time domain is:

$$\varepsilon_{KWW}(t) = \varepsilon_\infty + \Delta\varepsilon \left[1 - exp\left(-\frac{t}{\tau_{KWW}} \right)^{\beta_{KWW}} \right] \tag{3.20}$$

where β_{KWW} is the so-called stretching exponent which has values between 0 and 1. The KWW function has no analytic Fourier transform in the frequency domain. There exists however an approximate connection between the HN function and the KWW expression. In particular it has been shown that approximate relations hold between the HN shape parameters α and β and the stretching parameter β_{KWW}, as well as between the corresponding relaxation times. The two relationships are [17]:

$$\beta_{KWW} = (\alpha\beta)^{1/1.23} \tag{3.21}$$

$$\ln\left(\frac{\tau_{HN}}{\tau_{KWW}}\right) = 2.6(1-\beta_{KWW})^{1/2} exp(-3\beta_{KWW}) \tag{3.22}$$

The equivalence between the KWW and the HN functions can be studied by using an alternative method than the analytical Fourier transformation. Dielectric measurements can be performed to study the α relaxation either directly in the time domain (with the transient currents method) [18, 19] or in the frequency domain (with the broadband dielectric spectroscopy). Both experiments have been carried out for poly(hydroxy ether of bisphenol-A) [17] and the equations 3.21 and 3.22 have been indeed proven to be valid.

Bibliography

[1] E. Pungor, *A practical guide to instrumental analysis*. Florida: Boca Raton, 1995.

[2] D. A. Skoog, F. J. Holler, and T. A. Nieman, *Principles of instrumental analysis*. Boston: Thomson Learning, 1998.

[3] M. Evain, P. Deniard, A. Jouanneaux, and R. Brec *J. Appl. Cryst.*, vol. 26, p. 563, 1993.

[4] P. Griffiths and J. A. De Haseth, *Fourier Transform Infrared Spectrometry*. Hoboken, NJ: John Wiley & Sons, 2007.

[5] P. Lunkenheimer, U. Schneider, R. Brand, and A. Loidl *Contemporany Physics*, vol. 41, p. 15, 2000.

[6] F. Kremer and A. Schönhals, *Broadband Dielectric Spectroscopy*. Berlin: Springer, 2002.

[7] P. Lunkenheimer and A. Loidl *Chem. Phys.*, vol. 284, p. 205, 2002.

[8] `http://www.novocontrol.de/`.

[9] P. Debye, *Polar Molecules*. New York: Chem. Catalog., 1929.

[10] H. Fröhlich, *Theory of Dielectrics*. London: Oxford Univ. Press, 1958.

[11] K. S. Cole and R. H. Cole *J. Chem. Phys.*, vol. 9, p. 341, 1941.

[12] D. W. Davidson and R. H. Cole *J. Chem. Phys.*, vol. 18, p. 1417, 1950.

[13] S. Havrilliak and S. Negami *J. Polym. Sci C*, vol. 16, p. 99, 1966.

[14] S. Havrilliak and S. Negami *Polymer*, vol. 8, p. 161, 1967.

[15] R. Kohlrausch *Pogg. Ann. Phys.*, vol. 12(3), p. 393, 1847.

[16] G. Williams and W. D. C. *Trans. Faraday Soc.*, vol. 66, p. 80, 1970.

[17] A. Alvarez, A. Alegria, and J. Colmenero *Phys. Rev. B*, vol. 44, p. 7306, 1991.

[18] P. Hedvig, *Dielectric Spectroscopic of Polymers.* Bristol: Hilger, 1977.

[19] N. G. McCrum, B. E. Read, and G. Williams, *Anelastic and Dielectric Effects in Polymeric Solids.* London: Wiley, 1967.

Chapter 4

POLYMORPHISM AND DYNAMICS OF 2-ADAMANTANONE

4.1 Introduction

Diamondoid molecules are an attractive class of fully sp^3-hybridized hydrocarbons formed by three or more rigidly interlocked cyclohexane rings. They have recently received great interest due to their unique structures and their chemical and physical properties that make them promising candidates as building blocks for self-assembled processes in a huge number of applications [1–6]. The main interest is to build up organic crystals with large and tunable cavities giving rise to porous materials with the desired physical structure and chemical properties. The smallest diamondoid molecule is adamantane (of chemical formula $C_{10}H_{16}$), a rigid molecule with point group symmetry T_d formed by 10 carbon atoms arranged as a single diamond cage surrounded by 16

hydrogen atoms (see Figure 4.1(a)) [7]. Adamantane exhibits a series of thermally induced solid-solid phase transitions below the melting point, which are the consequence of the ability to gain rotational degrees of freedom in the crystalline state thanks to the low hindrance against rotational motions offered by its globular shape [8, 9]. The rotational motions of the molecules in the orientationally disordered (OD) phases take place among a finite set of distinct equilibrium orientations. Such dynamic disorder gives rise to high-vapour pressure and low entropy of fusion [10, 11].

2-adamantanone ($C_{10}H_{14}O$, hereinafter called 2A-O) is a rigid pseudo-globular molecule of C_{2v} symmetry obtained from adamantane by substitution of two hydrogen atoms by a carbonyl moiety (an oxygen atom linked to a carbon by a double bond, see Figure 4.1(b)). Although the presence of the polar oxygen moiety gives rise to a large dipole moment ($\mu = 3.4D$) parallel to the twofold symmetry axis [12, 13], which leads to relatively strong intermolecular interactions and to steric effects, this compound exhibits an OD high-temperature phase I below the melting point at 557 K [14]. Such OD phase I transforms to a metastable monoclinic phase II at about 178 K upon cooling. The transition is characterized by a large thermal hysteresis, being in fact observed at 205 K upon heating the low-temperature phase II [12, 14–16].

Butler *et al.* [16] submitted 2A-O to a thermal cycling at normal pressure between 150 and 250 K, i.e. across the transition between the phase II and the phase I. The result was an increase of the transition temperature from phase II to phase I from 205 K to 221 K, which actually means that a new low-temperature stable phase (phase III) appeared during cycling at the expense of the low-temperature metastable phase. The nature of such stable phase and the details of the phase diagram of

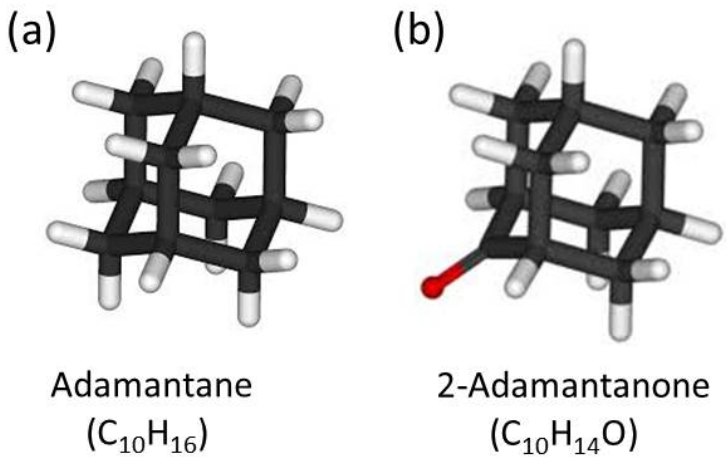

Figure 4.1: Molecular structure of (a) Adamantane and (b) 2-adamantanone

2A-O have been the subject of debate [16].

The phase diagram of 2A-O can be schematized as shown in Figure 4.2.

4.2 Experimental methods

The 2A-O was purchased from Aldrich Chemical Company, with purity of 99% and used as received.

In order to study the polymorphism of 2A-O, high-resolution X-ray measurements (see section 3.1.3) were performed from 90 to 205 K within phase II and from 210 to 400 K for OD phase I. Patterns were collected every 20 K and every 5 K around the low-temperature to the OD phase transition.

The broadband dielectric spectroscopy measurements (see section 3.2.1) were performed using a Novocontrol Alpha-analyzer (10^{-2} to 10^{7} Hz) and an HP4291 impedance analyzer (10^{6} to 10^{9} Hz), equipped with a Quatro temperature controller (± 0.1 K) working down to 100 K and a closed-cycle helium cryostat for lower temperatures. The capacitor was

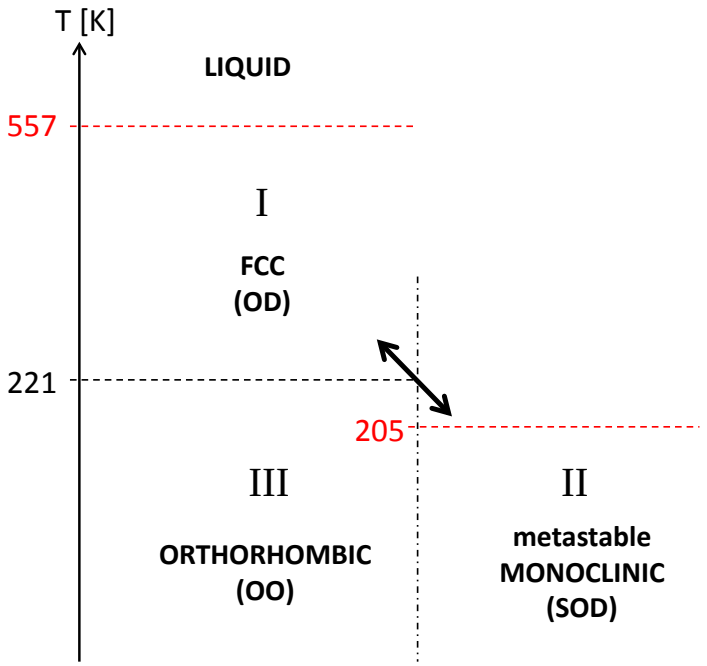

Figure 4.2: Temperature phase diagram of 2A-O. The left-hand side shows the thermodynamically stable phases, the right-hand side the metastable phase which is obtained from the fcc phase. Abbreviations: OD - orientational disorder; OO - Orientational order; SOD - Statistical orientational disorder.

prepared by pressing the 2A-O powder between two stainless steel disks using a hydraulic press (120 kN). The spectra were taken between 88 K and 222 K every 2 K in the low-frequency range and between 132 K and 220 K every 2 K in the high-frequency range.

4.3 Structural study

In this section, the crystal structures of stable and metastable phases of 2A-O are presented, together with the equilibrium pressure-temperature

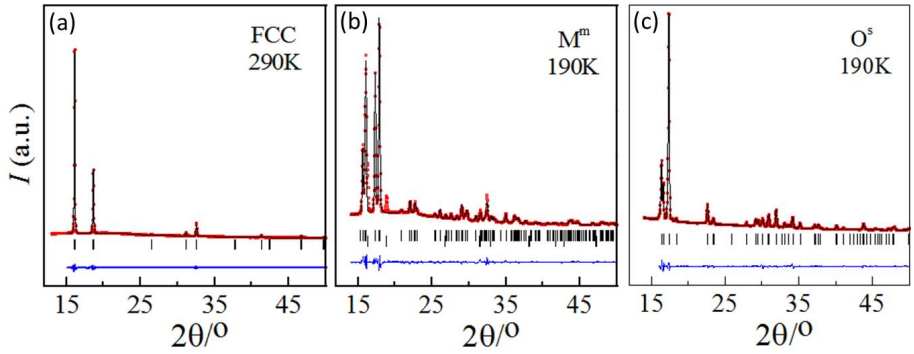

Figure 4.3: Experimental (red circles) and calculated (black line) diffraction patterns along with the difference profile (blue line) of a) fcc phase I at 290 K; b) metastable monoclinic phase II at 190 K; c) stable orthorhombic phase III at 190 K. Vertical bars indicate the calculated Bragg peak positions.

line characterizing the coexistence between the stable low-temperature and the OD phases. The stability of the various phases is compared.

Due to the rotational motions of the molecules, the OD phase I is highly symmetric, exhibiting a face-centred cubic (FCC) lattice with a XRD pattern characterized by relatively few diffraction peaks (Figure 4.3(a)). The fingerprint of phase I is visible in XRD above 205 K, temperature at which both phase I and phase II coexist in the diffraction profile (not shown). The dynamic disorder of this phase is associated with different types of molecular rotations: $2\pi/3$-rotations of the dipolar axis (C_3) along the six fourfold $\langle 001 \rangle$ cubic lattice directions, and $\pi/2$-jumps between two non-equivalent orientations about the C=O bond direction [17, 18].

The lattice of the metastable phase II of 2A-O was determined by Rietveld refinement to be monoclinic with space group $P2_1/c$, with 4 molecules in the unit cell ($Z = 4$) and one molecule per asymmetric unit ($Z' = 1$). The corresponding XRD pattern is shown in Figure 4.3(b). This

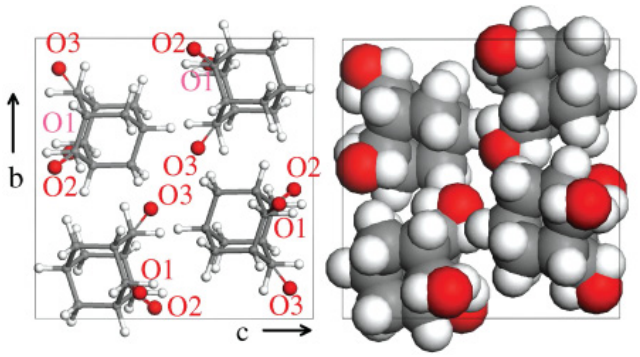

Figure 4.4: Left panel: Picture of the (h00) crystallographic phase of the monoclinic phase II with oxygen atoms (red) within their three occupational sites. Red labelled atoms correspond to the oxygen atoms within their three sites of fractional occupancies 0.25 (O1), 0.25 (O2), and 0.50 (O3). Right panel: The same projection with 70% of the van der Waals radii of the atoms.

phase actually displays an intrinsic statistical disorder concerning the position of the carbonyl oxygen, which can occupy one of three different sites. As can be seen in the left-hand panel of Figure 4.4 ((h00) crystallographic plane), the oxygen atom can occupy one of three possible sites, labelled O1, O2 and O3. The symmetry operations of the $P2_1/c$ space group are incompatible with an ordered structure with all the oxygens in the same site. Instead, such symmetry imposes a statistical occupancy of the oxygen sites. Rietveld refinement at different temperatures shows that the fractional occupancies are temperature-independent and are respectively equal to 25% (O1 and O2) and 50% (O3). This means then that for each unit lattice, the oxygen atom of the asymmetric unit formed by one molecule ($Z' = 1$) cannot be uniquely placed in one site but rather it is shared between three different sites with different probabilities of occupancy.

Chemical Formula		$C_{10}H_{14}O$	
M $[gmol^{-1}]$		150.2176	
Phase	FCC (I)	monoclinic (II)	orthorombic (III)
Space Group	$Fm\bar{3}m$	$P2_1/c$	$Cmc2_1$
a [Å]	9.4213 ± 0.0008	6.5920 ± 0.0017	6.8884 ± 0.0018
b [Å]	-	11.118 ± 0.003	10.830 ± 0.003
c [Å]	-	12.589 ± 0.003	10.658 ± 0.003
α[°]	90	90	90
β[°]	90	118.869 ± 0.011	90
γ[°]	90	90	90
V/Z [Å^3]	209.06	202.0 ± 0.1	198.8 ± 0.1
Z(Z′)	4(1)	4(1)	4(0.5)
T [K]	205	190	190

Table 4.1: Results of the structure for the FCC phase I, the metastable monoclinic phase II and the stable orthorhombic phase III.

We applied the same cycling procedure used in Ref. [16] to a sample placed inside the capillary tube used for XRD experiments. After about 10 cycles between 77 K and room temperature, the low-temperature monoclinic phase no longer appeared and a new diffraction pattern emerged (Figure 4.3 (c)). The Rietveld analysis was applied to determine the structure using a procedure similar to the monoclinic case, but combining it with minimization of the lattice energy. The best fit for the stable low-temperature phase III is an orthorhombic structure with space group $Cmc2_1$ and $Z = 4$.

The results on all three phases are summarized in Table 4.1.

Figure 4.5 shows a comparison between the structures of the stable orthorhombic phase III and the metastable monoclinic phase II (which

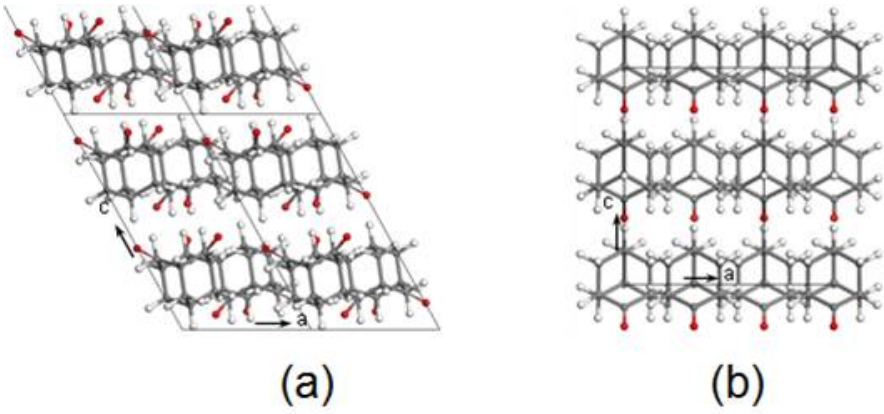

Figure 4.5: Structures of the (a) monoclinic phase II and (b) the orthorhombic phase III along the (0k0) plane.

are observed in roughly the same temperature range).

After the determination of the stable and metastable low-temperature structures, the temperature dependence of the lattice parameters was analysed to determine the thermal expansion parameters and volume change in the two low-temperature phases as well as in the FCC phase. The results are plotted in Figure 4.6.

The obtained lattice parameters and unit cell volume were fitted by assuming a polynomial dependence on temperature. The volume values at each temperature, depicted in Figure 4.7, were used to calculate the volume change at the monoclinic to FCC and orthorhombic to FCC transitions, which were found to be 6.54 and 3.86 cm^3/mol respectively. The last figure is identical to the volume change upon the pressure-induced transition determined in Ref. [19], which means that the low-temperature phase obtained by increasing the applied pressure must correspond to the stable orthorhombic phase.

To check the stability of the orthorhombic phase, high-pressure thermal analysis was performed. Figure 4.8 shows the experimental pressure-

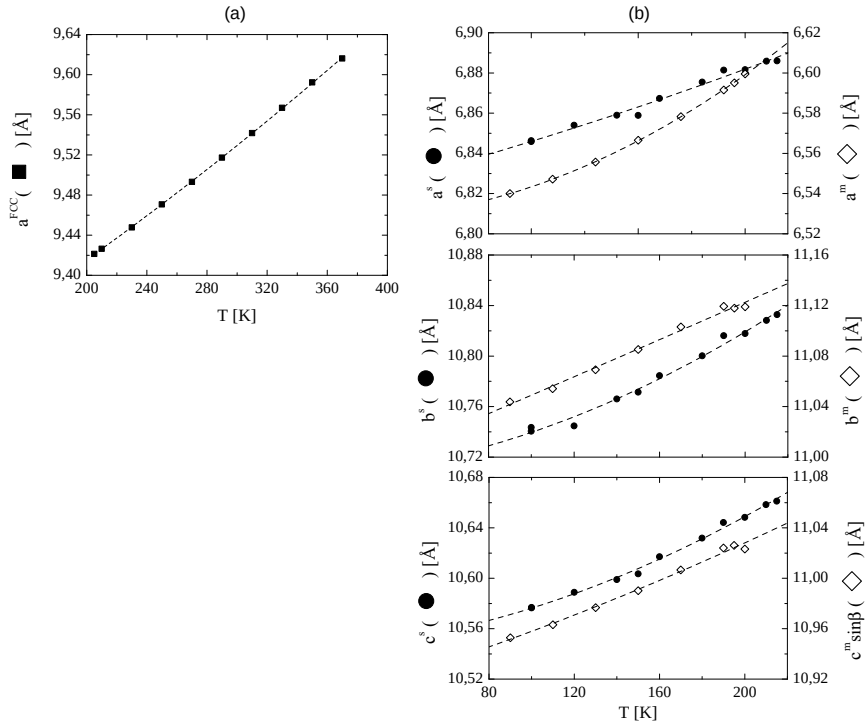

Figure 4.6: Lattice parameters of the 2A-O phases as a function of temperature. (a) FCC phase and (b) low-temperature phases: stable orthorhombic (left axes, filled symbols) and metastable monoclinic (right axes, empty symbols)

temperature diagram for both low-temperature to OD FCC phase transitions. The extrapolation to normal pressure gives a temperature of 217 K for the orthorhombic to FCC phase transition, which nicely agrees with the value obtained by adiabatic calorimetry [14] and that obtained by Butler *et al.* [16] after temperature cycling. Moreover, the high-pressure value of Hara *et al.* [19] perfectly matches the equilibrium line determined in this work between the orthorhombic and FCC phases. These results entail that the orthorhombic phase is the stable one. Another irrefutable experimental proof of the stabilization effect of pressure is obtained by compression and decompression of the monoclinic metastable phase at

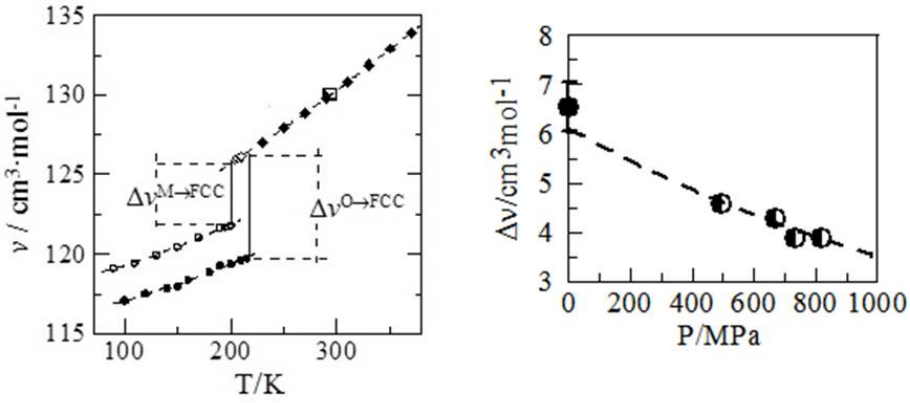

Figure 4.7: Left panel: molar volume for the stable orthorhombic (filled circles), the metastable monoclinic (empty circles) and the FCC phases of 2A-O as a function of temperature from X-ray measurements. Empty square represents the volume for the FCC phase from Ref. [20]. Right panel: volume variation as a function of pressure (half-filled circles) from Ref. [19] and the volume change at normal pressure (filled circle) from X-ray data for the orthorhombic-FCC transition[21].

temperatures lower than 200 K and heating up at normal pressure. Following this detour the temperature of the phase transition is found at 217 K, which again corresponds to the orthorhombic to FCC transition (and is instead far from our measured temperature of 203.6 K for the monoclinic to FCC transition).

4.4 The reorientational dynamics in the metastable monoclinic phase II

In this section and in the next one we focus on the metastable monoclinic phase II. The most striking feature of the structure of phase II is the existence of an intrinsic statistical disorder concerning the site occupancy

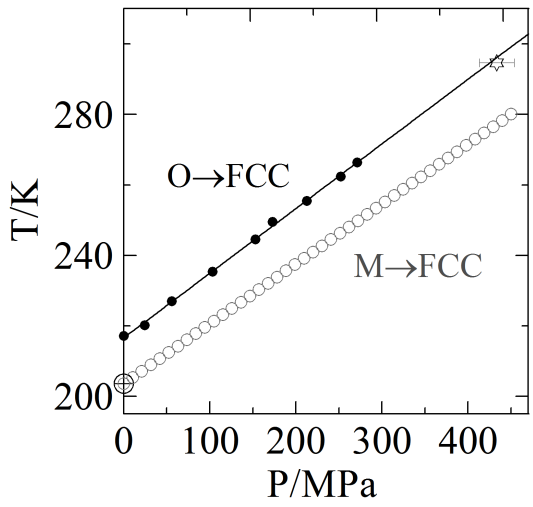

Figure 4.8: Experimental pressure-temperature diagram for low-temperature orthorhombic (O) to FCC phase transition (filled circle). Empty circle at normal pressure corresponds to the monoclinic (M) to FCC phase transition (the equilibrium line is shown in grey) calculated by means of Clausius-Clapeyron equation. The star at high-pressure corresponds to the value extrapolated from fig.2 in Ref. [19].

of the oxygen atom.

Diffraction techniques highlight the disorder and quantify unequivocally the possible molecular orientations within the commensurate long-range lattice, but they cannot provide information about the dynamics of the dipole reorientation. As already mentioned in section 4.1, the high-temperature phase I of 2O-A is an orientationally disordered FCC phase. The dynamic disorder is due to the reorientational motions of the dipolar axis (C_3) along the six fourfold $\langle 001 \rangle$ cubic lattice directions, while around the C=O axis of the molecules can display two positions related by a $\pi/2$-rotation [17]. Concerning the monoclinic phase II, NMR experiments concluded that "all the motions are completely frozen" [18].

Nevertheless, a published article focusing on the dynamics of OD phases [15] by dielectric spectroscopy stated that the I to II phase transition only involves a partial restriction of the reorientational motions, which is accompanied with a strong slow-down of the α-relaxation time. Because dielectric spectroscopy is sensitive to the dipole fluctuations (and "blind" to the $\pi/2$-rotations around the C=O axis), the observation of an α-relaxation implies the existence of a reorientational motion of the dipolar molecules, in strong contradiction to the NMR results. In addition, Brand et al. indicated the emergence in phase II of a shoulder in the high-frequency tail of the α-relaxation peak, possibly originated by a secondary β relaxation.

The existence of three distinct molecular orientations with the before mentioned fractional occupancies and the persistence of dipolar molecular dynamics, suggest that large-angle molecular rotations around a threefold axis occur in the low-temperature phase II. These rotations promote an effective time-average fluctuation of the molecular dipole which contributes to the dielectric susceptibility.

We performed broadband dielectric spectroscopy measurements on phase II in order to study the disorder in this "quasi-ordered" phase, and also on phase I to make sure that our results match the dielectric measurements reported in Ref. [15]. Figure 4.9 shows examples of the dielectric loss spectra of the phase II of 2A-O in a temperature range between 202 K and 88 K. The α-relaxation process is accompanied by a secondary β relaxation characterized by a much smaller strength ($\Delta\varepsilon_\alpha/\Delta\varepsilon_\beta \approx 500$). The dielectric loss spectra of the α relaxation could be fitted with a Havriliak-Negami line shape (Eq. 3.16) with typical parameters $0.55 < \alpha_{HN} < 0.89$ and $0.57 < \beta_{HN} < 0.71$, corresponding to a quite small stretching exponent $\beta_{KWW} = 0.50 - 0.57$ (as calculated

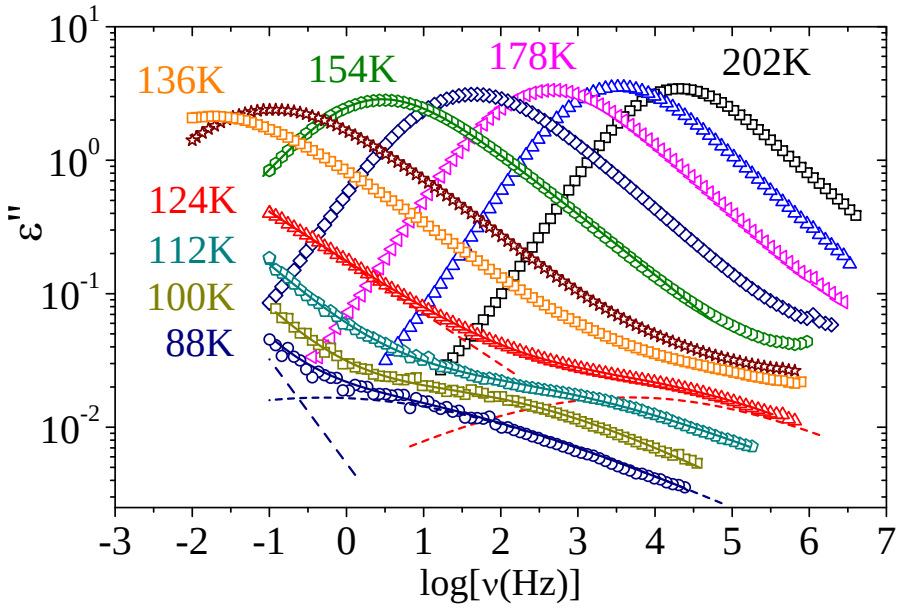

Figure 4.9: Dielectric loss spectra of phase II of 2A-O for several temperatures. The solid lines are examples of the fits using Havriliak-Negami and Cole-Cole functions for the α and β processes, respectively.

using the Alvarez-Alegria-Colmenero equation eq. 3.21). The β relaxation appearing at low temperature and high frequency was instead modelled with a Cole-Cole function (Eq. 3.9) with a resulting parameter $0.45 < \alpha_{CC} < 0.57$. In the case of phase I, only the α relaxation is visible and the spectra can be fitted with an Cole-Davidson line shape (Eq. 3.12) with fitting parameter $0.83 < \beta_{CD} < 0.87$ corresponding to a stretching exponent $\beta_{KWW} = 0.86 - 0.89$.

The values of β_{KWW} and of the Kirkwood factor g_K as calculated from the experimental data are shown in panels (a) and (b) of Figure 4.10, respectively.

It is worth noting that the typical value of the β_{KWW} parameter of the α relaxation in the FCC phase I is about 0.9, which is close to one

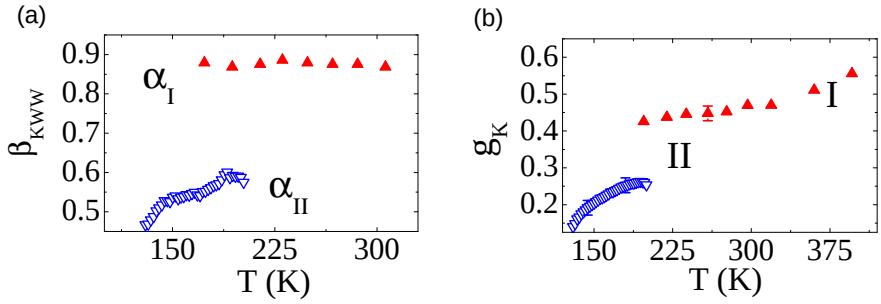

Figure 4.10: Values of β_{KWW} (a) and of Kirkwood factor g_K (b) of phases I and II as a function of temperature.

(Figure 4.10(a)). On the contrary, β_{KWW} is quite small in the phase II (< 0.6), which is an indication that strong orientational correlations exist between nearest neighbours and implies that the α relaxation in phase II has a markedly cooperative character. Such a conclusion is supported also by the low value of the Kirkwood factor $g_K = \mu^2/\mu_{gas}^2$, which is lower than 0.3 (Figure 4.10(b)). In the expression for g_K, μ_{gas} is the estimated dipole moment in gas phase (equal to 3.4D) and μ^2 has been extrapolated from Eq. 2.19 (see section 2.1), resulting in the following relation:

$$\mu^2 = 9\varepsilon_0 k_B T \frac{V}{Z} \frac{(\varepsilon_s - \varepsilon_\infty)(2\varepsilon_s + \varepsilon_\infty)}{\varepsilon_s(\varepsilon_\infty + 2)^2} \tag{4.1}$$

Here ε_0 is the vacuum permittivity, ε_S and ε_∞ are the static and relaxed permittivity obtained from the dielectric spectra, and the parameter V/Z is the molecular volume as obtained from X-ray diffraction, which takes values between 198 $\mathring{A}^3/molecule$ and 202 $\mathring{A}^3/molecule$ in the temperature range between 90 K and 200 K (Figure 4.11).

The value of the g_K factor should be taken cautiously because it has been derived assuming spatial isotropy. Such an assumption can be justified for liquids or translationally ordered cubic phases, but it is

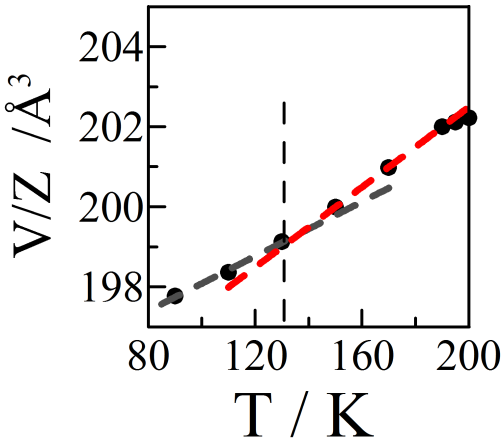

Figure 4.11: Cell volume versus temperature in the phase II. Dashed and dotted lines are linear regression to data above and below T_g. Vertical dashed line shows $T_g = 130$ K

only a rough approximation for anisotropic media such as the monoclinic phase II. Nevertheless, it still provides a valid figure of merit to discuss the changes with temperature and thus allow the comparison with the isotropic FCC phase I.

The cooperativity of the relaxation in the monoclinic phase II is evident also if one considers the structural arrangement of the molecules and their associated van der Waals radii (see the right panel of Figure 4.4). It is clear that there is not enough space for the molecules to jump from one orientational site to another without intermolecular cooperation and correlated motions of adjacent molecules. Moreover, since the fractional occupancies of the three sites have been shown to be constant in temperature, this means that a sort of local symmetry is preserved and thus that orientational correlations among molecules exist (as confirmed by the low values of g_K and β_{KWW}). This implies that dynamic reorientational

processes must simultaneously involve several molecules, and be correlated in such a way as to preserve the local symmetry.

The relaxation times as a function of reciprocal temperature (Arrhenius plot) are shown in Figure 4.12 for both phase I and phase II. Figure 4.12 collects the relaxation time for all processes (including the β relaxation in phase II), as well as previously published results on the relaxation times in phase I obtained with different techniques [12, 13, 15, 17, 18].

The relaxation times for all dynamic processes follow an Arrhenius (simply-activated) temperature behaviour. The activation energy ($E_a/k_B = a1000/\log e$, where a is the slope of the linear fit to the Arrhenius plot) for the α process in phase II is higher [$E(\alpha_{II})/k_B = 5746 \pm 17$ K] than that in the phase I [$E(\alpha_I)/k_B = 1699 \pm 10$ K], which again indicates stronger intermolecular interactions in the former phase. The increased intermolecular coupling cannot be due only to the volume change at the transition, which is rather small ($\Delta V_{II\to I}/V_I \approx 3\%$). The large variation in the activation energy is accompanied by a corresponding change in the value of the Arrhenius prefactor (defined as the value of the relaxation time at $1000/T \to 0$), which is $\tau_\infty(\alpha_I) = 1.25 \times 10^{-13}$ s in phase I, while it is equal to $\tau_\infty(\alpha_{II}) = 6.45 \times 10^{-18}$ s in phase II. These values agree with previously published ones [15].

From the Arrhenius plot it can be seen that the α-relaxation time for phase II reaches 10^2 s (the conventional relaxation time for glass transition) at $T_g = 130$ K. As visible in Figure 4.11, at this temperature a change of slope is observed in the plot of the cell volume versus temperature, which is another indication of glassy-like behaviour.

The relaxation time of the β process (see Figure 4.12) also follows an Arrhenius behaviour, with $E(\beta_{II})/k_B = 2744 \pm 1$ K and $\tau_\infty(\beta_{II}) = 6.53 \times 10^{-15}$ s. The origin of the β relaxation cannot be attributed to

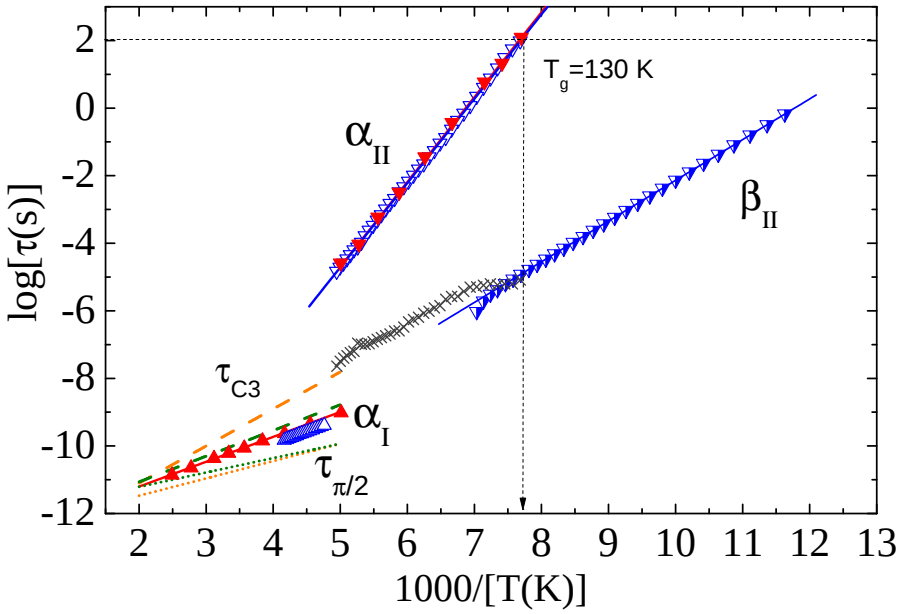

Figure 4.12: Relaxation times as a function of reciprocal temperature for the different relaxation processes in the FCC phase I and in the monoclinic phase II. Phase I: Dashed lines show the characteristic time τ_{C3} of $2\pi/3$-rotations of the C=O dipolar axis between the [001] cubic lattice directions; dotted lines show the time $\tau_{\pi/2}$ of $\pi/2$ jump rotations of the molecules around the C=O axis; data are from NMR (Ref. [18]) (green) and from IQNS (Ref. [17]) (orange); α_I process (equivalent to rotations of the C=O dipolar axis) from dielectric spectroscopy from Ref. [15] (red solid up triangles) and from this thesis work (blue open up triangles). Phase II: α-relaxation times are represented by open and closed down triangles, respectively, from this thesis work and Ref. [15] (blue and red symbols, respectively), while β-relaxation times are shown as blue-white down triangles. Lines are linear regressions to data. Grey asterisks are the predicted β-relaxation times calculated according to the coupling model (see text).

the existence of different independent molecules in the unit cell (since $Z' = 1$). Moreover, the rigid character of the carbonyl C=O group covalently attached to the adamantane skeleton rules out the possibility of intramolecular dipole fluctuations [15, 22–24] as the origin of the secondary relaxation. Given therefore that the β relaxation is related to some intermolecular relaxation process, and that only one kind of molecule is present in the asymmetric unit cell, it should be instead associated with the α relaxation of the same phase. In other words, the β relaxation corresponds to a Johari-Goldstein (JG) process associated, just like the corresponding α relaxation, to dipole fluctuations due to the oxygen site disorder.

A theoretical model that can explain the correlation between α and JG β relaxation is the Coupling model (CM) [25, 26]. According to such model, the β process is the primitive motion which initiates the cooperative α process at particular sites in the disordered structure. The more cooperative the α process, the greater the time-scale separation between such process and the JG β process. We already saw that the cooperativity of the primary process is reflected by a broader distribution of relaxation times, i.e., by a small value of β_{KWW}. In section 2.3.2 we saw that the CM predicts a quantitative relation, due to many-molecule dynamics, between the primitive JG relaxation time (τ_0 or τ_{JG}) and τ_α:

$$\tau_{JG} \sim \tau_0 = \tau_\alpha^{\beta_{KWW}} t_C^{1-\beta_{KWW}} \tag{4.2}$$

Here t_C is the crossover time at which the many-body dynamics starts to occur, equal to 2 ps in molecular glass formers. In the case of 2A-O, the calculated primitive τ_{JG} matches exactly the relaxation time for the β process (grey asterisks in Figure 4.12) within the temperature range for which available β_{KWW} data for the α process exist. The fact that the

α_{II} process is accompanied by a JG relaxation is further proof of the cooperativity of the α-relaxation process. Moreover, Eq. 4.2 predicts that the ratio between the activation energy of α and JG β processes should be equal to β_{KWW}, as in our case.

As a final remark, it is interesting to note that the extrapolation of the behaviour of the β process of phase II to high temperature gives a decent overlap with the α relaxation in phase I (see Figure 4.12). The latter is associated with reorientational motions with a very small degree of cooperativity. Such agreement is noteworthy, as it suggests that the statistical disorder associated with the fractional occupancy of the oxygen sites in phase II might give rise in phase I to a clear primary relaxation with considerable dielectric strength (see Figure 4.9).

4.5 Inelastic neutron scattering results and Density Functional Theory analysis

In order to check the fractional occupancies of the oxygen atom and confirm the existence of structural dynamics in phase II, an inelastic neutron scattering experiment was performed to study the lattice and molecular excitations in 2A-O in the form of phonon density of states (PDOS). The scattering data were acquired at the IN1 line of the ILL reactor in Grenoble, France, using a neutron spectrometer with a Be filter. The result of the inelastic scans between 0 and 220 meV, measured at three different temperatures are shown in Figure 4.13. The experimental results have been corrected applying empty cell subtraction, monitor normalization and energy subtraction (3.5 meV). In order to analyse the data, a Density Functional Theory (DFT) calculation was performed together with a spectral simulation. The quantum chemical simulation

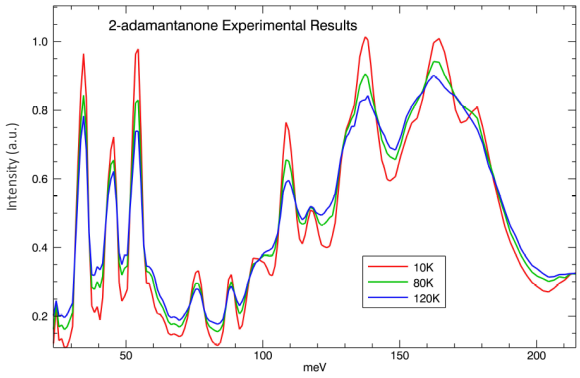

Figure 4.13: Experimental inelastic neutron scattering results obtained on 2A-O at 10 K, 80 K and 120 K. Corrections applied.

was carried out applying Double Numerical plus Polarization (DNP) basis set with the Perdew-Burke-Ernzerhof (PBE) functional. This is found to yield a better agreement in the high frequency region as compared with the Becke-Lee-Young-Parr (BLYP) method used in Ref. [27].

The results of the convolution taking into account the fractional occupancies of 25% for O1, 25% for O2 and 50% for O3 are plotted in Figure 4.14. In the plot at 10 K, the peaks associated with the oxygen modes are indicated. The measured and simulated frequency positions of the peaks are compared in Table 4.2.

Introducing a Debye-Wall factor in the simulated spectra it is possible to obtain a better agreement with the measured results and better estimation of the peak intensities. The simulated spectra considering the Debye-Waller correction are plotted in Figure 4.15 together with the experimental data.

Comparing with the results of Ref. [27], it is found that using the PBE functional the agreement between the simulated spectra and the

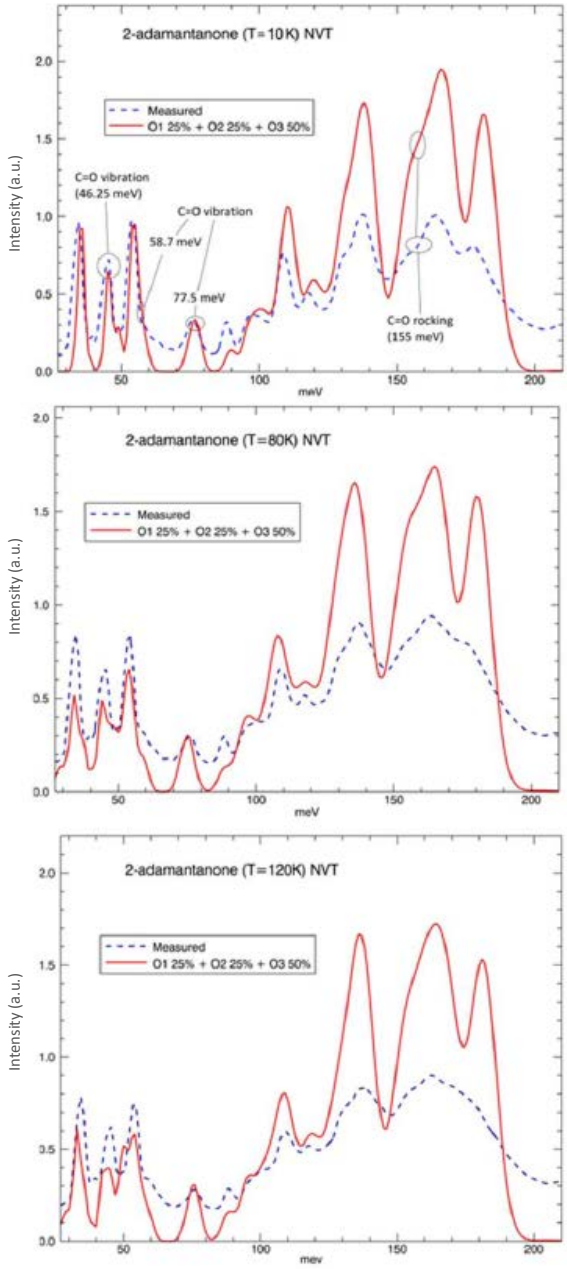

Figure 4.14: Measured (dashed blue line) and simulated (red line) spectra. In the simulation the fractional occupancies of 25% (O1 and O2) and 50% (O3) for the oxygen atom have been applied at temperatures of 10 K, 80 K and 120 K.

Sym	ν_i	Observed (cm^{-1}/meV)	PBE (cm^{-1}/meV)	PED	$BLYP^a$ (cm^{-1}/meV)	PED^a
A_1	1	776/97	781/98	CC stretch	764/95	CC stretch
	2	715/89	720/90	CC stretch, CCC def	701/87	CC stretch, CCC def
	3	435/54	432/54	CCC def, CH_2 rock	432/54	CCC def, CH_2 rock
	4	370/46	368/46	C=O sym def, CCC def	367/46	C=O sym def, CCC def
B_1	5	1440/180	1500/188	CH bend, CH_2 scissor	1443/179	CH_2 scissor
	6	1315/164	1320/165	CH bend, CH_2 rock	1320/164	CH bend, CH_2 wag, CH_2 rock
	7	944/118	961/120	CC stretch, CH_2 rock	943/117	CC stretch, CH_2 rock, CCC def
	8	620/78	618/77	C=O vibration, CC stretch	619/77	CCC def, CC stretch, C=O wag
B_2	9	1240/155	1230/154	CH_2 stretch, C=O rock	1224/152	CH bend, CC stretch, C=O rock
	10	1096/137	1094/137	CH_2 rock, CH bend	1086/135	CH_2 rock, CH bend, CH_2 wag, CCC def
	11	864/108	867/108	CH_2 rock	863/107	CH_2 rock, CC stretch
	12	470/59	468/59	C=O vibration, CC stretch	465/58	C=O rock, CCC def, CC stretch
	13	273/34	274/34	CCC def	275/34	CCC def

Table 4.2: Observed and simulated (PBE) vibrational frequencies of 2A-O.

[a] Simulated values with the Becke-Lee-Young-Parr (BLYP) method and vibrational assignment using PED functional as in Ref. [27].

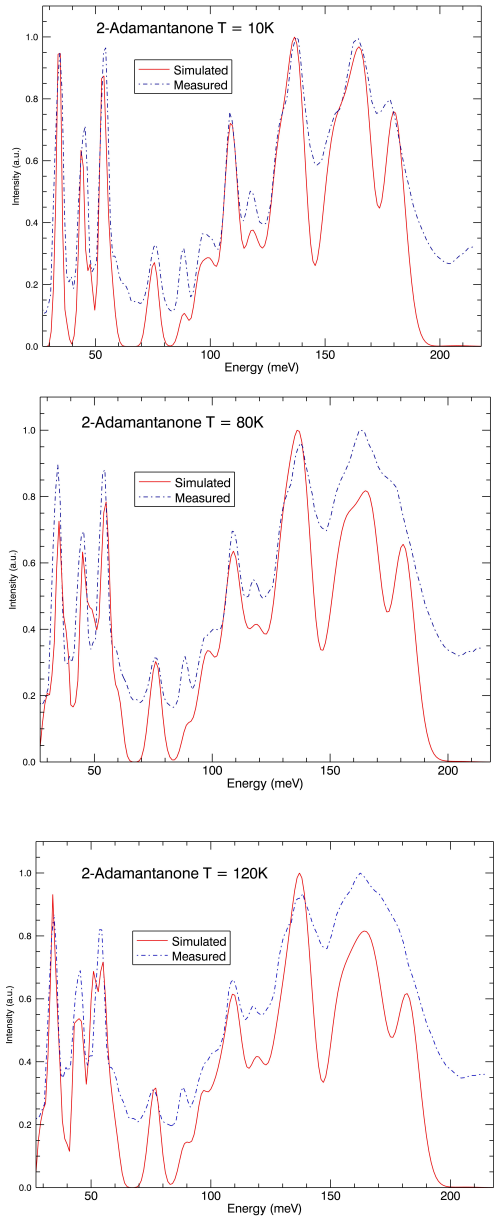

Figure 4.15: Measured (dashed blue line) and simulated (red line) spectra. In the simulation the fractional occupancies of 25% (O1 and O2) and 50% (O3) for the oxygen atom have been applied at temperatures of 10 K, 80 K and 120 K together with the Debye-Waller factor corrections.

experimental data is improved, although there are still some discrepancies in the $1500 - 1400 cm^{-1}$ range. In this range there is a overestimation of the spectral intensity compared to experimental data. Despite these discrepancies, however, it is found that the experimental data are accurately modelled by taking into account the three oxygen atom configurations with weights of 25% (O1 and O2) and 50% (O3). Modifying these weights leads to lower agreement. Therefore, any dynamic process (such as the α relaxation) involving the reorientation of the molecules must be a collective motion that respects the overall, fixed fractional occupancies of oxygen sites, thereby confirming the cooperative nature of the relaxation process in the orientationally-ordered phase II.

4.6 Conclusions

The lattice structures of two low-temperature phases of 2-adamantanone are probed by temperature-dependent X-ray diffraction, thereby establishing the thermal evolution of the lattice parameters and of the cell volume, as well as the thermodynamic stability of each phase. The orientationally-ordered, metastable low-temperature phase II displays an intrinsic statistical disorder concerning the site occupancy of the carbonyl moiety of the molecule. Dielectric studies evidence the existence of an α relaxation, originating from strongly correlated large-angle dipole fluctuations of groups of molecules, and of a corresponding primitive (Johari-Goldstein) β relaxation.

The coupling model is able to account for the existence of such Johari-Goldstein β relaxation and of the low value of the stretching β_{KWW} parameter (corresponding to a high coupling parameter $1 - \beta_{KWW}$), in spite of the strong (Arrhenius) character of the α-relaxation process.

The emergence of a glassy-like $\alpha - \beta$ dynamics even in an "ordered" system where coupling exists between motions on different time and length scales is a surprising result and opens the way to further studies of non-conventional cooperative relaxation dynamics.

The statistical disorder has been proven by means of DFT simulations of the inelastic neutron scattering data. Three non-equivalent crystallographic positions of the carbonyl oxygen atom of the molecule must be taken into account to reproduce the experimental spectra. This confirm the existence of a statistical disorder and the cooperative nature of the relaxation process in the OO phase II.

Bibliography

[1] G. C. McIntosh, M. Yoon, S. Berber, and D. Tománek *Phys. Rev. B*, vol. 70, p. 045401, 2004.

[2] Y. Y. Wang, E. Kioupakis, X. H. Lu, D. Wegner, R. Yamachika, J. E. Dahl, R. M. K. Carlson, S. G. Louie, and M. F. Crommie *Nature Mater.*, vol. 7, p. 38, 2008.

[3] J. E. Dahl, S. G. Liu, and R. M. K. Carlson *Science*, vol. 299, p. 96, 2003.

[4] W. L. Yang, J. D. Fabbri, T. M. Willey, J. R. I. Lee, J. E. Dahl, R. M. K. Carlson, P. R. Schreiner, A. A. Fokin, B. A. Tkachenko, N. A. Fokina, W. Meevasana, N. Mannella, K. Tanaka, X. J. Zhou, T. van Buuren, M. A. Kelly, Z. Hussain, N. A. Melosh, and Z.-X. Shen *Science*, vol. 316, p. 1460, 2007.

[5] Q.-S. Du and R.-B. Huang *Current Protein and Peptide Science*, vol. 13, p. 205, 2012.

[6] W. Guo, E. Galoppini, R. Gilardi, G. I. Rydja, and Y. H. Chen *Cryst. Growth & Design*, vol. 1, p. 231, 2001.

[7] V. Vijayakumar, A. B. Garg, B. K. Godwal, and S. K. Sikka *Chem. Phys. Lett.*, vol. 330, p. 275, 2000.

[8] N. A. Murugan and S. J. Yashonath *J. Phys. Chem. B*, vol. 109, p. 2014, 2005.

[9] L. C. Pardo, J. L. Tamarit, N. Veglio, F. J. Bermejo, and G. J. Cuello *J. Phys. Rev. B*, vol. 76, p. 134203, 2007.

[10] J. Timmermans *J. Phys. Chem. Solids*, vol. 18, p. 1, 1961.

[11] J. Salud, D. López, M. Barrio, J. L. Tamarit, H. A. J. Oonk, P. Negrier, and Y. Haget *J. Solid State Chem.*, vol. 133, p. 536, 1997.

[12] J. P. Amoreux, M. Sahour, C. Fernandez, and P. Bodart *Phys. Status Solidi*, vol. 143, p. 441, 1994.

[13] J. P. Amoureux, M. Castelain, M. Bee, B. Arnaud, and M. L. Shouteeten *J. Phys. C: Solid State Phys.*, vol. 15, p. 1319, 1982.

[14] A. B. Bazyleva, A. V. Blokhin, G. J. Kabo, A. G. Kabo, and V. M. Sevruk *Thermochim. Acta*, vol. 451, p. 65, 2006.

[15] R. Brand, P. Lunkenheimer, and A. Loidl *J. Chem. Phys.*, vol. 116, p. 10386, 2002.

[16] I. S. Butler, H. B. R. Cole, D. F. R. Gilson, P. D. Harvey, and J. D. McFarlane *J. Chem. Soc. Faraday Trans. II*, vol. 82, p. 535, 1986.

[17] M. Bee and J. P. Amoreux *Mol. Phys.*, vol. 47, p. 533, 1982.

[18] R. Decressain, J. P. Amoreux, and E. Cochon *Phys. Status Solidi*, vol. 190, p. 295, 1995.

[19] K. Hara, Y. Katou, and J. Osugi *Bull. Chem. Soc. Jpn.*, vol. 54, p. 687, 1981.

[20] J. P. Amoureux and M. Bee *J. Phys. C: Solid St. Phys.*, vol. 13, p. 3577, 1980.

[21] P. Negrier, M. Barrio, M. Romanini, J. L. Tamarit, D. Mondieig, A. Krivchikov, L. Kepinski, A. Jezowski, and D. Szewczyk *Crystal Growth and Design*, vol. 14, p. 2626, 2014.

[22] P. D. Harvey, I. S. Butler, D. F. R. Gilson, and P. T. T. Wong *J. Phys. Chem.*, vol. 90, p. 4546, 1986.

[23] L. Bistricic, G. Baranovic, and K. Mlinaric-Majerski *Spectr. Acta A*, vol. 54, p. 1961, 1998.

[24] L. Bistricic, G. Baranovic, and V.Volovsek *J. Mol. Struct.*, vol. 482-483, p. 661, 1999.

[25] K. L. Ngai *Phys. Rev. E*, vol. 57, p. 7346, 1998.

[26] K. L. Ngai *J. Phys. Condens. Matter*, vol. 15, p. S1107, 2003.

[27] L. Bistricic, L. Pejov, and G. Baranovic *J. Mol. Structure (Teochem)*, vol. 594, p. 79, 2002.

Chapter 5

SCALING OF THE ORIENTATIONAL DYNAMICS IN PLASTIC MIXED CRYSTALS BY THE DYNAMICAL SCALING MODEL

5.1 Introduction

Organic compounds formed by globular or pseudoglobular molecules displaying isotropic or only weakly angle-dependent interactions are able to form orientationally disordered phases (OD, plastic phases) below their melting temperature. In such OD phase the centres of mass of the molecules occupy lattice points as in a crystal and usually exhibit high

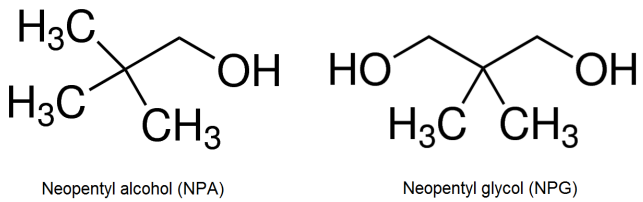

Figure 5.1: Molecular structure of $(CH_3)_3CCH_2OH$ (Neopentyl alcohol, NPA) and $(CH_3)_2C(CH_2OH)_2$ (Neopenthylglycol, NPG).

translational symmetry, but the molecular orientations are disordered as in a liquid. If the temperature is lowered while the system is in the OD phase, then the reorienting molecules can freeze into a random configuration forming an orientational glass (OG) [1]. The resulting glassy state entails only the arrest of the orientational degrees of freedom and is a priory substantially different from the structural glasses in which both the translational and orientational degrees of freedom are frozen. Nevertheless, it has been shown that the dynamics of OD phases share many common features with liquid glass former and that, in fact, the orientational degrees of freedom determine to a large extent the properties of structural glasses, as shown in comparative studies on the glass and glassy transitions in ethanol [2]. In this chapter we discuss the OG glass transition in the orientationally disordered mixed crystals formed between $(CH_3)_3CCH_2OH$ (Neopentyl alcohol, NPA) and $(CH_3)_2C(CH_2OH)_2$ (Neopenthyl glycol, NPG) (Figure 5.1). In particular we have studied the compositional range of the NPA_{1-x} NPG_x compressed into $0 < x < 0.5$, for which OG glasses are known to form.

5.2 Experimental methods

NPA and NPG with a purity of 99% where purchased from Aldrich Chemical Company. The mixed samples were prepared by melting and mixing the appropriate amounts of the two compounds. The prepared samples were located while in the liquid form into a parallel-plate stainless steel capacitor with the electrodes separated by $50\mu m$-thick silica spacers. The frequency and temperature dependence of the complex dielectric permittivity was measured by broadband dielectric spectroscopy (see section 3.2.1). The measurements were performed in the frequency range from 10^{-2} to 10^{6} Hz with a Novocontrol Alpha Analyser spectrometer equipped with a Quatro temperature controller using a nitrogen-gas cryostat. The temperature interval of the measurements is between 127 K and 273 K with a temperature stability at the sample around 0.1 K.

5.3 The pure compounds

The orientationally ordered (OO) triclinic low-temperature phase II of NPA $[(CH_3)_3CCH_2OH]$ [3] transforms into a orientationally disordered (OD) face centred cubic (FCC) phase I at 235.4 K which is then stable up to 329.8 K [4], temperature at which melting takes place (see Figure 5.2). When the OD phase I of NPA is cooled down rapidly enough, the transition to the crystalline phase II does not take place: the disordered system is then supercooled and a glassy state (OG) forms, phase I'. Upon increasing the temperature from the glassy state, the transition to the supercooled phase I' takes place at around 134.7 K [5]. At higher temperature the phase I' can crystallize into the stable phase II.

The supercooled phase I' is quite difficult to reach and maintain because of the facility of crystallization of NPA. As it was shown also

for some structural glasses [6, 7], the use of an impurity can suppress the crystallization. In this case a chemically and structurally similar molecule, named NPG [$(CH_3)_2C(CH_2OH)_2$], is employed to partially replace the NPA molecules without resulting in a different lattice symmetry. A continuous series of face-centred cubic mixed crystals with different stoichiometries are obtained.

NPG is characterized by a low-temperature monoclinic ordered phase that transforms into an orientationally disordered FCC phase at 314.4 K and this phase is stable up to 402.8 K [4]. The disordered phase can be supercooled and the transition to the glassy state takes place at around 205.7 K (see Figure 5.2) [5].

The phase diagram of the $NPA_{1-x}NPG_x$ mixed crystals is reported in Figure 5.2. The glass transition temperatures for this system were obtained by means of X-ray diffraction and specific heat measurements. The glass transition for the pure compounds have been determined by dielectric spectroscopy in Ref. [5]. It can be seen that there is a critical concentration ($x_c \approx 0.5$) above which the mixed crystals do not display a glassy transition but instead probably solidify into a phase with static orientational order.

5.4 Analysis of the glassy dynamics

In previous work [8] the relaxation times of the $NPA_{0.7}NPG_{0.3}$ mixed crystal was measured. The temperature dependence of the relaxation time was fitted according to the CG four-parameter equation (Eq. 1.7) due to the extremely wide frequency and temperature ranges of the measurements. Nevertheless, it was found that neither a CG model nor the VFT three-parameter equation (Eq. 1.3) are able to reproduce satisfactory

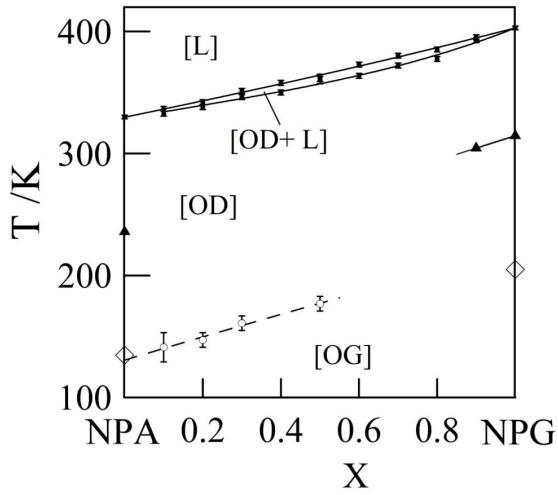

Figure 5.2: $NPA_{1-x}NPG_x$ equilibrium phase diagram. Filled circles corresponds to the two phase OD + Liquid (L) equilibrium temperatures; filled triangles corresponds to the low-temperature ordered phase II to OD phase I transition. Non-equilibrium glass transition temperature T_g as a function of molar fraction obtained by calorimetry [8] are also showed (empty circles). The empty diamonds correspond to the T_g extrapolated from the fits of the relaxation time of the pure NPA [8] and NPG [5] compounds.

all results [9]. By applying a linearised derivative analysis the existence of a crossover in the relaxation times was demonstrated [10, 11]. Here we focus on the application of the theoretical predictions of the Dynamic Scaling Model (DSM) (see section 1.2.1) for the mixed crystals $NPA_{1-x}NPG_x$, with $0 < x \leq 0.5$, in order to investigate the possible existence of a crossover similar to the one reported for $NPA_{0.7}NPG_{0.3}$.

Figure 5.3 displays the dielectric loss spectra of the $NPA_{0.6}NPG_{0.4}$ OD mixed crystal acquired at various temperatures upon cooling from room temperature. Similar results are obtained for all the concentrations under investigation. From a first inspection of Figure 5.3 we can observe

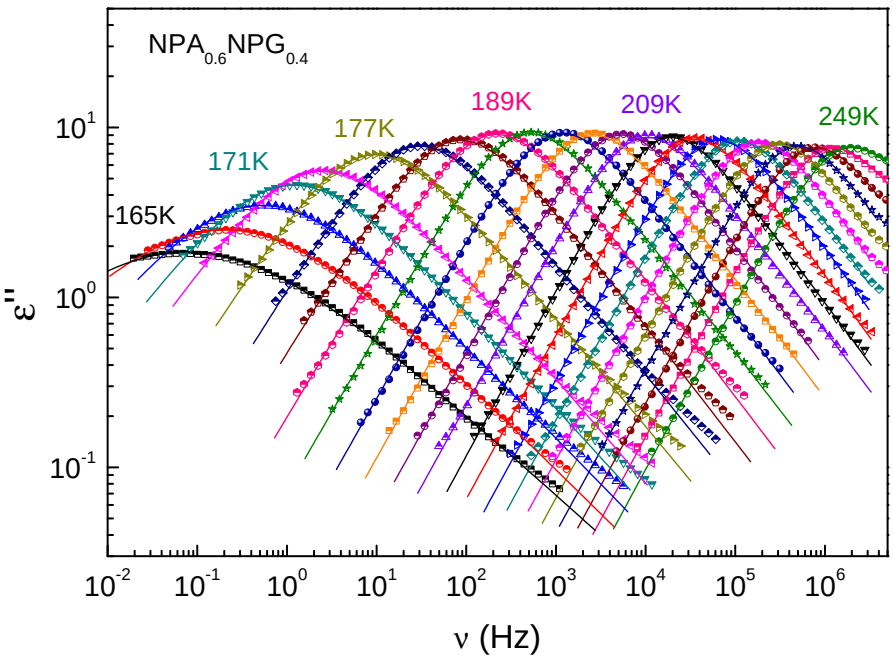

Figure 5.3: Relaxation dielectric loss curves for $NPA_{0.60}NPG_{0.40}$ mixed crystal in the OD FCC phase from 249 to 173 K every 4 K and from 171 to 165 K every 2 K after the subtraction of the electrical conductivity. Solid lines correspond to the fits using the HN function.

that the width of the α-relaxation peak clearly exceeds the width of a simple Debye relaxation process. Moreover, the width as well as the asymmetry of the peak increase with decreasing temperature. The dielectric spectra were fitted assuming for the α peak an empirical Havriliak-Negami equation (Eq. 3.16). The resulting relaxation times are plotted in Figure 5.4 as function of the reciprocal temperature are plotted for all the stoichiometries under scrutiny.

The Arrhenius plots of the relaxation time were fitted by using both the CG and the VFT models. We can see that in most cases neither the CG nor the VFT model are able to reproduce all the experimental points.

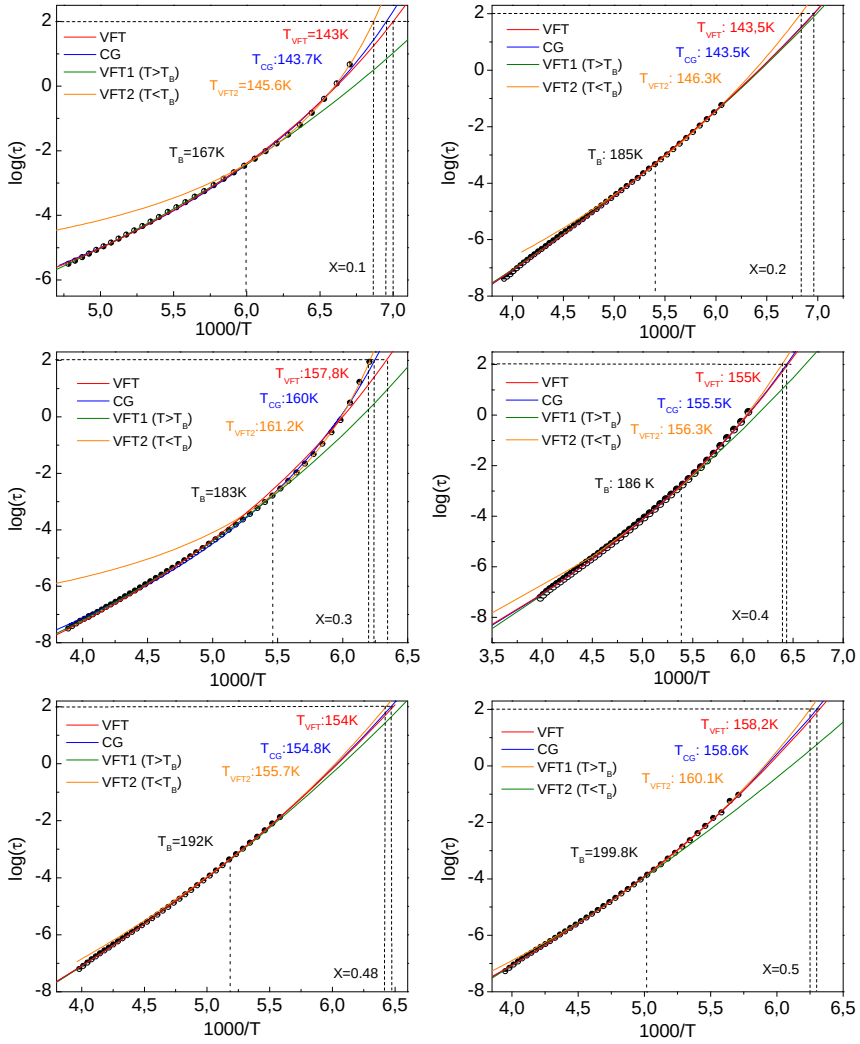

Figure 5.4: Relaxation times as a function of reciprocal temperature for different mole fraction x of the $NPA_{1-x}NPG_x$ mixed crystal. Solid lines represents fits with the CG equation (blue line) and the VFT equations (red line). Dashed lines indicates the glass temperatures according to the different fits. The vertical straight lines correspond to the crossover temperature T_B. The orange and green solid lines represents the VFT equation applied to the two temperature ranges below and above the crossover temperature.

.

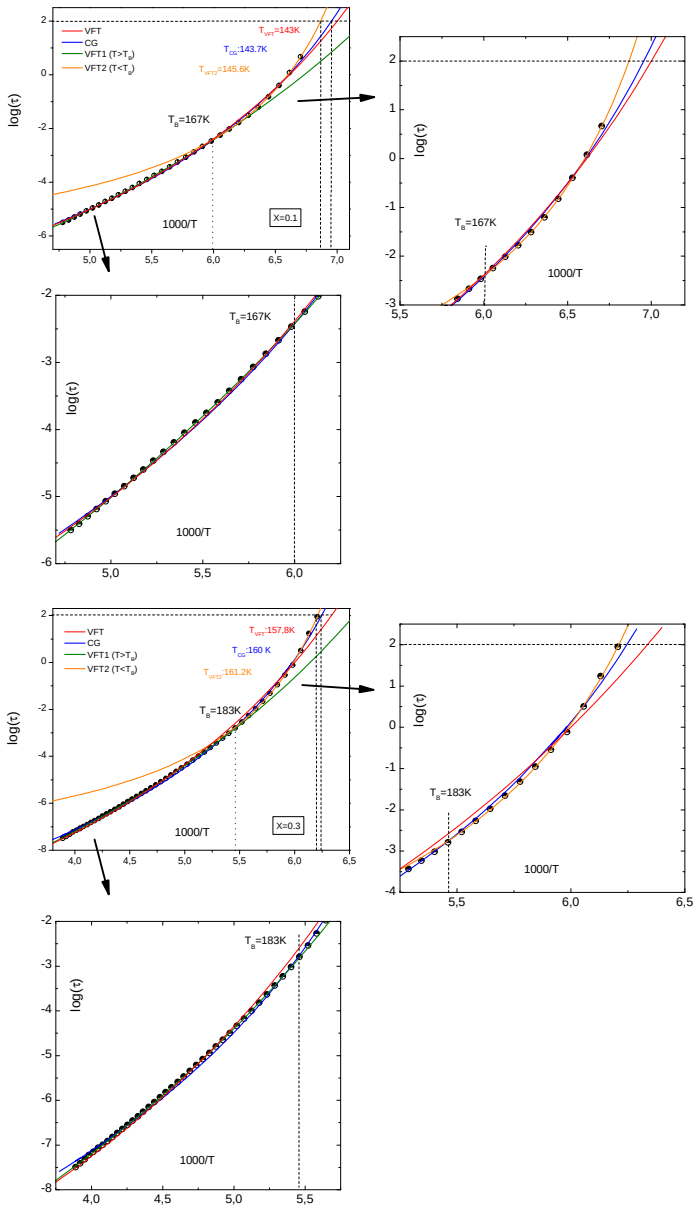

Figure 5.5: Relaxation times as a function of the reciprocal temperature for the two mole fraction x equal to 0.1 and 0.3 of the $NPA_{1-x}NPGx$ mixed crystals. In the insets are represented the low- and high-frequency regions of the relaxation times in order to better see the disagreement between the CG (blue line) and the VFT (red line) fits with the experimental data.

Figure 5.5 displays the Arrhenius plot for two concentrations, with a zoom on the high- and low-frequency regions to better highlight the disagreement between the experimental data and the CG and VFT models. Figure 5.6 exhibits the result of the derivative-based analysis using equation 1.6. In this representation it is possible to directly visualize the existence of two temperature domains with distinct activation energy, confirming that a single VFT regime cannot account for all the experimental points.

Instead, two VFT regimes are needed, above and below a crossover temperature T_B (see Figure 5.4). Such crossover temperature separates the temperature ranges described by two distinct VFT equations (Table 5.1 summarizes the VFT fitting parameters below T_B). In order to check the validity of the critical-like behaviour predicted by the DSM theory (Eq. 1.10), a derivative-based analysis is applied based on the following equation:

$$\frac{H_a(T)}{R} = R\left(\frac{dln\tau}{d(1/T)}\right) = \frac{\gamma T^2}{T - T_C} \tag{5.1}$$

Here T_C is the critical temperature at which the DSM equation diverges (see eq. 1.10). From eq. 5.1 one obtains:

$$\frac{RT^2}{H_a} = \left(\frac{1}{\gamma}\right)T - \left(\frac{T_C}{\gamma}\right) = BT - A. \tag{5.2}$$

In Figure 5.7 the quantity RT^2/H_a is plotted versus the temperature T. The observed linear dependence, which agrees with Eq. 5.2, reveals that the description based on the critical-like DSM behaviour is more accurate than a VFT parametrization, and corroborates the validity of the DSM in the temperature range $T_g \leq T \leq T_g + 80$, that is in the all experimental range, for these OD mixed crystals. The critical-like behaviour is described by an exponent $\gamma = \nu z \approx 10 \pm 1$ that is very close to the universal value

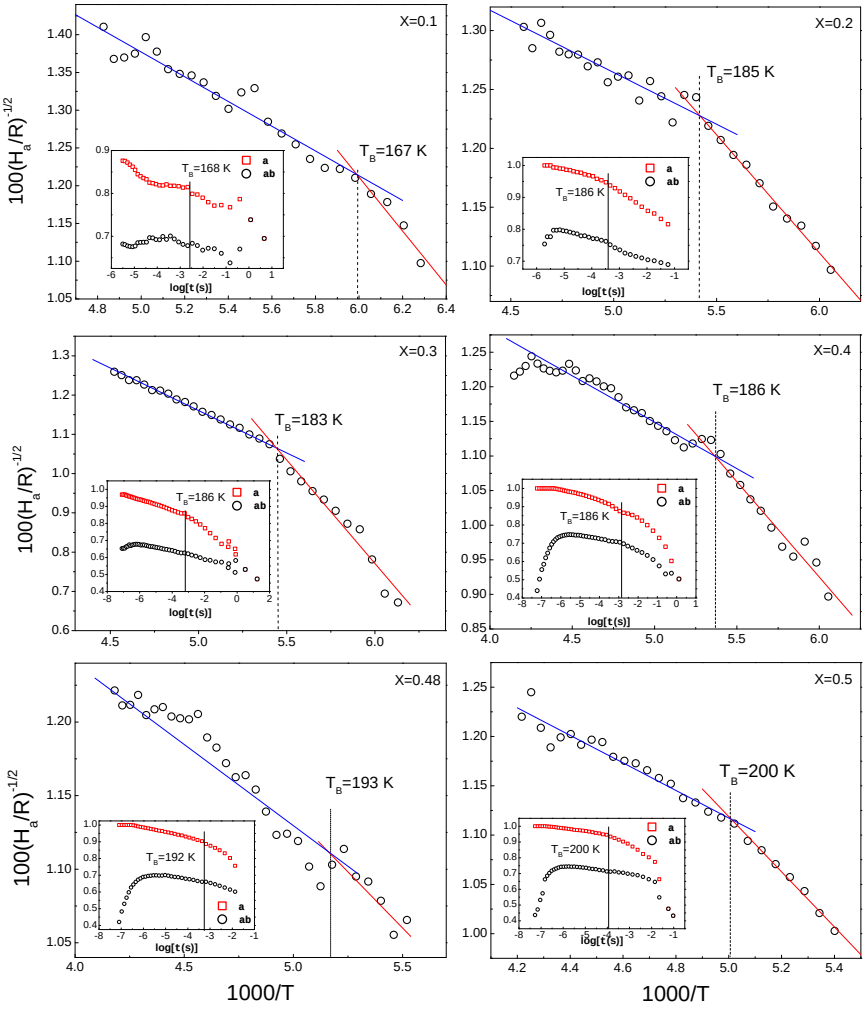

Figure 5.6: Derivative-based analysis with Eq.1.6 of the temperature variation of the dielectric relaxation time for each molar fraction of the OD $NPA_{1-x}NPG_x$ mixed crystals. The crossover between two distinct ranges of validity of the VFT model is visible as a sharp change of slope. The D and T_0 parameters are also shown . Insets: α and $\alpha\beta$ parameters characterizing the low- and high-frequency wings of the distribution of relaxation times, as obtained with the fits using the HN function.

	VFT ($T_g < T < T_B$)			DSM	
X	T_g [K]	T_0 [K]	D	T_C [K]	γ
0.1	143.7	106	8	130.0	9.3
0.2	143.5	87	22	128.0	11.2
0.3	160.0	134	5	150.0	9.2
0.4	155.5	107	14	139.2	11.4
0.48	154.8	89	26	139.5	11.8
0.5	158.6	111	14	146.8	10.8

Table 5.1: VFT fitting parameters (T_0 and D) for the data below the crossover temperature T_B, and DSM fitting parameters (critical temperature T_C and exponent γ), as a function of the molar concentration x. The values of the glass transition temperature T_g as extrapolated from the VFT fits are also listed.

($\gamma = 9$) proposed by Colby [12], and by a critical temperature T_C ranging between 128 and 150 K (see Table 5.1). The DSM seems therefore to describe well the dynamics of OD phases for temperatures slightly above the glass temperature. The various characteristic temperatures for the $NPA_{1-x}NPG_x$ mixed crystals are displayed in Figure 5.8.

The variation with temperature of the HN parameters describing the low- and high-frequency wings of the relaxation is displayed in the insets to Figure 5.6 for all the mole fractions of the $NPA_{1-x}NPG_x$ mixed crystals. From the insets to Figure 5.6 one may also observe that the width and asymmetry of the α-relaxation process varies with temperature and is composition-dependent. In all cases there is a crossover in the shape parameters and therefore in the distribution of relaxation times. For each composition, such change in the HN parameters occurs virtually at the same temperature as the crossover temperature obtained from

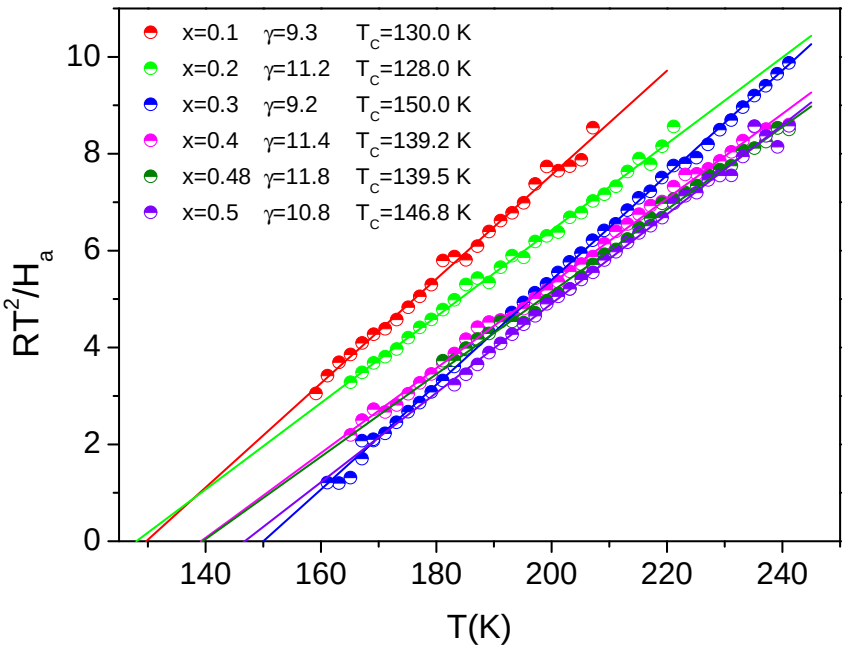

Figure 5.7: Derivative-based analysis of the temperature variation of the dielectric relaxation according to the critical-like DSM behaviour (eq. 5.2), for various molar fractions x of $NPA_{1-x}NPG_x$ mixed crystals.

the derivative-based analysis based on the VFT model. The dynamic crossover is found to occur at a relaxation time close to $10^{-3\pm1}s$ regardless of the composition of the mixed crystal. The crossover temperatures obtained from the derivative-based analysis and from the temperature dependence of the HN parameters are in agreement for the whole range of concentrations under investigation. The observed values of α and $\alpha\beta$ clearly indicate a non-Debye nature of the relaxation, which could be caused by heterogeneities in the concentration due to statistic chemical disorder resulting in a distribution of relaxation times.

In section 1.2.1 we pointed out that the hypothesis underlying the DSM model is the existence of cooperative dynamics throughout cooperative

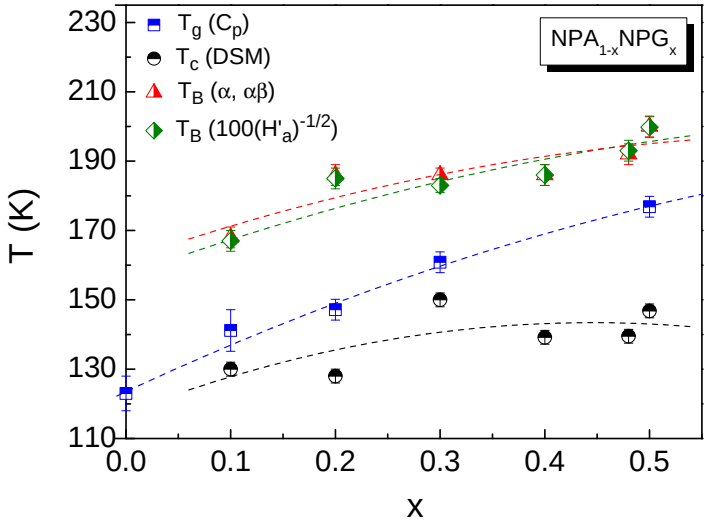

Figure 5.8: Characteristic temperatures for the $NPA_{1-x}NPG_x$ mixed crystals: glass transition calorimetric temperatures ($T_g(C_p)$, blue squares); crossover temperatures as calculated from the derivative-based analysis ($T_B(100(H_a/R)^{-1/2})$, green diamonds) and from the discontinuity of the HN parameters ($T_B(\alpha, \alpha\beta)$, red triangles); critical temperatures at which τ diverges according to the DSM model ($T_C(DSM)$, black circles).

rearranging regions (CRRs). According to such model, the length scale ξ of cooperative motion of all glass formers should exhibit a universal temperature dependence, which, assuming $\nu z = 9$, can be written as [13]:

$$\xi(T) = r_0 \left(\frac{T - T_C}{T_C} \right)^{-3/2} \tag{5.3}$$

Here T_C is the critical temperature of the DSM, which is lower than T_g, and r_0 (≈ 1.1Å) [14, 15] is the value of the cooperative length scale at $T = 2T_C$, assuming that cooperative motion still takes place at such temperature. The steepness index-based fragility coefficient defined as $m = [\partial \log \tau(T)/\partial(T_g/T)]_{T=T_g}$, has been shown experimentally to be

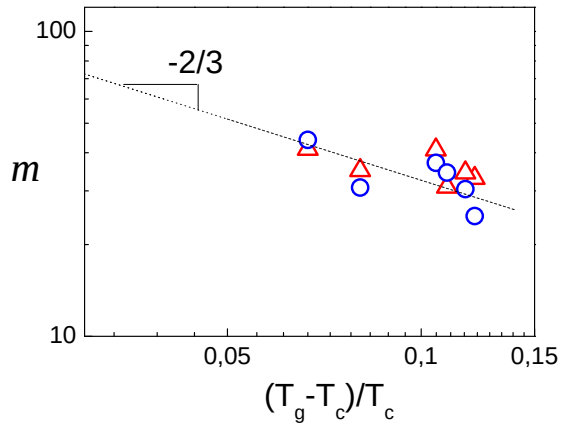

Figure 5.9: Fragility index calculated from the definition of fragility (Eq. 1.4) (triangles) and from the relation $m \approx 16 + 590/D$ [16] (circles) as a function of the normalized difference between glass and critical temperatures. Dotted line corresponds to the slope of the eq. 5.4. Errors are within the size of the symbols.

correlated with the quantity $(T_g - T_C)/T_C$. For a set of glass formers (low molecular weight organics, polymers, inorganics, etc.) the following relation has been shown to hold [13]:

$$m \cong 14[(T_g - T_C)/T_C]^{-2/3} \tag{5.4}$$

Inserting this into eq. 5.3 for $T = T_g$ one obtains:

$$\xi(T_g) \cong r_0 \left(\frac{m}{14}\right)^{9/4} [\text{Å}]. \tag{5.5}$$

Figure 5.9 displays the fragility coefficient as a function of the normalized difference between glass and critical temperatures for the OD $NPA_{1-x}NPG_x$ mixed crystals. It can be seen that there is a good agreement between the values calculated using equation 1.4 and the phenomenological equation $m \approx 16 + 590/D$ [16] when both are plotted together.

In the previous equation, D is the so-called strength coefficient, which measures the fragility of the compound and it is found from the VFT fits of the relaxation times. It is noteworthy that the value of the fragility strength coefficient decreases with decreasing temperature in successive dynamic domains. In "classical" glass formers, i.e., in supercooled liquids and polymers, the opposite behaviour occurs (namely the value of D is smaller in the immediate vicinity of T_g). Such unusual sequence was already noted in the isotropic phase of liquid crystalline materials [10] and in earlier tests on orientationally disordered solids [9]. For both cases this was associated with approaching the point of the near-continuous phase transition at which the dynamics are influenced by pretransitional fluctuations. The same can be postulated for the materials studied here.

It can be seen that the relationship predicted between the fragility and the scaled $T_g - T_C$ difference is fulfilled for these OD phases. By inserting the obtained fragility values into Eq. 5.5, the correlation length at T_g is found to be between 7 and 12 Å. Because the FCC lattice parameter of the mixed crystals is approximately 8.9 Å [4], this implies that the cooperative rearranging dynamics in plastic crystals are related to short-range fluctuations with a spatial extent of roughly one unit cell.

To the best of our knowledge, no experimental results have been published concerning cooperativity at the nanometer scale near the molecular glass transition, nor on the correlation length in plastic crystals [17]. Nevertheless, molecular dynamics simulations for adamantane derivatives [18] highlighted the existence of fluctuations on the same length scale as found here. This picture of CRR regions is very different from that emerging from other theories such as the random first-order transition [19], which predicts dynamically reconfiguring regions of much larger size ($100 - 200$ molecules). As for the size of the CRRs in glass, a wide range of values can

be found in the literature, but they are commonly much higher than 1 nm [20–22]. It should be pointed out that most of the published studies, as well as the one presented here, are model-dependent and thus subject to the validity of the theoretical model assumed to describe the data. Thus, the model-dependent analysis performed in this work concerning the size of CRR awaits non-dependent model data analysis to be confirmed.

5.5 Conclusions

We have shown that the dynamic scaling model (DSM) can perfectly account for the scaling exponent associated with the temperature dependence of the relaxation time for all NPA-NPG orientationally disordered (OD) mixed crystals, as analysed by using the linearised derivative analysis. The VFT-focused derivative-based analysis reveals instead two dynamic domains.

Values of obtained power ("critical") exponent are close to the DSM universal exponent $g = \nu z = 3/2 \times 6 = 9$. The exponent equal or close to 9 seems to be a general property of phases with only one kind of disorder (*e.g.*, translational for liquid crystals and orientational for plastic crystals). The perfect agreement with the DSM predictions allows us to the determine the correlation length of the cooperative rearranging regions. The obtained correlation length is comparable with the lattice parameter of the high-symmetry unit cell (which is less than 1 nm), so that the correlated dynamics should be thought of as corresponding to short-range fluctuations. Based on the results presented here as well as on the results of Refs. [9, 10, 23], the question arises whether the simple critical-like DSM description for orientationally disordered crystals is superior to the Vogel-Fulcher-Tamman parametrization used so far.

Bibliography

[1] R. Brand, P. Lunkenheimer, and A. Loidl *J. Chem. Phys.*, vol. 116, p. 10386, 2002.

[2] A. Criado, M. Jimenez Ruiz, C. Cabrillo, F. J. Bermejo, R. Fernandez-Perea, H. E. Fischer, and F. R. Trouw *Phys. Rev. B*, vol. 61, p. 12082, 2000.

[3] J. Salud, M. Barrio, D. O. López, J. Ll. Tamarit, and X. Alcobé *J. Appl. Crystallogr.*, vol. 31, p. 748, 1998.

[4] J. Salud, D. O. López, M. Barrio, and J. Ll. Tamarit *J. Mater. Chem.*, vol. 9, p. 909, 1999.

[5] D. O. López, J. Ll. Tamarit, M. R. de la Fuente, M. A. Pérez-Jubindo, J. Salud, and M. Barrio *J. Phys. Condens. Matter*, vol. 12, p. 3871, 2000.

[6] P. K. Dixon, L. Wu, S. R. Nagel, B. D. Williams, and J. P. Carini *Phys. Rev. Lett.*, vol. 65, p. 1108, 1990.

[7] M. Descamps and J. F. Willart *J. Non-Cryst. Solids*, vol. 172-174, p. 510, 1994.

[8] J. Ll. Tamarit, D. O. López, M. R. de la Fuente, M. A. Pérez-Jubindo, J. Salud, and M. Barrio *J. Phys. Condens. Matter*, vol. 12, p. 8209, 2000.

[9] A. Drozd-Rzoska, S. J. Rzoska, S. Pawlus, and J. Ll. Tamarit *Phys. Rev. B*, vol. 73, p. 184509, 2006.

[10] A. Drozd-Rzoska and S. J. Rzoska *Phys. Rev. E*, vol. 73, p. 041502, 2006.

[11] A. Drozd-Rzoska *Phys. Rev. E*, vol. 73, p. 022501, 2006.

[12] R. H. Colby *Phys. Rev. E*, vol. 61, p. 1783, 2000.

[13] B. M. Erwin and R. H. Colby *J. Non-Cryst. Solids*, vol. 307-310, p. 225, 2002.

[14] U. Tracht, M. Wilhelm, A. Heuer, H. Feng, K. Schmidt-Rohr, and H. W. Spiess *Phys. Rev. Lett.*, vol. 81, p. 2727, 1998.

[15] S. A. Reinsberg, X. H. Qiu, M. Wilhelm, H. W. Spiess, and M. D. Ediger *J. Chem. Phys.*, vol. 114, p. 7299, 2001.

[16] R. Böhmer, K. L. Ngai, C. A. Angell, and D. J. Plazek *J. Chem. Phys.*, vol. 99, p. 4201, 1993.

[17] K. Binder, J. Baschnagel, W. Kob, and W. Paul *Phys. World*, vol. 12, p. 54, 1999.

[18] F. Affouard, J. F. Willart, and M. Descamps *J. Non-Cryst. Solids*, vol. 307-310, p. 9, 2002.

[19] J. D. Stevenson, J. Schmalian, and P. G. Wolynes *Nat. Phys.*, vol. 2, p. 268, 2006.

[20] S. Capaccioli, G. Ruocco, and F. Zamponi *J. Phys. Chem. B*, vol. 112, p. 10652, 2008.

[21] D. Cangialosi, A. Alegria, and J. Colmenero *Phys. Rev. E*, vol. 76, p. 011514, 2007.

[22] C. Dalle-Ferrier, C. Thibierge, C. Alba-Simionesco, L. Berthier, G. Biroli, J. P. Bouchaud, F. Ladieu, D. L'Hôte, and G. Tarjus *Phys. Rev. E*, vol. 76, p. 041510, 2007.

[23] A. Drozd-Rzoska *J. Chem. Phys.*, vol. 130, p. 234910, 2009.

Chapter 6

DOUBLE PRIMARY RELAXATION IN A HIGHLY ANISOTROPIC ORIENTATIONAL GLASS-FORMER WITH LOW-DIMENSIONAL DISORDER

6.1 Introduction

The main difference between orientational and canonical glasses is that in the former the freezing involves exclusively the rotational degrees

of freedom of the molecules. While in structural glasses all six molecular degrees of freedom are frozen (*i.e.*, both orientational and translational ones), in orientational glasses the centrers of mass display positional order, and only the three orientational degrees of freedom are frozen. Hence orientational glasses are, in a sense, systems with fewer degrees of freedom than structural glasses. In this chapter a glass-forming system with yet a lower number of degrees of freedom is discussed, namely the solid phase of a quasi-planar benzene derivative which exhibits a layered structure of parallel planes in which the molecules can basically only rotate around a six-fold-like axis. We show that such phase is characterized by a double primary (collective) relaxation which is related to the low-dimensional character of the system and which results in a spectral landscape reminiscent of α relaxations characterized by an excess wing.

As discussed in chapter 2, the landscape of the secondary relaxations of canonical glass formers is enriched by the existence of the excess wing (EW), that is, a relaxation process which is not clearly resolved from the main α-relaxation process [1, 2]. Some authors [3] have proposed, by means of a comparative study on several canonical glass formers, that the EW could actually be a non-resolved secondary relaxation process immersed into the high-frequency wing of the main (α) relaxation. The physical origin of the EW has remained unclear until very recently, and at least three different scenarios have been hypothesized. On the one hand, a picture in which the EW is an inherent feature of the α relaxation, thus present in all glass formers. On the other hand, a scenario where the EW is in fact a JG relaxation hidden below the predominant α relaxation. Finally, there is also the opposite view according to which the JG relaxation does not exist in strong glasses and the EW is related to motions different from that related to the JG relaxation and appearing exclusively below the

melting temperature [4, 5]. In recent work on canonical glasses, application of high pressures revealed that the EW is in fact a "submerged" secondary relaxation. An invariance of the frequency separation between the α relaxation process and such secondary relaxation has also been revealed by probing isochronal conditions within the temperature-pressure diagram (see also chapter 8) [6]. These studies have thus concluded that the EW is in fact the JG secondary relaxation, as shown e.g. for the case of glycerol [7], ethanol [8], and some propylene glycol oligomers [9].

As far as orientationally disordered materials are concerned, an earlier work [10] based on the study of several OD phases concluded that the EW is absent and thus not a universal picture for such glass formers. However, few years later the same authors reported [11] the possible existence of an EW in a hexasubstituted benzene derivative, namely pentachloronitrobenzene. Pentachloronitrobenzene (PCNB, chemical formula $C_6Cl_5NO_2$) displays, in the condensed phase, a stacked structure of molecular planes in which the PCNB molecules lie flat on each plane and occupy the sites of an hexagonal lattice [12, 13]. The phase behaviour of this structure has been extensively studied [11–19], and a glass transition has been reported by adiabatic calorimetry around 185 K, assigned to the freezing of the orientational disorder within the triangular planes [17]. Similar results were found by Correia *et al.* by DSC and thermally stimulated currents, with a reported glass transition temperature of 191 K [18, 19].

In order to shed light into the actual nature of the excess wing of PCNB, and to clarify the connection between the dielectric peculiarities results and those of crystallographic studies, we have probed the relaxation dynamics of PCNB by means of dielectric spectroscopy as a function of temperature and pressure. We find that the excess wings in fact a

separate relaxation than the α process, and that is not a Johari-Goldstein precursor. An assignment based on the materials anisotropy is proposed.

6.2 Experimental details

PCNB was purchased from Aldrich (purity 99%). Differential scanning calorimetry was used to check the purity of the compound by measuring the melting temperature, which was in agreement with the reported value (417.2 K). Hence, the material was used as received. Ambient-pressure calorimetric measurements (section 3.1.1) were carried out with heating and cooling rates of 5 K/min. High-resolution X-ray powder diffraction profiles (section 3.1.3) were recorded in the temperature range between 150 and 300 K, with an acquisition times of 2 hours for each temperature. PVT measurements (section 3.1.2) on PCNB were carried out at 336.15, 304.15, and 294.15 K in the pressure range between 0.1 and 270 MPa.

The broadband dielectric spectroscopy measurements at ambient pressure (see section 3.2.1) were performed using a capacitor prepared by pressing the PCNB powder between two stainless steel disks using a hydraulic press (120 kN). The spectra were taken in the temperature range between 188 K and 394 K every 2 K. Pressure-dependent dielectric measurements (section 3.2.2) were also performed, between ambient pressure and 0.6 GPa. For these studies, the material under investigation was pressed between two parallel stainless steel plates as in the ambient pressure measurements, and in order to prevent a possible contamination with the pressurizing fluid (thermal oil from Huber), the capacitor was covered by a Teflon membrane and latex wrapping. The temperature was controlled by thermal baths (Lauda Proline RP 1290 and Huber Unistat) with a liquid flow circuit connected to the high-pressure setup.

Isothermal pressure scans were taken at 262, 274, 284, 304 and 334 K, and an isobaric measurement at 0.3 GPa was performed in the temperature range between 274 K and 324 K.

6.3 Structural Study

Concerning the structural characteristics of the material under scrutiny, a Monte Carlo computer simulation modelling available single-crystal diffuse X-ray scattering data [12] has shown that the solid phase of PCNB, which melts at ca. 417 K, is rhombohedral (space group $R\bar{3}$) with each site of the crystal containing a molecule in one of the six possible different orientations in the plane, each occupied with equal probability. Figure 6.1 shows the average structure of PCNB as reported in Ref. [12]. Singe-crystal neutron diffraction data has confirmed the $1/6 : 5/6$ $NO_2 : Cl$ occupation factors and shown that the O atoms of the NO_2 group are rotated out of the benzene plane in such a way that both planes are 74° apart [13]. The latter study has moreover revealed that the U_{33} components (along the c axis) of the tensor for the anisotropy displacement parameters are much larger than the U_{11} and U_{22} principal coefficients (of the (001) in-plane displacements) whatever the temperature and for all atoms, but specially for Cl, N and O.

Motivated by these findings, we have set out to study the temperature dependence of the lattice parameters. To this aim we acquired isothermal X-ray powder diffraction profiles as a function of temperature. The diffraction pattern measured at 300 K (Figure 6.2) matches well the pattern simulated using the structural data from Thomas *et al.* [12] The similarity between the diffraction profiles acquired at distinct temperatures (not shown) confirms that no structural change takes place in the 150-300

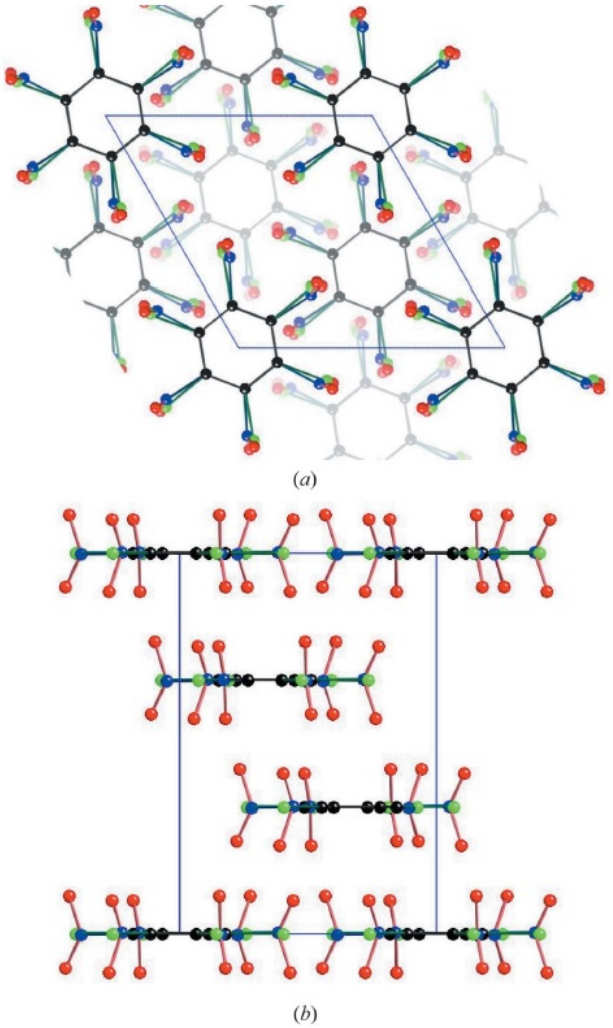

Figure 6.1: Average structure of PCNB. Each of the six substituent sites in every molecule contains 1/6 NO_2 and 5/6 Cl. Red dots represents the O atoms, blue the N atoms, green the Cl atoms and black the C atoms. View along the [001] direction (a) and along the [100] direction (b) [12].

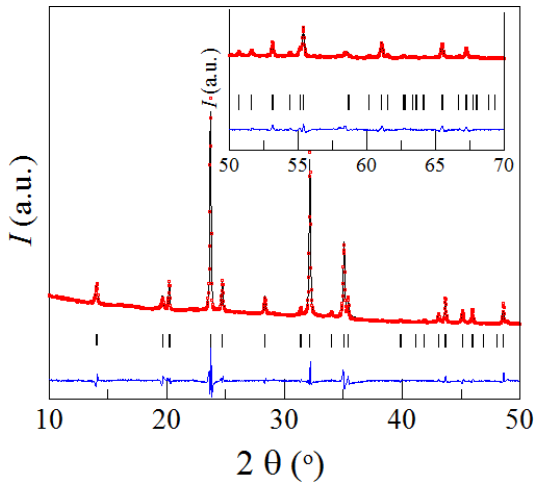

Figure 6.2: Experimental X-ray diffraction pattern of PCNB at room temperature (red circles). The black line corresponds to the calculated X-ray diffraction patterns determined by Rietveld refinement. The difference profile (blue line) and Bragg reflections (vertical bars) are also shown.

K range. We used these data as starting point for the refinement of the lattice parameters by means of the Pattern Matching option of the Full Prof program [20]. Figure 6.3 shows the temperature-dependence of the lattice parameters and of the unit cell volume normalized to the number of molecules Z in the cell, from below the glass transition to room temperature. The continuous variation of the lattice parameters (and, as a consequence, of the volume per molecule) together with the discontinuity in the volume expansivity (defined as $\alpha_V = 1/V(\partial V/\partial T)_P$) are irrefutable signatures of a glass transition which takes place at approximately 187 K.

From Figure 6.3(a) we can observe that, as the temperature decreases, the lattice contracts more in the c direction ($\alpha_c(T = T_g) =$

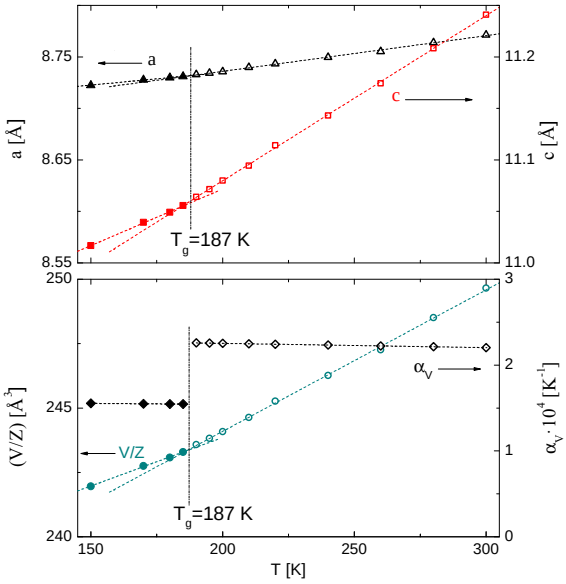

Figure 6.3: Upper panel: lattice parameters a (open and closed triangles) and c (open and closed squares). Lower panel: molecular cell volume (open and closed circles) and thermal expansivity (open and closed diamonds) as a function of temperature.

$1/c(\partial c/\partial T)_P = 1.45 \cdot 10^{-3} K^{-1}$) than within the (001) planes ($\alpha_a(T = T_g) = 1/a(\partial a/\partial T)_P = 4.0 \cdot 10^{-5} K^{-1}$). Also, the kink at the glass transition in the temperature dependence of the lattice parameter c is much more pronounced than that of the parameter a, the change of the slope being more than one order of magnitude different. In other words, the inter-plane structural parameter is much more affected by changes of temperature and by the glass transition than any intraplane distance. This is obviously directly related with the larger values of the U_{33} component compared to U_{11} and U_{22} [13].

6.4 Dielectric Spectroscopy Study

Figure 6.4 displays several spectra of the imaginary part of the complex permittivity, measured both isothermally (a,b) and isobarically (c). The isothermal spectra were acquired at ambient pressure from the glass transition temperature up to a temperature close to the melting point. They are shown in panel (a) and, for a reduced set of temperatures, in panel (b). In Figure 6.4(c) we show some of the spectra obtained at constant temperature (334 K) as a function of pressure. In all spectra a clear relaxation peak is observed, displaying continuous temperature and pressure shifts characteristic of the freezing of the molecular dynamics on cooling and pressurizing. The frequency position and temperature dependence of the main peak are in agreement with early dielectric studies on PCNB [14–16]. The observation of a reorientational process is in line with the orientational disorder observed in diffraction studies. It can be observed in Figure 6.4 that the profile of the loss feature is not that expected in the case of a single relaxation process. Rather, in all spectra in addition to a well-pronounced main peak (hereafter α relaxation), an excess wing (hereafter called α' process) is clearly visible as a shoulder to the main peak. The fact that this loss process appears as a shoulder indicates that its dielectric strength is lower than that of the main loss (see also below). Figure 6.4(b) highlights the need of two dipolar processes (displayed as dotted lines) for modelling the dielectric spectra. It should be noticed that in previous work [11, 21] only one HN function was employed to fit the loss curves, resulting in a slight discrepancy between the experimental data and the fit function in the high-frequency range of the spectra.

From Figure 6.4(a) one can observe that at the glass transition tem-

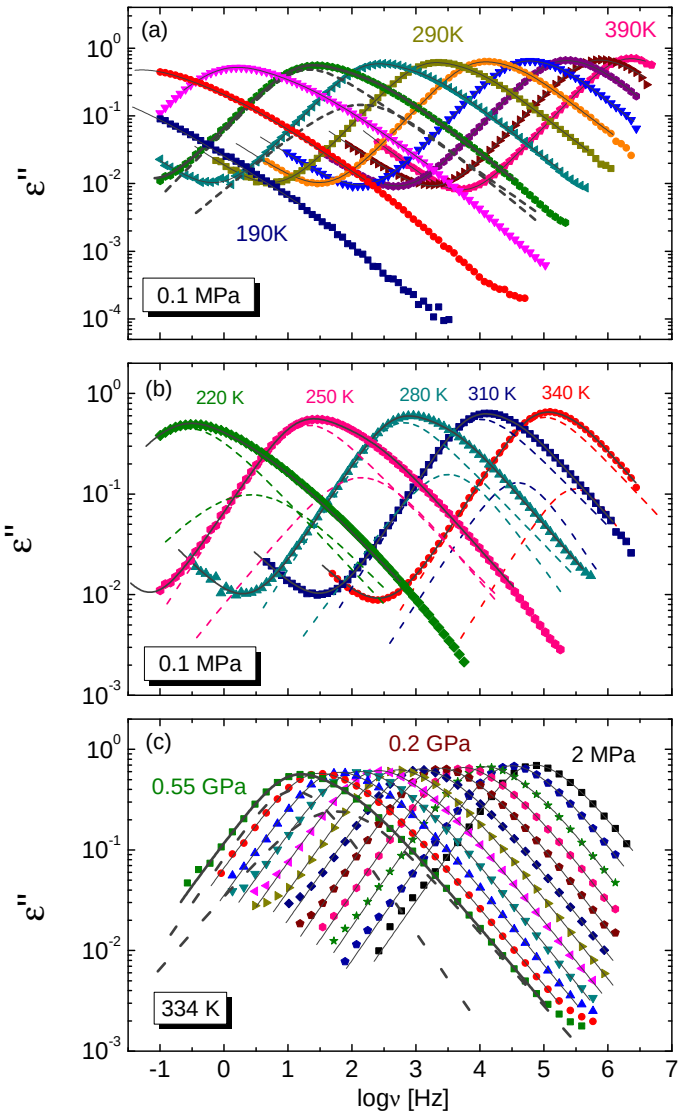

Figure 6.4: (a,b) Dielectric loss curves acquired at ambient pressure between 390 K and 190 K every 20 K (a) and for a reduced set of temperatures (b) to highlight the spectral shape. (c) Dielectric spectra at constant temperature (334 K), acquired between 2 and 550 MPa every 50 MPa. The solid lines represents the fits of the spectra as the sum of two components, shown explicitly with dotted lines at 250 K (a), for all temperatures in (b), and at 550 MPa (c).

perature (at about 190 K), the frequency position of the main peak in the loss spectrum is observed well below 10^{-1} Hz, namely at times close to 100 s, thus confirming the identification of such main loss as the α relaxation directly associated with the glass transition. The possible origin of the second relaxation feature at higher frequency (process α') will be discussed in the next section. All measured PCNB spectra were fitted using a combination of a Havriliak-Negami (HN) function for the main relaxation (α) together with a Cole-Cole (CC) function for the shoulder relaxation (α'). The resulting fits are shown as continuous lines in Figure 6.4; it can be seen in all three panels that the model provides quite accurate fits. A reasonable physical consistency was found for the fit parameters: the shape parameters of the HN function were in the ranges $0.61 < \alpha_{HN} < 1$ and $0.62 < \beta_{HN} < 1$, corresponding to a stretched exponent β_{KWW} between 0.68 and 1; the α' process (described with a Cole-Cole function) was characterized by an exponent in the range $0.61 < \alpha_{CC} < 1$.

The characteristic relaxation times of both processes, as obtained from the fitting procedure, are plotted in Figure 6.5 both as a function of temperature at normal pressure (upper panel) and as a function of pressure at constant temperature (lower panel). It can be observed in Figure 6.5 that the two relaxations (α and α') have similar but not identical dependencies on T and P. This shows that the α' process is not an excess wing (as suggested by the spectral lineshape of isobaric measurements) but a separate dynamical process than the α relaxation. The isobaric data could be fitted using a VFT line-shape (see eq. 1.3), while an Arrhenius-like equation was used for the data at constant temperature.

The values of the glass-transition temperatures and pressures, fragility and activation volume are reported in Table 6.1 for all measurements.

The low fragility values obtained from isobaric measurements indicate

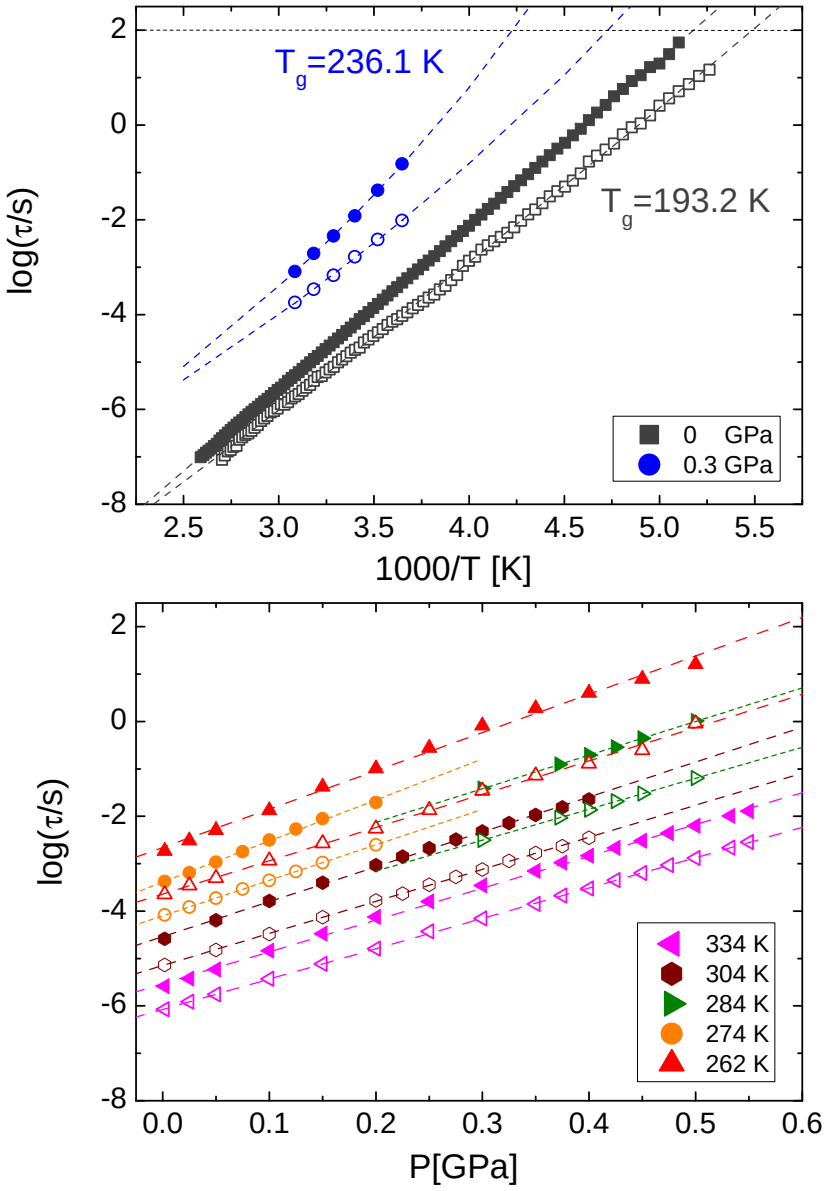

Figure 6.5: Relaxation times for the α (closed symbols) and α' (open symbols) relaxations as a function of the reciprocal temperature for isobaric measurements (upper panel), and as a function of pressure for isothermal measurements (lower panel). The constant temperatures or pressures employed are indicated in the legends.

P (MPa)	process	T_g (K)	m
0.1	α	193.2 ± 0.1	18.2 ± 1.2
	α'		18.6 ± 2.5
300	α	236.1 ± 0.2	22.5 ± 1.8
	α'		19.6 ± 1.4
T (K)	process	P_g (MPa)	$\Delta V^{\#}$ (cm^3/mol)
334	α	1120 ± 14	43.0 ± 0.4
	α'		40.9 ± 0.1
304	α	890 ± 14	42.9 ± 0.5
	α'		39.4 ± 0.1
284	α	780 ± 9	38.6 ± 0.2
	α'		35.5 ± 0.3
274	α	620 ± 17	45.4 ± 0.9
	α'		39.3 ± 0.1
262	α	580 ± 23	40.6 ± 0.9
	α'		35.2 ± 0.5

Table 6.1: Values of the glass-transition temperature (T_g) and pressure (P_g), fragility (m) and activation volume ($\Delta V^{\#}$) for the measurements at constant pressure and temperature shown in Figure 6.4.

that PCNB is a quite a strong glass former, as also confirmed by the linear dependence of $log\tau$ on pressure. The activation volume exhibits a non-monotonic dependence on temperature, which is atypical since it usually increases with decreasing temperature [22]. The relatively large error bar associated to the calculated values of $\Delta V^{\#}$ excludes however a more detailed analysis.

Figure 6.6 shows that the shape of the loss spectra is almost the same for different combinations of T and P chosen so as to maintain the same value of the relaxation time for the α process, namely at the isochronal value $log(f_{max_\alpha}) = 2.4$ corresponding to ca. 0.6 ms. The figure evidences that the relative position and strength of both processes and the overall shape of the spectra are unchanged despite the large range of temperatures and pressures spanned by the experiments. The rough superposition of all isochronal spectra into a single master curve indicates that the two dynamic processes have similar dependence upon the thermodynamic parameters, as also visible in Figure 6.5, highlighting a strong correlation between both relaxations.

It is worth noting that a relaxation phenomenology similar to PCNB has been reported in related molecular systems, namely discotic liquid crystals consisting of phenyl-based, rigid disk-shaped aromatic flat cores functionalized with flexible polar sidegroups [23–25]. These materials, whose constituent molecules can be considered to be larger "cousins" of the hexasubstituted benzenes, display in fact two dielectric relaxations with different characteristic times but virtually identical temperature dependences [24]. Also in the case of discotic crystals, the lower-frequency relaxation corresponds to the main α process, as discernible from the position of the loss maximum at the corresponding T_g (determined from calorimetry measurements), and the second (α') process at higher fre-

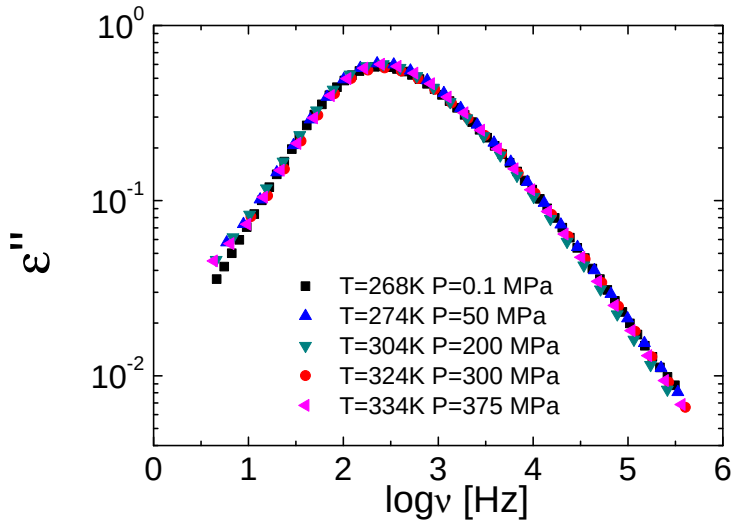

Figure 6.6: Superposition of loss spectra measured for a combination of temperatures and pressures displaying the main relaxation peak at the same frequency $f_{max} = 251$ Hz ($\tau_{max} \approx 0.6$ ms).

quency displays lower dielectric strength than the first one.

It is possible to obtain a "thermodynamic" scaling of all the data $\tau_\alpha(T, P)$ as a function of the scaling variable $1000/TV^\gamma$ (section 1.2.2). To do so, it is necessary to find the equation of state $V(T, P)$ for PCNB to be able to calculate the specific volume at every pressure and temperature. This can be done by modelling the experimental PVT curves by means of the Tait equation (eq. 1.16). Figure 6.7 shows the volume measurements as a function of pressure for PCNB collected at three fixed temperatures; the green solid lines represent the simultaneous model of all three curves using the Tait equation. The result of the thermodynamic scaling of the relaxation time data is shown in Figure 6.8. It can be seen that the α and α' relaxations scale with slightly different factors, namely, that the value of γ is different in each case, being $\gamma_\alpha = 7.60 \pm 0.02$ and $\gamma_{\alpha'} = 7.81 \pm 0.01$

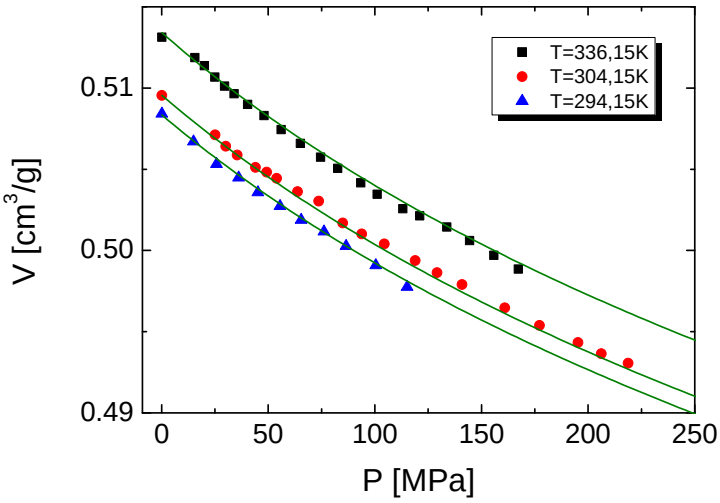

Figure 6.7: Specific volume of PCNB as a function of pressure at fixed values of temperatures (PVT measurements). The green lines corresponds to the Tait equation used to model all the data simultaneously.

respectively. This again confirms that the α and α' processes corresponds to different dynamics.

From the comparison of temperature- and pressure-dependent measurements it is possible to determine whether the molecular dynamics is dominated (limited) by the thermal energy or by the available free volume. In particular, one can use the ratio between the activation enthalpy at constant volume ($E_V = R[\partial log\tau/\partial T^{-1}]_V$) and the activation enthalpy at constant pressure ($E_P = R[\partial log\tau/\partial T^{-1}]_P$): if this ratio is between 0 and 0.5, then the dynamics is volume-dominated and if it this between 0.5 and 1 the dynamics is temperature-dominated [50]. We have estimated both activation enthalpies by considering the isothermal data presented in the lower panel of Figure 6.5. The enthalpy at constant pressure was obtained plotting the relaxation times of both α and α' relaxations obtained in the isothermal measurements at pressures between normal pressure and

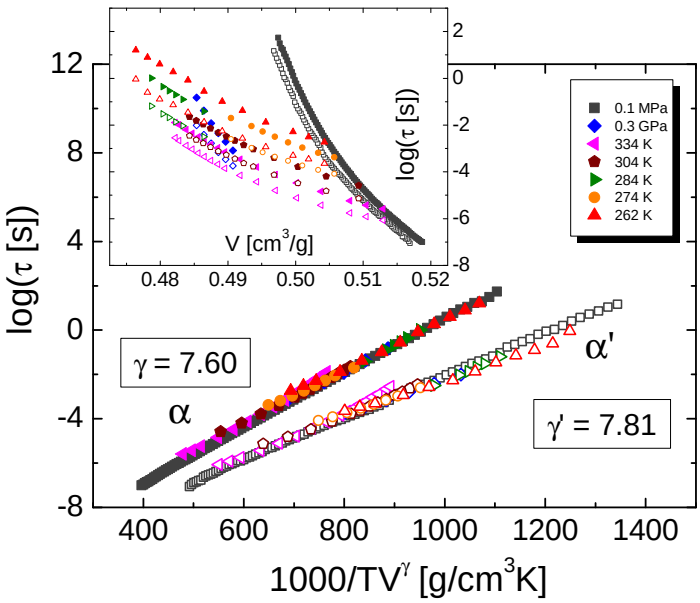

Figure 6.8: Thermodynamic scaling of the relaxation times for the α (closed symbols) and α' (open symbols) processes as a function of the scaling quantity $1000/TV^{\gamma}$. Inset: relaxation times of both α (closed symbols) and α' (open symbols) processes as a function of the specific volume calculated at the appropriate (P,T) values by means of the Tait equation (eq. 1.16).

0.6 GPa every 0.1 GPa as a function of the corresponding temperatures, and then calculating the activation enthalpy as the slope of the linear fit of such plot. The obtained values of E_P are in the range between 3428 and 4648 K for the α process and between 2972 and 3503 K for the α' process. For the enthalpy at constant volume, we plotted again the same data (relaxation times) as a function of the specific volume calculated at the appropriate (P,T) values by means of the Tait equation 1.16. The result is shown in the inset to Figure 6.8. The enthalpy at constant volume was then obtained by plotting the relaxation times of both α and α' relaxations at three fixed specific volumes (V=0.485, 0.500

and 0.505 cm^3/mol) as a function of the corresponding temperatures, and then calculating the slope of the linear fit of such plot. The obtained E_V values lie between 2518 and 2584 K for the α process and between 1779 and 2246 K for the α' process. The ratio E_V/E_P is found to lie between 0.51 and 0.77 for both the α and α' processes, which would indicate that both dynamics are temperature-dominated. Moreover, the ratio decreases with increasing pressure, as expected because a pressure increase entails a increase of the density and therefore a higher activation volume barrier.

6.5 Origin of the two relaxation processes

Given the rigidity of the hexagonal carbon backbone of the PCNB molecule and of the bonds to the side groups Cl and NO_2, the α' process cannot be attributed to the motion of an intramolecular dipole moment behaving independently from the main dipole moment of the molecule. The motion of Cl atoms with respect to the carbons can only give rise to vibrational modes in the IR region of the electromagnetic spectrum. If intramolecular motions of the NO_2 sidegroups took place, given the small mass of the NO_2 group they would also be much faster than either the α and α' processes, at least like the β relaxation reported in an earlier study at much lower temperature (between 140 and 170 K, *i.e.*, clearly below T_g) and with relaxation times far away from those here reported ($\tau_\beta \approx 1$ ms at 140 K) [11]. Single-crystal neutron diffraction studies have shown that the NO_2 plane (i.e., the plane containing the N atom and both oxygens) is not coplanar with that of the benzene-like ring, but that the two planes form in fact a (fixed) angle of 74°. The NO_2 group is occupationally disordered and displays large displacements and torsional vibrations accompanying whole-molecule librations; however, according

to the diffraction studies it doesn't display rotations around the C-N axis. Hence the α' process cannot correspond to a reorientation of the NO_2 dipole independent of that of the rest of the molecule [13].

At the same time, the α' process cannot be identified as the primitive (Johari-Goldstein) precursor relaxation of the α process. In fact, a correlation between the α- and β_{JG}-relaxation times has been experimentally proven, based on empirical findings on a large number of glass formers [26]. According to these studies, the primitive JG relaxation time (τ_{JG}) is related to the α-relaxation time (τ_α) as (see section 2.3.2.1):

$$\tau_{JG} = (t_c)^{1-\beta_{KWW}} \tau_\alpha^{\beta_{KWW}} \tag{6.1}$$

Here, t_c is the crossover time which marks the onset of the many-body dynamics (typically $t_c \approx 2$ ps in molecular glass-formers) and β_{KWW} is the stretched exponent of the Kohlrausch-Williams-Watts function representing the α-relaxation process. By using, for example, the value of τ_α of Figure 6.6 ($\tau_\alpha = 0.63 \cdot 10^{-3}$ s) and the corresponding β_{KWW} value (≈ 0.90), the calculated τ_{JG} is found to be two decades smaller than $\tau_{\alpha'}$.

It follows that the origin of the α' loss cannot be a secondary relaxation of any kind, but must instead stem from the motion of the PCNB molecule as the primary α relaxation (as testified by their similar behaviour, see (Figure 6.6). The pressure- and temperature-dependences of both α and α' relaxation processes are in fact very strong correlated. This is visualized Figure 6.9, where the relaxation time of the α' process is plotted (in logarithmic scale) versus that of the α relaxation for a set of temperatures and pressures. The correlation between both reorientational processes is evident, which shows that both relaxation processes are connected by a power-law dependence.

To identify the origin of the α' feature, it is helpful to compare our

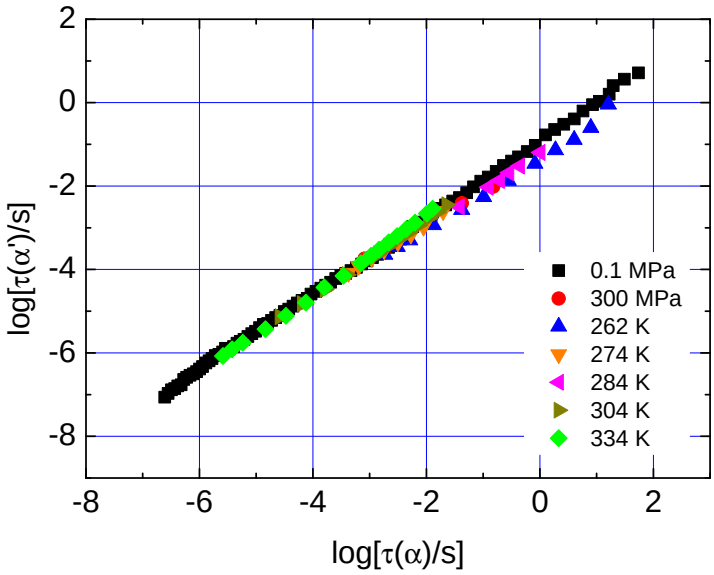

Figure 6.9: Relaxation time of the α' process as a function of the relaxation time of the α process for a set of temperatures and pressures.

BDS results with structural data and with dielectric relaxation results on discotic liquid crystal systems. The dipole moment of the PCNB molecule ($\mu = 2.33$ D [14]) is determined to a large extent by that of the NO_2 sidegroup. In the solid phase, the NO_2 group of a PCNB molecule, which, as mentioned, is tilted with respect to the (001) plane, points towards a C-Cl bond of a molecule in the next layer and away from its NO_2 group (both molecules being related by an inversion centre), whereas the other chlorines of both molecules are bent towards each other. These correlations are accompanied by large atomic displacements compared with the spacing between intermolecular layers along the c axis (3.75 Å), which imply a high level of molecular distortion. This has been confirmed by Monte Carlo simulations of the diffraction data, in which very large displacements were needed to reproduce the intense and broad diffuse scattering background [12]. The local displacements, evidenced

both by Monte Carlo simulations and by the analysis of the diffraction data by Thomas *et al.* [12], result in an increase of the intermolecular $NO_2 \cdots NO_2$ and $NO_2 \cdots Cl$ nearest-neighbour distances and a decrease of the $Cl \cdots Cl$ ones.

These findings suggest that intermolecular interactions mediated by NO_2 and Cl groups are responsible for strongly correlated displacements and distortions which prevent the formation of an ordered crystalline structure. Hence the at first sight flat, 2D-like benzene derivative is in fact a 3D-like molecule with strong fluctuations. Because of the intermolecular interactions involving the NO_2 groups, the molecular dipole cannot lie exclusively on the (001) layers but must possess a component along the c axis. The molecular dipole of PCNB (largely due to the nitro group) has therefore a larger component orthogonal to c, and a shorter one along c. The reported molecular displacements imply that both components, and in particular the one parallel to c, exhibit very large fluctuations; due to steric effects, these fluctuations are strongly correlated between one molecule and the next, *i.e.* they are necessarily highly cooperative.

The above discussion implies that the in-plane and out-of-plane anisotropy of PCNB is reflected both in the microscopic dipole moments and in their mutual interactions: the molecular dipoles have two non-zero (in-plane and out-of-plane) components, and they also display very anisotropic coupling in the in-plane and out-of-plane directions. Such a situation is reminiscent of that of columnar hexagonal phases of discotic liquid crystals of disk-shaped molecules with disordered flexible sidegroups (alkyl or other substituent chains). These molecules possess dipole moments (associated with the flexible sidegroups) which are not oriented parallel to the molecular disk, and which display highly anisotropic interactions in two directions, namely within the same column and

between adjacent column [23–25]. Discotic liquid crystals also display a "double" primary relaxation with similar temperature dependence as found in PCNB. In other words, the two systems, PCNB and discotic liquid crystal, share both the same degree of anisotropy and a similar phenomenology.

In light of this, we are lead to assign the α and α' relaxations in the dielectric spectra to the in-plane and out-of-plane components of the dipolar moment of the PCNB molecules. In particular, we ascribe the main α process to the reorientational motions of the molecular dipole within the (001) planes, *i.e.* to molecular reorientational jumps which modify directly the in-plane component of the dipole moment. As mentioned above, the larger dipole component lies on the (001) plane and consequently its reorientational dynamics must exhibit higher dielectric strength. The second process, α', slightly faster than the α process, is instead connected with the relaxation of the dipole component fluctuating around the c hexagonal axis, *i.e.*, with "shaking" motions of the PCNB molecules that leave basically invariant the in-plane component, but which affect strongly the out-of-plane contribution of the molecular dipole (significantly shorter than the in-plane one). The relative dielectric strength of the α and α' processes, shown in Figure 6.10, corroborates this assignment, since the strength of the main α process is larger than that of the α' process for all values of the thermodynamic parameters. It can be moreover observed that the strength of the α' process diminishes with respect to that of the α process with decreasing temperature. This effect is much more accentuated at high pressure and low temperatures. Since the increase of pressure or the reduction of temperature have a much stronger effect on the c lattice parameters, the assignment of the α' relaxation to the dynamics along the c direction rationalizes the pronounced effect of P or

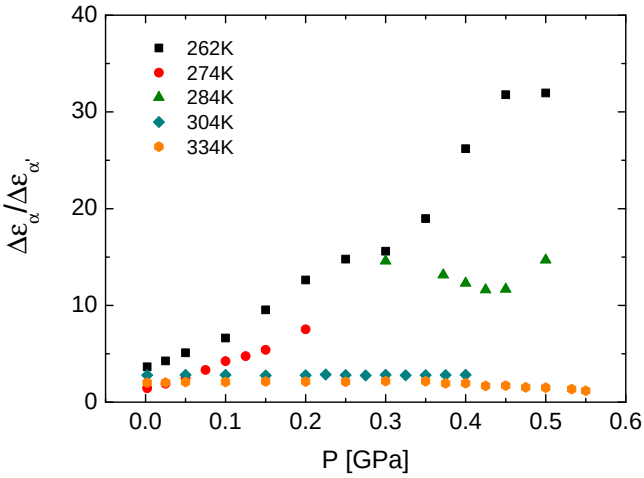

Figure 6.10: Ratio between the dielectric strength of the α- and α'- relaxation process as a function of pressure for a set of temperatures.

T changes on this relaxation feature.

Also the fact that the α' process is observed at higher frequency (that is, at shorter times) can be rationalized with our assignment. In fact, the dipole component in the plane relaxes by whole-molecule rotations inside the plane; these are limited by the steric hindrance of the sidegroups of neighbouring PCNB molecules in the same plane, which is large as evidenced by the small expansivity in the (001) plane. In contrast, the vertical component of the dipole can relax only through the fluctuations of the out-of-plane dipole component and is therefore affected by the smaller inter-plane hindrance associated with the soft interactions along c, as evidenced by the large expansivity along c.

We finally discuss the shape of each spectral component. The pressure dependence of the stretched β_{KWW} exponents are displayed in Figure 6.11 for both relaxations at two fixed temperatures. For the α process, the β_{KWW} parameter (obtained from the parameters of the HN function

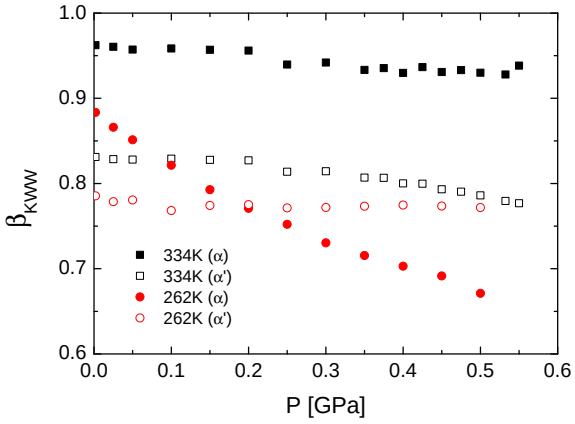

Figure 6.11: Values of the β_{KWW} exponent for the α and α' processes at fixed temperature as a function of pressure.

as $(\alpha_{HN}\beta_{HN})^{1/1.23}$) decreases as the pressure increases, this behaviour being more relevant at high-temperature and, as usual, it increases with temperature at constant pressure. The β_{KWW} for the α' process (obtained from the exponent of the Cole-Cole function as $(\alpha_{CC})^{1/1.23}$) decreases slowly with the decrease of temperature and is almost invariant with pressure. It should be noticed that the β_{KWW} values for the α' process are noticeably smaller than those for the α process at high temperature as well as at low pressure, which entails that the α' relaxation is more cooperative than the α relaxation except at very high pressure and low temperature. The pronounced cooperativity of the α' relaxation again confirms its "primary" nature.

6.6 Conclusions

This study is, to the best of our knowledge, the first one on the slow dynamics of statistical disordered structures under simultaneous

variations of temperature and pressure through dielectric spectroscopy. Despite the long-range translation order of PCNB, its rotational dynamic properties display very strong similarities to those of structural glass-formers: (i) the dependence of the glass transition on pressure is similar to that of van der Waals molecular liquids; (ii) the overall rotational relaxation function is invariant if considered at isochronal conditions. For the studied temperature and pressure ranges, the dynamics reveals two relaxation processes very close in time scale, correlated via a power law over different isothermal and isobaric measurements, which have been attributed to, respectively, the in-plane reorientational motions of the molecules within the (001) plane (α process), which are frozen at T_g=193 K, and the out-of-plane faster contribution, associated with the relaxation of the residual dipole fluctuating around the c hexagonal axis (α' relaxation). The strength of the α' process is lower since the component parallel to the c axis is smaller than that orthogonal to it, and the dynamics of both processes is different due to the anisotropy of intermolecular interactions.

Bibliography

[1] A. Kudlik, S. Benkhof, T. Blochowicz, C. Tschirwitz, and E. Rössler *J. Mol. Struc.*, vol. 479, p. 201, 1999.

[2] K. L. Ngai and M. Paluch *J. Chem. Phys.*, vol. 120, p. 857, 2004.

[3] U. Schneider, R. Brand, P. Lunkenheimer, and A. Loidl *Phys. Rev. Lett.*, vol. 84, p. 5560, 2000.

[4] H. Tanaka *J. Chem. Phys.*, vol. 111, p. 3175, 1999.

[5] H. Tanaka *J. Non-Cryst. Solids*, vol. 351, p. 3396, 2005.

[6] M. Mierzwa, S. Pawlus, M. Paluch, E. Kaminska, and K. L. Ngai *J. Chem. Phys.*, vol. 128, p. 044512, 2008.

[7] A. A. Pronin, M. V. Kondrin, A. G. Lyapin, V. V. Brazhkin, A. A. Volkov, P. Lunkenheimer, and A. Loidl *Phys. Rev. E*, vol. 81, p. 041503, 2010.

[8] R. Brand, P. Lunkenheimer, U. Schneider, and A. Loidl *Phys. Rev. B*, vol. 62, p. 8878, 2000.

[9] R. Casalini and C. M. Roland *Phys. Rev. B*, vol. 69, p. 094202, 2004.

[10] R. Brand, P. Lunkenheimer, U. Schneider, and A. Loidl *Phys. Rev. Lett.*, vol. 82, p. 1951, 1999.

[11] R. Brand, P. Lunkenheimer, and A. Loidl *J. Chem. Phys.*, vol. 116, p. 10386, 2002.

[12] L. H. Thomas, T. R. Welberry, D. J. Goossens, A. P. Heerdegen, M. J. Gutmann, S. J. Teat, P. L. Lee, W. C. C., and C. J. M. *Acta Cryst.*, vol. B63, p. 663, 2007.

[13] J. M. Cole, H. Bürgi, and M. G. J. *Phys. Rev. B*, vol. 83, p. 224202, 2011.

[14] A. Aihara, C. Kitazawa, and N. A. *Bull. Chem. Soc. Jpn*, vol. 43, p. 3750, 1970.

[15] P. G. Hall and G. S. Horsfall *J. Chem. Soc., Faraday Trans. 2*, vol. 69, p. 1071, 1973.

[16] H. A. Kolodziej, K. Orzechowski, R. Szostak, P. Freundlich, T. Glowiak, and S. Sorriso *J. Mol. Struct.*, vol. 380, p. 15, 1996.

[17] Z. C. Tan, Y. Nakazawa, K. Saito, and M. Sorai *Bull. Chem. Soc. Jpn*, vol. 74, p. 1221, 2001.

[18] N. T. Correia, J. J. Moura Ramos, and H. P. Diogo *J. Phys. Chem. Solids*, vol. 63, p. 1717, 2002.

[19] J. J. Moura Ramos and N. T. Correia *Mol. Cryst. Liq. Crys.*, vol. 404, p. 75, 2003.

[20] J. Rodríguez-Carvajal, "Fullprof suite: Crystallographic tools for rietveld, profile matching & integrated intensity refinements of x-ray and/or neutron data."

[21] M. Shahin and S. S. N. Murthy *J. Chem. Phys.*, vol. 118, p. 7495, 2003.

[22] A. Grzybowski, K. Koperwas, A. Swiety-Pospiech, K. Grzybowska, and M. Paluch *Phys. Rev. B*, vol. 87, p. 054105, 2013.

[23] H. Groothues, F. Kremer, D. M. Collard, and C. P. Lillya *Liquid Crystals*, vol. 18, p. 117, 1995.

[24] M. M. Elmahdy, G. Floudas, M. Mondeshki, H. W. Spiess, X. Dou, and K. Mllen *Phys. Rev. Lett.*, vol. 100, p. 107801, 2008.

[25] N. Haase, C. Grigoriadis, H. Butt, K. Müllen, and G. Floudas *J. Phys. Chem. B*, vol. 115, p. 5807, 2011.

[26] K. L. Ngai, P. Lunkenheimer, C. León, U. Schneider, R. Brand, and A. Loidl *J. Chem. Phys.*, vol. 115, p. 1405, 2001.

Chapter 7

SUPPRESSION OF HYDROGEN-BOND-INDUCED CLUSTERS IN m-FLUOROANILINE BY MIXING WITH m-XYLENE

7.1 Introduction

Though halogen interactions are usually thought as weak, so that their effect is mainly neglected in the structural studies of liquids, there are remarkable exceptions such as water, alcohols or amines, where molecular self-association via H-bonding is known to occur. In these simple molecular liquids self-association was demonstrated by X-ray and neutron scattering

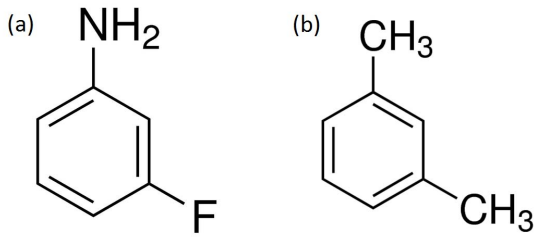

Figure 7.1: Molecular structure of m-fluoroaniline (a) and m-xylene (b).

experiments and Monte Carlo numerical simulations [1]. These studies revealed the presence of a pre-peak in the static structure factor measured in scattering experiments and of a shoulder to the main diffraction peak [1, 2], which are evidences for the existence of H-bonded clusters.

In some compounds the directional H-bond interactions of hydroxyl or amine groups compete with the repulsion between these polar groups and the hydrophobic (aliphatic or aromatic) bulky parts of the molecules, like for instance in m-fluoroaniline [mFA, $FC_6H_4NH_2$, see Figure 7.1(a)] [1, 2]. In these materials, a segregation at the molecular scale occurs, leading to a spatial organization of the molecules into clusters displaying supra-molecular order.

In the case of m-toluidine and m-fluoroaniline, neutron scattering experiments revealed a peak at 0.5 Å^{-1} in the static structure factor S(Q) (corresponding to large distances) [1, 2], which is taken as evidence of the spontaneous formation, in the supercooled liquid state, of supramolecular clusters induced by hydrogen bonding. These clusters are centred about amine groups, with the aromatic rings of the involved molecules pointing away from the H-bonds. Due to the steric hindrance of aromatic rings, the clusters are of limited size: the typical length scale, as determined experimentally, is about 12 Å between adjacent clusters, which corresponds to

clusters of no more than 10 molecular units [1, 2]. The hydrophobic core of the molecules excludes the build-up of an extended H-bond network such as that of water or other associating systems.

Apart from the primary structural relaxation, the dielectric loss spectra of mFA display a well-resolved secondary relaxation at higher frequency. In the past this secondary relaxation, visible at ambient pressure, was identified as the universal Johari-Goldstein (JG) β-relaxation [3]. However, dielectric studies carried out on mFA at moderate [4] and high [5] pressure showed significant pressure-induced changes in the dielectric spectra: in glasses obtained at very high pressure and high temperature the secondary relaxation observed at ambient pressure is suppressed, and a new secondary relaxation emerges with properties of a genuine JG relaxation like that of the van-der-Waals aromatic system toluene [5]. These results suggest that the secondary relaxation observed in mFA at ambient pressure is not a JG process, and could actually originate from some internal processes in the H-bond induced clusters.

The short-range order of structural glasses formed by mFA was shown to be different if the vitrification of mFA is obtained at low temperature and low pressure or at high temperature and high pressure [6]. Detailed structural information and comparison of glasses obtained under different conditions (isobaric cooling or isothermal compression) should be particularly useful to identify a possible effect of self-association on the relaxation dynamics of supercooled mFA. For example, the H-bonded clusters could interfere with the dynamical heterogeneities that are believed to be responsible for the dramatic dynamic slow-down taking place close to the glass transition [7]. This effect could explain the quite high glass transition temperature and high fragility of mFA.

The aim of this chapter is to investigate the presence of H-bond induced

clusters in mixtures of m-fluoroaniline with m-xylene [mX, $C_6H_4(CH_3)_2$, see Figure 7.1(b)], a similar aromatic compound which however possesses no H-bonding groups. The ultimate goal is to probe the microscopic mechanism behind the clustering phenomenon and the length scale associated with such clusters in a system where it is possible to suppress in a controlled way the H-bonded clusters by dilution of the H-bond density via addition of mX.

7.2 Experimental methods

mFA and mX where purchased from Aldrich Chemical Company with a purity of 99%. Both materials are liquid at room temperature, and the mixed $mFA_{1-x}mX_x$ samples were prepared by simply mixing the correspondent amount of the two materials with $0.25 \leq x \leq 0.95$.

Differential Scanning Calorimetry (DSC, see section 3.1.1) was carried out on all mixed samples in the temperature range between 273.15 K and 123.15 K, with a heating/cooling rate of 2 K per minute. High-resolution X-ray powder diffraction profiles (section 3.1.3) were recorded on some samples after quenching to 120 K, at various temperature with an acquisition times of 2 hours for each temperature.

Fourier-transform infrared spectroscopy (FTIR, see section 3.1.4) was performed at room temperature in the region of the NH stretching bands ($\lambda = 3150 - 3600$ cm^{-1}).

The frequency and temperature dependence of the complex dielectric permittivity was measured by means of broadband dielectric spectroscopy (see section 3.2.1). The measurements were performed using both the Novocontrol Alpha analyser (10^{-2} to 10^7 Hz) and the HP4291 impedance analyser (10^6 to 10^9 Hz). The temperature interval of the measurements

was between 114 K and 253 K with ±0.1 K stability. The samples were located in liquid form into a parallel-plate stainless steel capacitor with the electrodes separated by 50 μm thick silica spacers. Experiments on high mX molar fractions were carried out both in the Barcelona and Pisa laboratories.

7.3 Preliminary characterization

The thermal behaviour of the samples, as determined by DSC measurements, is shown in Figure 7.2 and Figure 7.3. The same DSC experimental procedure was applied for all concentrations under investigation: the sample was first cooled down from 273 to around 123 K at 2 K/min and then heated up to room temperature. The DSC thermograms upon heating are shown for two representative concentrations in Figure 7.2. The samples behaved differently according to their molar composition x: for $x < 0.75$, only the characteristic feature of the glass transition is visible upon heating. In the case of molar composition $x \geq 0.75$, during the heating above T_g also the recrystallization and melting are observed. In this second range of molar concentration, the glass transition can be observed by DSC only in the case of $x = 0.75$, because for higher mX content the glass transition occurs at lower temperature, outside the measuring range of the DSC instrument (see the BDS data in section 7.4 and the thermal evolution of T_g in Figure 7.3). The temperature values obtained from DSC measurements for all concentrations are summarized in Table 7.1.

To experimentally investigate the occurrence of aggregation, we acquired the infrared spectra of all studied concentrations. The measured FTIR spectra are shown in Figure 7.4. It may be observed that the

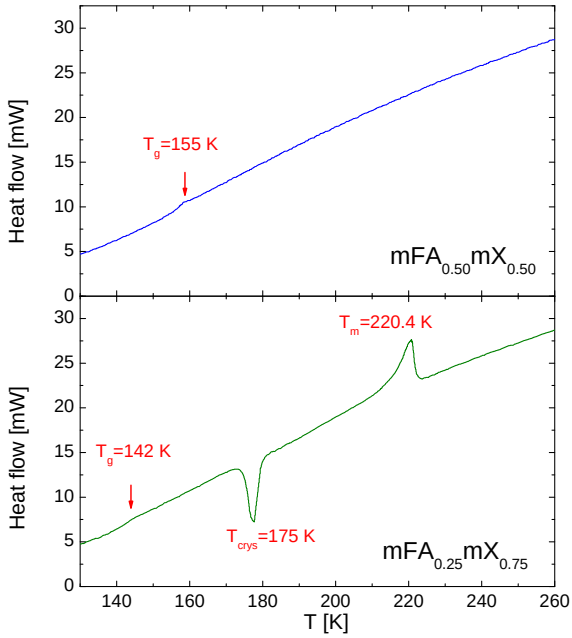

Figure 7.2: DSC thermograms of the $mFA_{1-x}mX_x$ binary mixtures with $x = 0.50$ (upper panel) and $x = 0.75$ (lower panel). Both thermograms are taken heating the sample in the temperature range between 123.15 K and 273.15 K with a heating rate of 2K/min.

N-H stretching modes (both the symmetric and the asymmetric one) are considerably modified at high mX molar fraction (*i.e.*, in correspondence with a strong reduction of the aggregate population). In particular, while in pure mFA two different FTIR bands are observed for each (symmetric and asymmetric) stretching mode, corresponding to aggregated and non-aggregated mFA molecules, the component due to the H-bond induced clusters decreases much more rapidly than the other one with increasing mX content. This is similar to what is reported for alkane solutions in *tert*-butanol, where concentration-dependent aggregation also occurs [8]. At the moment we are performing simulations to check what kind of aggregate the mFA tends to form.

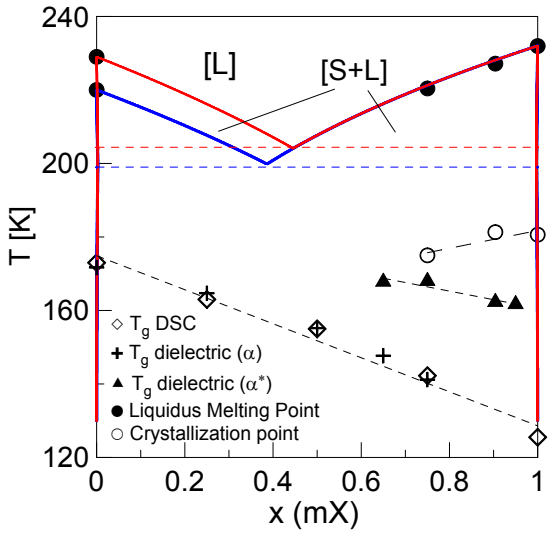

Figure 7.3: Phase diagram of the $mFA_{1-x}mX_x$ binary mixtures. The red line corresponds to the calculated liquidus (by means of the Schröder-Van Laar equation) assuming the melting temperature of mFA reported in [9] and the blue line assuming the melting temperature of Ref. [10]. Diamonds correspond to the T_g obtained from the DSC thermograms; the T_g values for the pure compounds are those of Ref. [10]. Crosses and triangles correspond to the T_g calculated from the dielectric measurements for the α and α^* processes respectively. The closed and open circles correspond, respectively, to the melting and crystallization temperatures, as obtained from the DSC thermograms. For values see Table 7.1.

x	T_m [K]	T_{crys} [K]	T_g DSC [K]	T_g diel. [K]
0.00	229 [9]		173 [10]	171.7
	220 [10]			
0.25			163	164.7
0.50			155	155.2
0.65				147.7
0.75	220.4	175	142.3	141.2
0.90	227.2	181.3		
1.00	232	180.6	125.5 [10]	

Table 7.1: Values of melting (T_m) and crystallization (T_{crys}) temperatures of the $mFA_{1-x}mX_x$ mixed samples, and of their glass temperature obtained from DSC (T_g DSC) and from dielectric spectroscopy (T_g diel.) measurements.

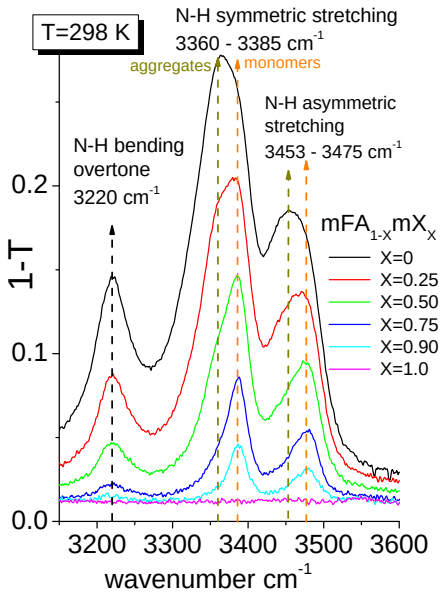

Figure 7.4: Infrared absorption spectra in the region of the N-H stretching bands for several binary mixtures of mFA with mX.

7.4 Dielectric Spectroscopy Study

Broadband dielectric spectroscopy measurements were carried out on the pure mFA compound and on all the binary mixtures under investigation (pure mX was not measured because it yields too weak a signal due to the small molecular dipole moment, and moreover it displays a strong tendency to crystallize). The measurements on the mixtures with $x \geq 0.65$ were done by quenching the sample down to 117 K to avoid crystallization (which was more likely to occur due to the higher concentration of mX), and the spectra were then taken every 2 K by heating the sample up to the corresponding melting point. The rest of the spectra ($x \leq 0.50$) were taken (again every 2 K) while cooling the sample to the lowest temperature reachable with our system (117 K). Figure 7.5 displays some of the loss spectra measured for three mX molar fractions ($x = 0.25$, 0.75 and 0.90) in the temperature range between 117 K and 237 K.

For mX molar fractions between 0 and 0.50 a primary (α) relaxation process is observed, followed by a secondary (β) relaxation at higher frequency (Figure 7.5(a)). Both display a smooth temperature dependence of the characteristic frequency and dielectric strength. Because the only polar molecule present in the system is mFA, both relaxations must involve the motion of mFA molecules. The α relaxation is the collective dynamic process associated with the glass transition of these homogeneous mixtures, as visible from the agreement of the T_g extrapolated from the α dynamics and the one obtained by DSC (Table 7.1). On the other hand, the position of the β process is approximately the same independently of the composition, and it matches the spectral position of the β relaxation in pure mFA. This entails that the origin of the β relaxation in the

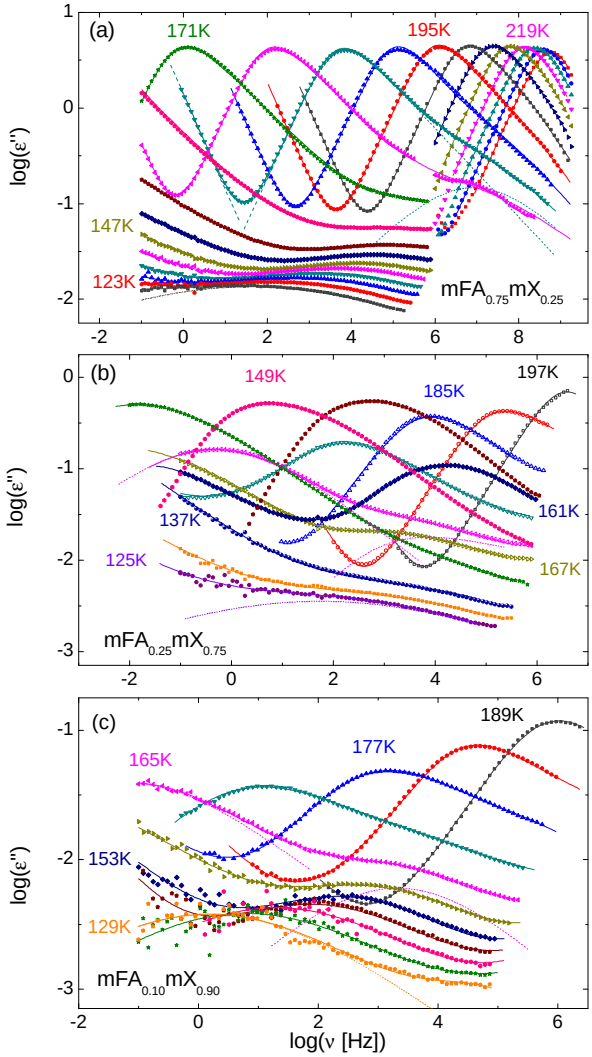

Figure 7.5: Dielectric loss spectra for the $mFA_{1-x}mX_x$ system for some of the molar fraction under investigation: (a) $x = 0.25$ in a temperature range between 237 and 177 K every 6 K; (b) $x = 0.75$ in a temperature range between 197 and 125 K every 6 K; (c) $x = 0.90$ with temperature between 189 and 129 K every 6 K. Solid lines correspond to fits and the dotted lines shown the different components used to fit the measured spectra at given temperatures (at 183 and 117 K in (a); at 163 and 125 K; at 165 and 129 K in (c)).

binary mixtures is the same as in pure mFA. The fact that the α process is sensitive to the relative concentration of mX while the β process is not, rules out a Johari-Goldstein interpretation, confirmed also by the fact that the coupling model (CM) does not apply to our data, as we checked by calculating the JG characteristic time from the α relaxation time. The origin of the secondary process was suggested to originate from some local dynamics inside H-bonded clusters [5]. For example, it could stem from the relative motion of two H-bonded molecules with respect to one another. Given that an H-bond links the NH_2 group (or possibly the F atom) of a mFA molecule with one of its neighbours, and since the molecular dipole moment of the mFA molecule is itself determined by the same polar groups, a relative rotation or swing motion of either molecule around the H bond might change the electronic distribution and thus the local dipole moments in a cluster. Another option is that mFA dimers are formed, and that the β process corresponds to some internal dynamics of such dimers.

The relaxation times of both dynamic processes are displayed as Arrhenius plots in Figure 7.6, for all three concentrations x between 0 and 0.5. The α process was fitted with an Havriliak-Negami (HN) profile (eq. 3.16) and the β process with a Cole-Cole function (eq. 3.9). The Arrhenius plot is useful to highlight the changes in the behaviour of the system as a function of the quantity of mX present in the mixture. The most important and prominent effect is the shift of the α relaxation to shorter times (*i.e.*, to a faster dynamics) with increasing mX concentration. This is a direct consequence of the reduction of H-bond density and thus of the size of the mFA clusters when mFA molecules are substituted with mX, as lower self-association (smaller clusters) implies faster collective dynamics. The primary relaxation has a non-simply activated behaviour,

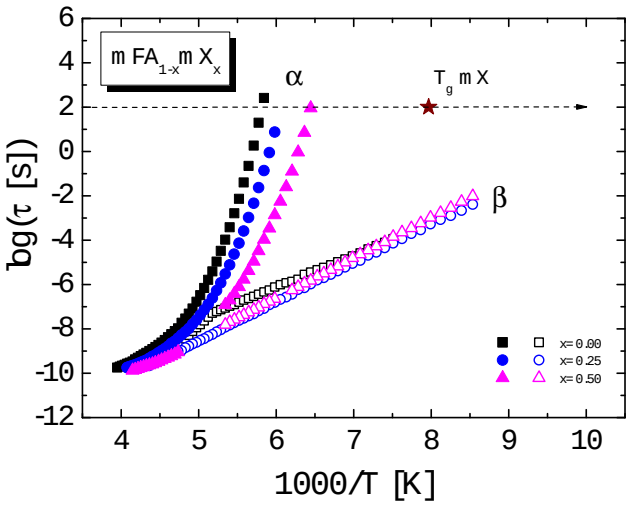

Figure 7.6: Relaxation times as a function of reciprocal temperature for the α (closed symbols) and β (open symbols) relaxations observed in the $mFA - mX$ binary system for mX molar fraction between 0 and 0.5. The star represents the glass transition temperature of pure mX [10].

while the β-relaxation times could be fitted simply with an Arrhenius law (Eq. 1.2), except for the high temperature data of pure mFA where a kink at 195 K is observed. This behaviour was already reported in previous studies on pure mFA [5, 11]. The fact that the α and β relaxation times converge together at high temperature is consistent with the interpretation of the β process, as when the temperature is increased the character of the α relaxation becomes less and less cooperative an thus more representative of the dynamics around a single H-bond than of an extended cluster.

For x equal to 0.65 and 0.75 (Figure 7.5(b)), one can follow the evolution of the α and β peaks with temperature only up to approximately 165 K. At this temperature the primary α relaxation starts to fade away and a new relaxation, which we will refer to as α^*, becomes visible

at higher frequencies (shorter times). Because the sample was initially quenched from the liquid phase, the spectra acquired at temperatures lower than 165 K are characteristic of a homogeneous mixture. However, further increase of the temperature provides sufficient thermal energy for the crystallization of a mX-rich part of the sample, as we observed in XRD measurements (see Figure 7.7 for comparison of XRD spectra between the mixture with x =0.75 at 120 and 180 K and the spectra for the pure crystalline mX at 4.5 K, retrieved from Ref. [12]). We conclude therefore that for $x \geq$0.65 a phase separation of the sample takes place, namely, into a mX-rich crystalline phase and a mFA-rich amorphous phase, that leads to the suppression of the α peak of the homogeneous mixture. Such phase separation can occur for example, if the two materials are not completely miscible at high mX content: in such case two phases with different mX concentration would coexist. It should be noted that the α^* relaxation is close, in terms of the relaxation times (and also in terms of its temperature dependence, see below), to the α relaxation of pure mFA. This entails that the α^* relaxation is the spectral signature of mFA clusters present in the mFA-rich phase.

It is clear from Figure 7.5 that the width of the α and α^* peaks increases with decreasing temperature. This is expected since the α and α^* processes become more cooperative at lower temperature, resulting in a wider distribution of relaxation times.

In the 0.75 molar fraction case, at the same time that the α^* relaxation appears in the spectrum, the β process vanishes and a new secondary relaxation (β') is observed at longer relaxation times. The β' and α^* relaxations are the only ones visible if the sample is cooled down again.

By further increasing the mX molar fraction ($x = 0.90 - 0.95$) only the α^* peak and the β' relaxation are observed at all temperatures

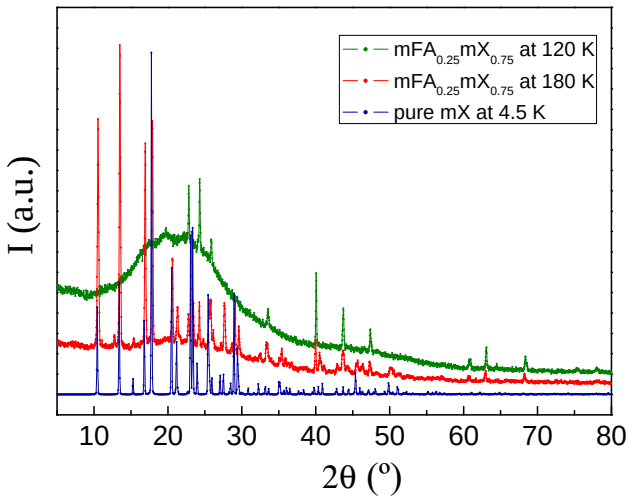

Figure 7.7: Experimental diffraction patterns of the $mFA_{0.25}mX_{0.75}$ binary system after the quench to 120 K (green) and the subsequent heating to 180 K (red). The patterns are compared with the diffraction pattern of pure crystalline mX at 4.5 K (blue), retrieved from Ref. [12].

(Figure 7.5(c)). The absence of the α peak indicates that the our quench rate is not sufficient to avoid the mX crystallization, so that the primary relaxation of the homogeneous supercooled liquid is not visible, but only the α^* peak corresponding to the mFA-rich regions.

The β' relaxation, present at x larger than 0.75, is significantly slower than the β relaxation observed for lower mX molar fraction (including pure mFA), although both have very similar activation energies. The slower dynamics of the β' process can be rationalized if this relaxation is characteristic of mFA molecules trapped inside the mX-rich crystalline phase, because crystallization leads to a slowing-down of all dynamics. Since the β and β' processes have virtually identical activation energies, they likely stem from the same local dynamic process; the β' process

might therefore be the spectral signature of the secondary relaxation of local H-bond-related motions of mFA molecules trapped inside the mX-rich crystalline phase or of $mFA - mX$ dimers. The very low dielectric strength of this process (see Figure 7.8) indeed indicates that relatively few molecules contribute to it.

In Figure 7.8 it is possible to observe the spectral changes as a function of x at two fixed temperatures (171 K and 143 K). At 171 K (upper panel) both the primary α relaxation and the secondary β relaxation are initially observed. Increasing the mX concentration the intensity of both peaks decreases to zero, and the new α^* and β' relaxations appear, which are both consequence of the crystallization of the mX component. Above $x = 0.75$, only the α^* and β' relaxations are visible. At 143 K (lower panel) mainly the β relaxation is visible in our experimental frequency range. It may be observed that for x below 0.75 the frequency of the β process is almost independent of the fraction of mX in the system.

The relaxation times of the α, α^*, β and β' relaxations are plotted as a function of temperature in Figure 7.9 (Arrhenius plot) for all the mX molar fractions under examination. All primary (α, α^*) peaks could be fitted using a HN line shape, while both secondary (β and β') relaxations were fitted using a Cole-Cole function. The fit parameters are summarized in Table 7.2. It can be observed in Figure 7.9 that the characteristic time of the α^* process (observed for average molar fractions x between 0.65 and 0.95) matches that of the α relaxation for x between 0 and 0.50, which confirms the formation of mFA-rich domains with clusters similar to those of homogeneous mixtures with low mX content.

The α-relaxation time for the mixtures with x between 0 and 0.50 cannot be fitted satisfactory using the VFT equation (Eq. 1.3), and we therefore employed instead the Cohen-Grest equation (Eq. 1.7); in all the

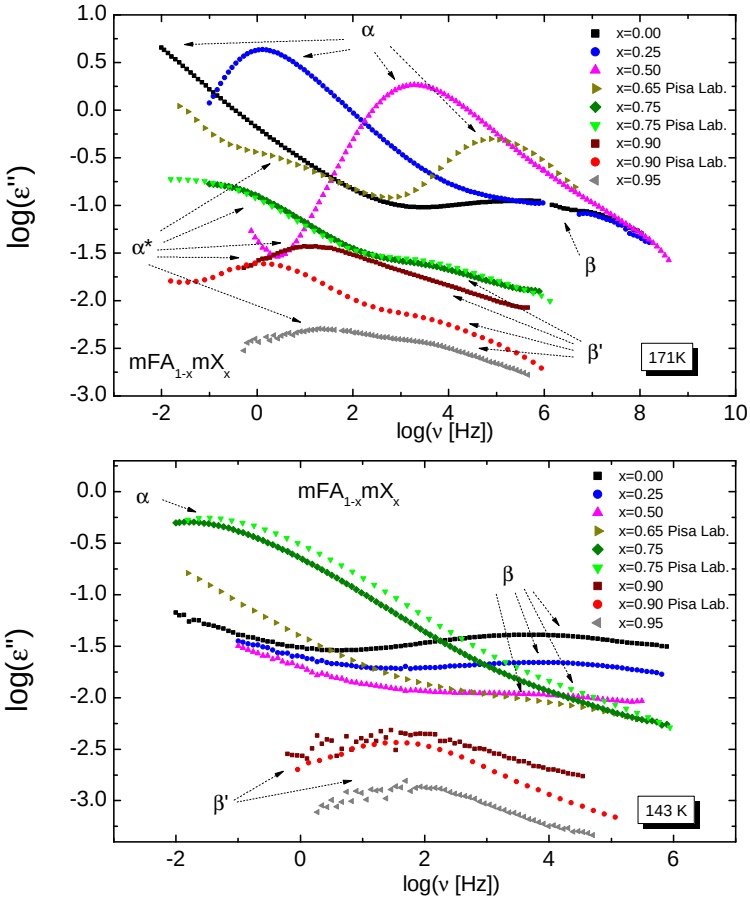

Figure 7.8: Comparison of the dielectric loss spectra at 171 K (upper panel) and 143 K (lower panel) for the different mX molar fractions.

x	α relaxation			α^* relaxation			β relaxation		β' relaxation	
	$\Delta\epsilon$	α_{HN}	β_{HN}	$\Delta\epsilon$	α_{HN}	β_{HN}	$\Delta\epsilon$	α_{CC}	$\Delta\epsilon$	α_{CC}
0	12.2-25.0	0.96-1.00	0.43-1.00	-	-	-	0.35-2.08	0.24-0.39		
0.25	7.7-14.1	0.93-1.00	0.42-1.00	-	-	-	0.18-1.85	0.19- 1.00		
0.50	4.7-7.4	0.67-1.00	0.42-0.81	-	-	-	0.15-0.65	0.31-0.89		
0.65 (Pisa)	4.0-4.5	0.59-0.89	0.42-0.69	2.2-3.5	0.69-0.96	0.42-0.61	0.07-0.11	0.19-0.27		
0.75	2.2-2.6	0.57-0.88	0.31-0.71	0.8-1.8	0.43-0.92	0.34-0.72	0.03-0.07	0.21-0.29	0.19-0.28	0.33-0.40
0.75 (Pisa)	2.7-3.1	0.42-0.84	0.43-0.72	0.8-2.8	0.39-0.96	0.24-0.93	0.04-0.06	0.23-0.29	0.12-0.14	0.34-0.39
0.90	-	-	-	0.2-0.3	0.40-0.78	0.60-0.78			0.03-0.04	0.33-0.44
0.90 (Pisa)	-	-	-	0.1-0.2	0.40-0.72	0.61-1.00			0.01-0.02	0.38-0.52
0.95	-	-	-	0.03-0.05	0.32-0.56	0.62-0.92			0.007-0.011	0.38-0.47

Table 7.2: Left column: Values of the fit parameters (strength $\Delta\epsilon$ and exponents α_{HN} and β_{HN}) for the α and α^* relaxations, as obtained from the Havriliak-Negami function fits for all x molar fractions. Central and right column: fit parameters (strength $\Delta\epsilon$ and exponent α_{CC}) for the β relaxation obtained from The Cole-Cole function fits for all x molar fractions.

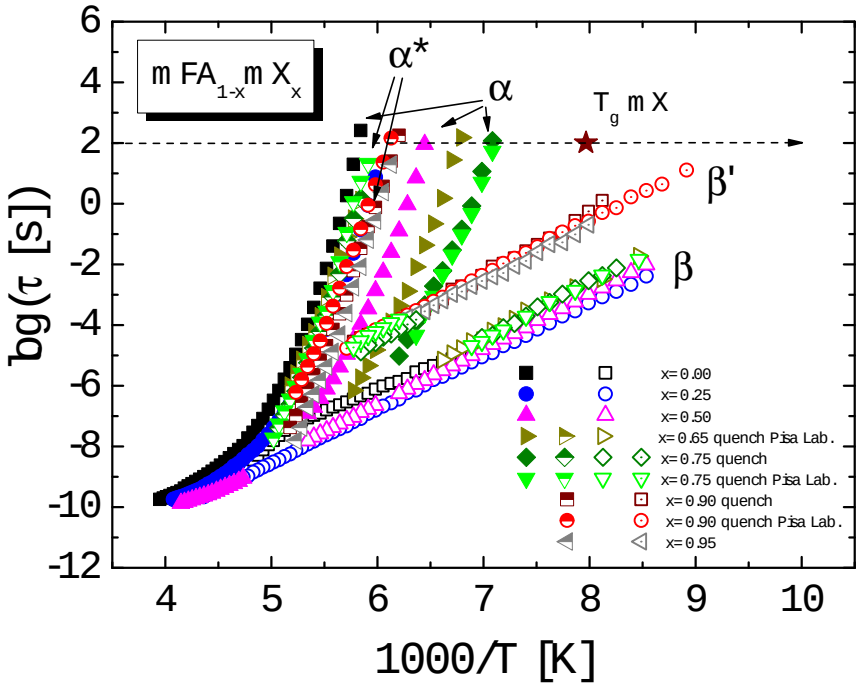

Figure 7.9: Relaxation times as a function of reciprocal temperature for the α (closed symbols), α^* (half-closed symbols), β (open symbols) and β' (circled dot symbols) relaxations observed in the $mFA - mX$ binary system. The star represents the glass transition temperature of pure mX [10].

other cases the VFT gave a good fit. The values of T_g extrapolated from these fits for the α and α^* relaxations, together with the corresponding fragility value m (calculated according to Eq. 1.4) are summarized in Table 7.3. The high fragility of pure mFA and of the homogeneous mixtures indicates that all of them are fragile glass formers. The fragility decreases slightly with increasing mX content, which means that the dynamic correlation decreases by adding mX. This experimental result can be associated with the lower number of hydrogen bonds and the smaller size of the H-bonded clusters upon higher mX content.

x	$T_g(\alpha)$ [K]	$T_g(\alpha^*)$ [K]	m (α)	m (α^*)	$E_a(\beta)$ [K]	$E_a(\beta')$ [K]
0	171.7 ± 0.4		86.9 ± 1.0		3304 ± 12	
0.25	164.7 ± 0.2		79.4 ± 1.1		4036 ± 7	
0.50	155.2 ± 0.8		80.3 ± 1.3		4179 ± 5	
0.65 (Pisa)	147.7 ± 0.2	167.8 ± 0.5	78.1 ± 3.2	84.0 ± 1.8	4188 ± 89	
0.75	141.2 ± 0.4	168.0 ± 0.2	74.6 ± 1.8	95.6 ± 2.4	4313 ± 81	4450 ± 92
0.75 (Pisa)	140.5 ± 0.9	168.4 ± 0.3	72.0 ± 1.4	89.3 ± 1.7	4273 ± 81	4467 ± 115
0.90		162.3 ± 0.4		81.1 ± 1.5		4481 ± 59
0.90 (Pisa)		163.8 ± 0.4		80.1 ± 1.0		4187 ± 16
0.95		161.7 ± 0.4		80.6 ± 1.1		4074 ± 41

Table 7.3: Values of the glass temperature (T_g) and fragility m for the α and α^* relaxations and values of the activation energy (E_a) associated to the β and β' relaxations for the $mFA_{1-x}mX_x$ binary system as extrapolated from the fits of the relaxation times as function of the inverse of temperature.

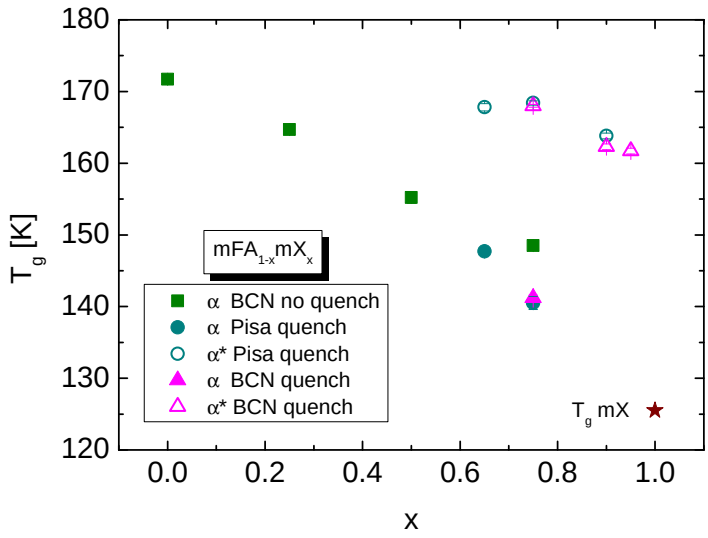

Figure 7.10: Glass temperature T_g for the α (closed symbols) and α^* (open symbols) relaxations. Vertical lines represent the associated error bars.

It may be observed from Figure 7.10 that the glass transition temperature associated with the α relaxation decreases with increasing mX molar fraction and that it approaches the T_g of pure mX (star in Figure 7.9 and Figure 7.10) as the mX concentration tends to unity. Instead, the α^* process displays a T_g similar to that of mFA-rich homogeneous mixtures with x between 0.1 and 0.3. This confirms the idea that, above a certain temperature, the part of the compound rich in mFA is the one responsible for the observed α^* relaxation while the part rich in mX crystallizes (as seen by X-ray diffraction patterns).

By decreasing the quantity of mFA in the sample, the strengths of both α and α^* peaks decrease. Both strengths show non-linear dependence on x (see Figure 7.11). Since $\Delta\epsilon = (N/V)\mu^2/kT$ and α and α^* are collective processes, their dielectric strength is proportional to the

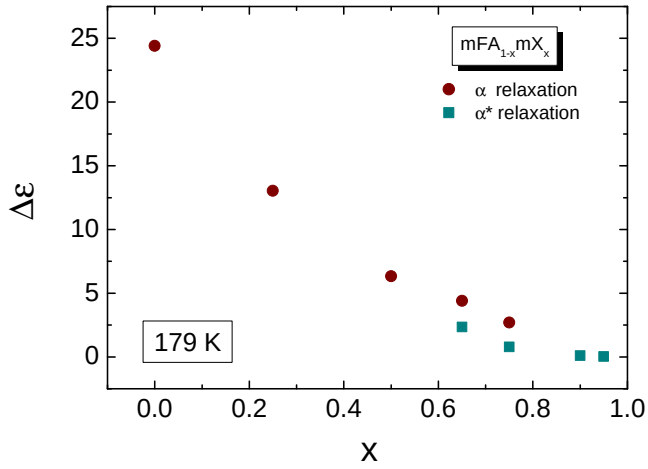

Figure 7.11: Strength of the α (circles) and α^* (squares) relaxations as a function of the mX molar fraction at the fixed temperature of 179 K.

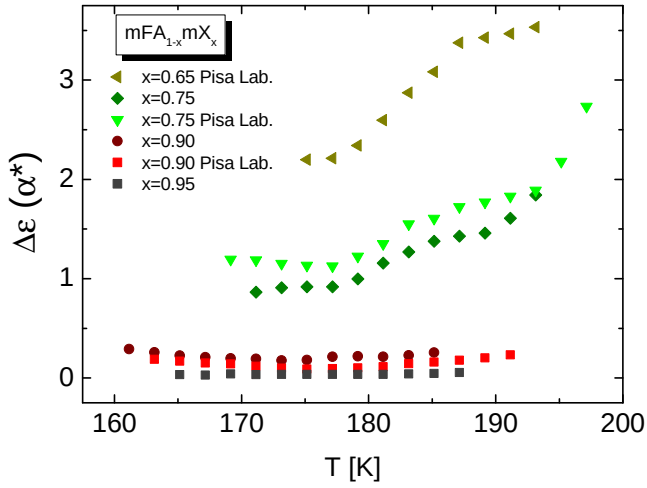

Figure 7.12: Strength of the α^* peaks as a function of temperature, as resulting from the HN fits of the loss spectra for the x concentrations between 0.65 and 0.95.

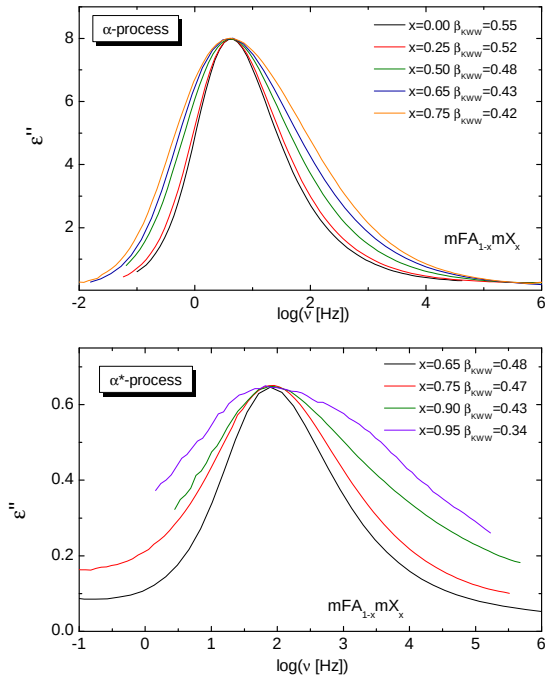

Figure 7.13: Loss spectra measured at the indicated mX molar fraction at different temperatures so as to observe the main relaxation peak at the same frequency f_{max}, namely with $logf_{max} = 0.6$ in the case of the α process (upper panel) and with $logf_{max} = 1.9$ in the case of the α^* process (lower panel).

number density of mFA molecules that belong to H-bonded clusters. The decrease of the strength of the α process for $x < 0.65$ is due to the lower concentration of mFA in the homogeneous mixture phase. Similarly, the decrease of the α^* strength for $x \geq 0.75$ is indicative of the lower amount of mFA-rich domains. The fact that the increase of the strength with increasing mFA content is non-linear for both α and α^* processes could be due to the fact that at low mFA concentrations not all mFA molecules are able to join a cluster (as they are trapped in the mX matrix).

Figure 7.12 exhibits the variation of the strength of the α^* process

as a function of temperature for mX molar fraction between 0.65 and 0.95; the strength increases with temperature, perhaps due to the higher mobility of the mFA molecules.

Figure 7.13 is a plot of the intensity-normalized dielectric loss spectra of different mixtures, acquired each at a different temperature chosen so as to maintain roughly the same value of the relaxation time for the α process at the isochronal value $logf_{max_\alpha} = 0.6$ (corresponding to ca. 39 ms, upper panel) and for the α^* process at the isochronal value $logf_{max_{\alpha^*}} = 1.9$ (corresponding to ca. 2 ms, lower panel). From these superposition graphs it can be gathered that the width of both peaks increases with increasing mX molar fraction (β_{KWW} decreases). This indicates a wider variety of distribution times of the primary relaxation with increasing mX content, which stems from a larger variety of molecular environments of the mFA molecules in the clusters. This is consistent with clusters of smaller size, for which cluster-surface effects are more important.

7.5 Conclusions

In this chapter we investigated the extent of H-bond induced clusters in mixtures of m-fluoroaniline (mFA) with m-xylene (mX), a similar aromatic compound which however possesses no H-bonding groups. The increase of the mX molar fraction results in a shorter relaxation time (faster dynamics) of the collective α relaxation of the mixture, indicating weaker intermolecular interactions and the reduction of the size of the mFA clusters contributing to the relaxation process. Also the fact that the fragility, and therefore the dynamic correlation, decrease slightly with increasing mX content is associated with a lower number of hydrogen bonds. The presence of two secondary processes (β and β'), one at longer

relaxation time compared to the other and with almost the same activation energy, suggests that their microscopic origin is the same and is related to local dynamics involving the hydrogen bonds formed by mFA molecules.

Bibliography

[1] D. Morineau and C. Alba-Simionesco *J. Chem. Phys.*, vol. 109, p. 8494, 1998.

[2] D. Morineau, C. Alba-Simionesco, M. C. Bellisent-Funel, and M. F. Lauthie *Europhys. Lett.*, vol. 43, p. 195, 1998.

[3] A. Kudlik, S. Benkhof, T. Blochowicz, C. Tschirwitz, and E. Rössler *J. Mol. Struct.*, vol. 479, p. 201, 1999.

[4] A. Reiser, G. Kasper, and S. Hunklinger *Phys. Rev. Lett.*, vol. 92, p. 125701, 2004.

[5] S. Hensel-Bielowka, M. Paluch, and K. L. Ngai *J. Chem. Phys.*, vol. 123, p. 014502, 2005.

[6] C. Alba-Simionesco, D. Morineau, B. Frick, N. Higonen, and H. Fujimori *J. Non-Cryst. Solids*, vol. 235-237, p. 367, 1998.

[7] C. Dalle-Ferrier, C. Thibierge, C. Alba-Simionesco, L. Berthier, G. Biroli, J.-P. Bouchaud, F. Ladieu, D. L. Hôte, and G. Tarjus *Phys. Rev. E*, vol. 76, p. 041510, 2007.

[8] P. Sassi, F. Palombo, R. S. Cataliotti, M. Paolantoni, and A. Morresi *J. Phys. Chem. A*, vol. 111, p. 6020, 2007.

[9] G. Kasper and A. Reiser *J. Non-Cryst. Solids*, vol. 352, p. 4900, 2006.

[10] C. Alba-Simionesco, J. Fan, and C. A. Angell *J. Chem. Phys.*, vol. 110(11), p. 5262, 1999.

[11] T. Fujima, H. Frusawa, and K. Ito *Phys. Rev. E*, vol. 66, p. 031503, 2002.

[12] R. M. Ibberson, W. I. F. David, S. Parsons, M. Prager, and K. Shankland *J. Mol. Struct.*, vol. 524, p. 121, 2000.

Chapter 8

DYNAMICS OF TERNIDAZOLE AS A FUNCTION OF TEMPERATURE AND PRESSURE

8.1 Introduction

Amorphous solids and glasses display only short-range order, unlike crystalline materials characterized by long-range order of molecular packing. For the pharmaceutical industry, the relevance of glasses is twofold: in addition to their very common occurrence (they are obtained directly from the synthesis processes) glasses displays higher solubility than the crystalline form (or polymorphs) of the same compound. Despite these advantages, the glass state has the drawback that it is physically unstable

against crystallization, and that such in stability is currently uncontrolled. The issue of the stability of pharmaceutical glasses is particularly complex, partly due to the fact the pharmaceutical compounds are organic materials that usually exhibit hydrogen bond networks or hygroscopicity resulting in humidity-dependent properties, and partly due to their conformational richness, not encountered in inorganic glasses.

It is nowadays commonly accepted in fact that one of the causes behind the glass formation is the conformational wealth inherent to flexible molecules, which is also perceived as an essential feature for the existence of distinct polymorphs in the crystalline state [1]. The crucial role of conformers for glass formation is attributed to the slow kinetics of conformational transformation of the molecules into the suitable conformer for a given polymorph obtained upon crystallization from the melt or from a solutions. This can happen if because the conformer that minimizes the crystal energy corresponds to a high-energy state in the melt or has a low relative concentration in solution.

Part of the pharmaceutical research is devoted to improve the physical and chemical stability of active principles. This can be achieved in different ways: by the prodrug strategy, which is a modification of the physico-chemical properties via chemical derivatization; by formation of co-crystals by mixing components that are solid at room temperature, one of which is an active pharmaceutical ingredient [2]; by salification, in which the active pharmaceutical ingredient is transformed into a nitrate, hydrochloric or other salt; or by amorphization of the active compound. In the last process, poor glass formers are submitted to a deliberate process that prevents crystallization from the melt or else to a non conventional treatment to reach the amorphous state, such as freeze-drying, spray-drying, milling, rapid precipitation by antisolvent addition, introduction of impurities,

and dehydration of hydrate forms [3], among others.

Once obtained, the glass state is in general unstable against the so-called recrystallization process, which consists in the nucleation of crystalline domains in the glass phase and in their subsequent growth. As the temperature is lowered below the melting point, the Gibbs energy difference between the supercooled liquid and the crystal polymorph increases, resulting in a thermodynamic drive that favours the crystallization process. On the other hand, the increase of viscosity (*i.e.* decrease of molecular mobility) in the supercooled liquid works against nucleation and, if nuclei are formed, against the growth of the crystalline phase. The antagonistic role played by the thermodynamic gradient on one hand and the slow kinetics on the other, is the main difficulty to understand and model the crystallization process. In the past, studies of the recrystallization of supercooled liquids were conducted by varying exclusively the temperature, whereas the second variable determining the thermodynamics of the system, *i.e.* the pressure, was mainly disregarded due to the inherent experimental difficulties, except for a few non-conclusive studies on inorganic systems [4–6].

In order to link the nucleation and growth rates to the thermodynamic drive, both temperature and pressure should be parametrized. Recently, Paluch and co-workers have proposed a strategy referred to as the "isochronal condition" method in which the molecular mobility is maintained constant for a set of (T,P) thermodynamic states while the crystallization process develops. The method is based on determining the relaxation map (*i.e.* the viscosity) of the liquid and supercooled liquid as a function of temperature (T) and pressure (P). For a given relaxation time (viscosity) a set of states defined by different value of the two variables T and P is selected, within which the viscosity is invariant, hence keeping constant

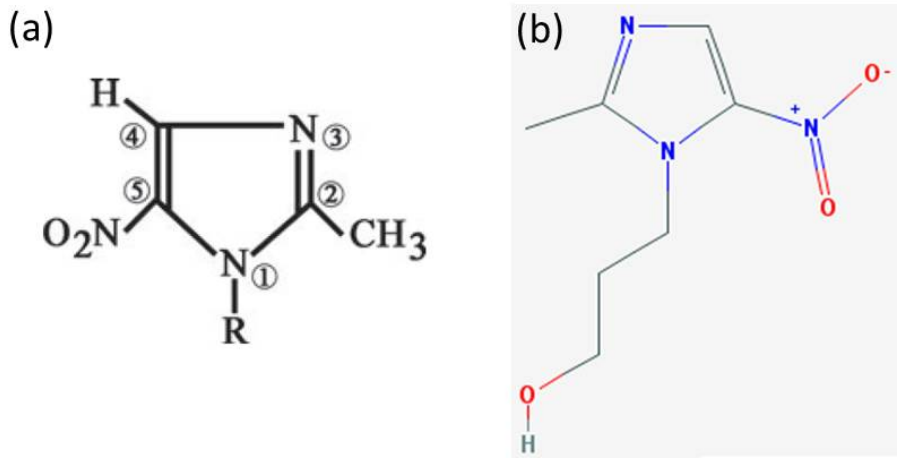

Figure 8.1: (a) Chemical structure of the 2-methyl-5-nitroimidazole derivatives and (b) of ternidazole with R=$CH_2CH_2CH_2OH$ [11].

the molecular mobility (kinetics) and probing exclusively the influence of the thermodynamic gradient on the crystallization process. The crystallization of several organic materials has been investigated using this idea. For 5-methyl-2-[(2-nitrophenyl)amino]-3-thiophenecarbonitrile [7], indomethacin [8] and dimethyl phthalate [9], for example, it has been concluded that a higher pressure (for isochronal measurements) speeds up the crystallization process, whereas for ibuprofen [10] the opposite effect was observed, namely a decrease of the crystallization rate with increasing pressure.

The aim of the present work is to obtain information about the effect of pressure on the dynamics of supercooled ternidazole drug (3-(2-methyl-5-nitroimidazol-1-yl)-propan-1-ol, $C_7H_{11}N_3O_3$, hereinafter TDZ) by means of broadband dielectric spectroscopy, to study the kinetics of the recrystallization process at high pressure as well as to disentangle the effect, if any, of the existence of two conformers.

8.2 Structural characterization

Ternidazole is an imidazole derivative with antiprotozoic and antibiotic properties [12, 13]. The general molecular structure of inimidazole derivatives and of TDZ are schematically drawn in Figure 8.1. TDZ has been recently characterized from a crystallographic and thermodynamic points of view [11]. It crystallizes into a triclinic structure (with space group $P\bar{1}$) in which the asymmetric unit cell, with $Z' = 2$, is formed by two different conformers A and B, whose molecular structures are shown in Figure 8.2(a). The local molecular arrangement, shown in Figure 8.2(b), consists of four conformers (two of each type) arranged so as to form a tetramer held together by hydrogen bonds. The tetramers are stacked parallel to each other forming layers coinciding with the (200) plane and held together mainly by van der Waals forces (Figure 8.3). No polymorphism is reported for TDZ: the material crystallizes in the same triclinic structure regardless of its thermal history. The pressure-temperature phase diagram indicates that the triclinic phase is the most stable (equilibrium) solid phase for pressures up to 0.2 GPa [11]. The presence of two isomers in the asymmetric unit cell means that the crystal is formed by two distinct molecules which are not related by any symmetry operation; the occurrence of multiple molecules in the asymmetric unit is rather uncommon. Based on the Cambridge Structural Database, Bond *et al.* [14] concluded that the structures of organic materials displaying $Z' = 2$ represent around 10% of the total. For the particular case of imidazole derivatives, this percentage is approximately 13%.

Nitroimidazole compounds, a subset of imidazole derivatives, are quite simple, small and flexible molecules (in the case of TDZ, due to the n-propanol chain) which usually display weak intermolecular interactions

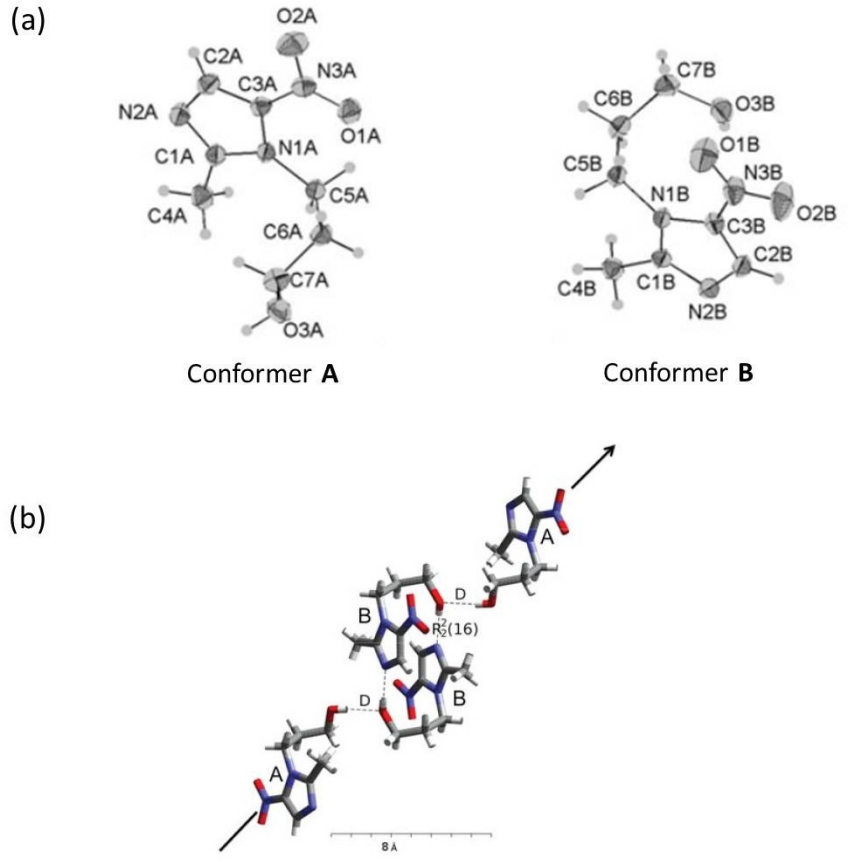

Figure 8.2: (a) Conformations of the two conformers of ternidazole (A and B) observed in the solid state. The anisotropic ellipsoids for 294 K are drawn at 30% probability level; hydrogen atoms are drawn as spheres with arbitrary radii [11]. (b) Local molecular arrangement in the triclinic phase of TDZ: two of each conformers (A and B) form a tetramer held together by hydrogen bonds (dotted lines).

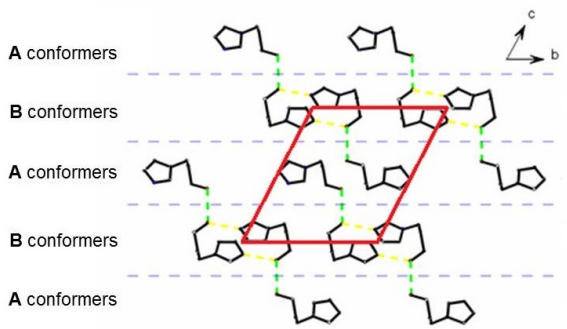

Figure 8.3: Layer structure of ternidazole [11]. The red parallelogram corresponds to a unit cell.

[15–17]. In the case of TDZ the main intermolecular interactions are the hydrogen bond between the OH group of a B conformer and either the same group of an A conformer or with the nitrogen atom involved in a double bond of a second B conformer (green and yellow dotted lines in Figure 8.2(b)) [11]. Since A and B conformers have a different environment, the intermolecular interactions between them are also different and the question arises if such differences can result in distinct dynamics in the supercooled state. Supercooling and glass formation of TDZ are easily achieved: at ambient pressure a glass transition is observed even by slow cooling of the melt (T_m = 333 K). Figure 8.4 displays a typical DSC curve (see section 3.1.1) measured at ambient pressure upon heating after the quench of the liquid phase down to 193 K. The glass transition is observed at T_g = 235 K [11]. Figure 8.5 represents the pressure and temperature dependence of T_m and T_g, as obtained by means of high-pressure differential thermal analysis (all these results are from Ref. [11]) and from dielectric measurements (carried out in this thesis), which will be discussed in section 8.4.

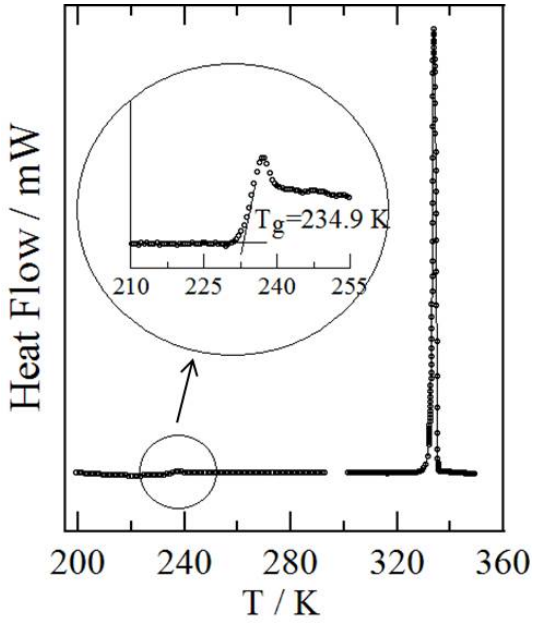

Figure 8.4: Differential scanning calorimetry (DSC) curve of ternidazole. The most prominent peak corresponds to the melting of ternidazole, measured upon heating the triclinic phase; the peak enlarged in the circle corresponds to the glass transition observed upon heating the glass state obtained by supercooling the liquid phase [11].

8.3 Experimental details

Medicinal grade ternidazole was provided by Bouchara-Recordati, Levallois Perret (France) and used as received.

PVT measurements (see section 3.1.2) on TDZ were carried out at 368.15, 356.15, 346.15, 325.15 and 303.15 K in a pressure range between 0.1 and 0.3 GPa.

Temperature-dependent broadband dielectric spectroscopy measurements at ambient pressure (see section 3.2.1) were performed using a capacitor filled with TNZ in the liquid state. The spectra were taken between 10^{-2} and $1.8 \cdot 10^{9}$ Hz in the temperature range between 203 K

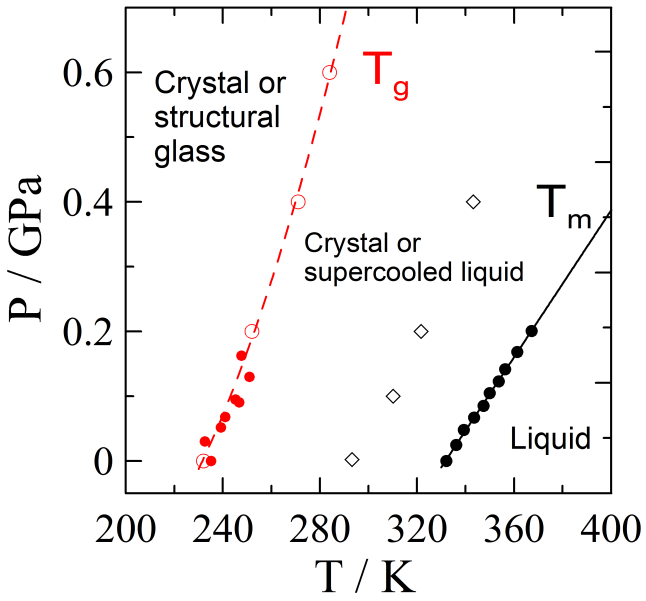

Figure 8.5: Pressure-temperature equilibrium and non-equilibrium phase diagram of ternidazole from high-pressure differential thermal analysis (full symbols, from [11]) and from dielectric spectroscopy measurements (empty symbols). Diamonds indicate the isochronal points at which the crystallization kinetics was studied (see text).

and 337 K every 2 K. Pressure-dependent dielectric measurements were carried out in the frequency range between 10^{-2} and 10^{7} Hz (see section 3.2.2). For the latter measurements the material was placed in its liquid state between two parallel stainless-steel plates; in order to prevent a possible contamination with the pressurizing fluid (thermal oil from Huber) the capacitor was covered by a teflon membrane and latex wrapping. The sample was placed in a high-pressure chamber (Unipress) made of a Cu-Be alloy, which was filled with the thermal oil and connected to a manual pump that allowed applying hydrostatic pressure between ambient pressure and 0.6 GPa, as measured by means of a pressure transducer

with an accuracy of ±0.5%. The temperature was controlled by thermal baths (Lauda Proline RP 1290 and Huber Unistat) with a liquid flow circuit connected to the high-pressure setup. Isothermal pressure scans were taken at 260, 280, 300 and 320 K, and isobaric measurements at 0.2, 0.4 and 0.6 GPa were performed in the temperature range between 210 K and 336 K.

8.4 Dielectric Spectroscopy Study

In order to probe the crystallization process at isochronal conditions, the dynamics of the system must be first determined as a function of both thermodynamic variables T and P. Figure 8.6 displays examples of dielectric loss spectra acquired on supercooled TDZ for a set of temperatures at ambient pressure (upper panel) and for a set of pressures at the constant temperature of 260 K (lower panel). It is clear at first glance that the α-relaxation process due to the collective rototranslational motions of the TDZ molecules is accompanied by two secondary relaxations (β and γ processes). The dielectric loss spectra were fitted as the sum of three components, namely a Cole-Davidson function for the primary relaxation and two Cole-Cole functions for each secondary process. The relaxation times of all three losses, as obtained from the fits, are plotted as a function of the reciprocal of temperature (Arrhenius plot) in Figure 8.7 at fixed pressure (ambient pressure and 0.4 GPa), and as a function of pressure in Figure 8.8, at the fixed temperature of 260 K. We first focus on the primary process; the origin of the secondary processes will be discussed later.

The relaxation times of the α process are plotted in Figure 8.9 as a function of temperature for different pressures (upper panel) and as a

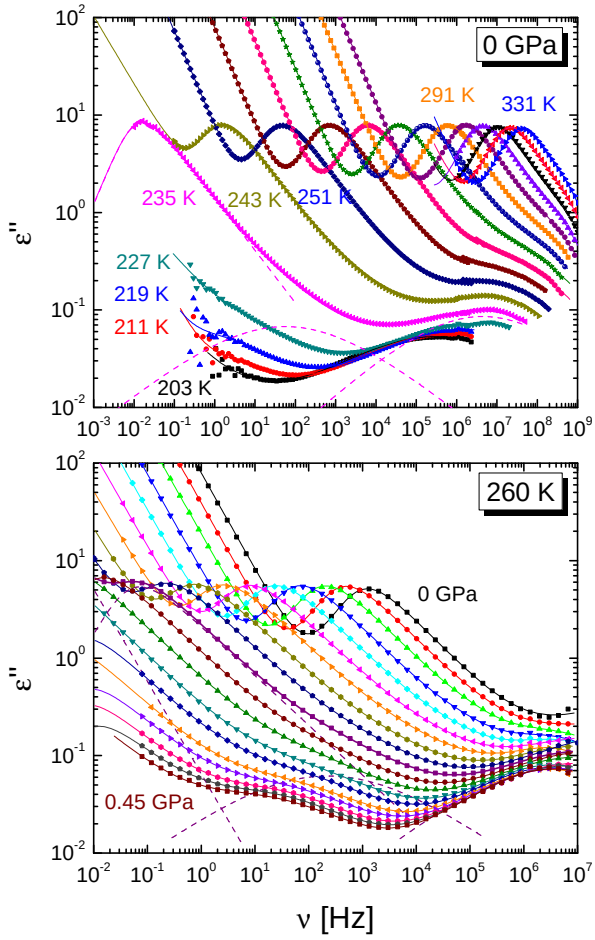

Figure 8.6: Upper panel: dielectric loss spectra of supercooled TDZ for several temperatures at normal pressure (markers) and corresponding fits (solid lines). The primary relaxation (described by the Cole-Davdison function) and the two secondary processes (described by the Cole-Cole functions) are shown for the spectrum acquired at 235 K as dashed lines. Lower panel: dielectric loss spectra of TDZ for pressures between normal pressure and 0.45 GPa every 25 MPa at the constant temperature of 260 K. Markers are experimental points and continuous lines are fits. Dashed lines represent the conductivity term and the three peak functions used to fit the data at 225 MPa.

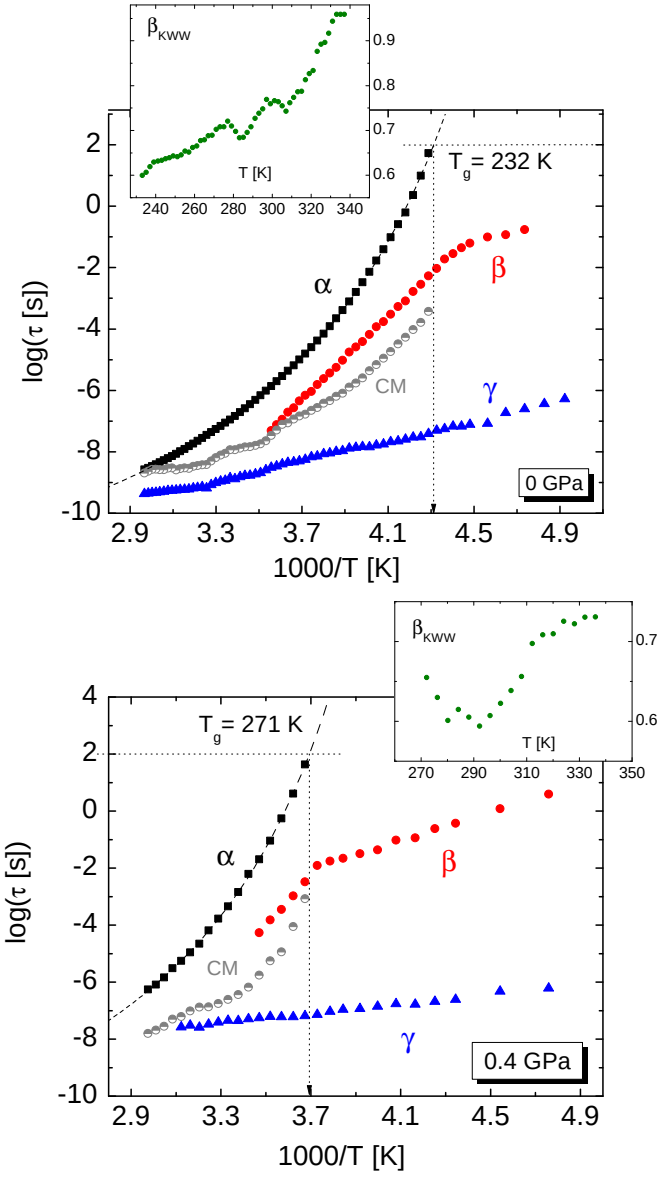

Figure 8.7: Arrhenius plot of the relaxation times for all three α, β, and γ dynamic processes, at ambient pressure (upper panel) and at 0.4 GPa (lower panel). The grey half-filled circles correspond to the theoretical Johari Goldstein relaxation times calculated according to the CM (see section 2.3.2). Insets: β_{KWW} stretched exponent as derived from the fit of the α peak, as a function of temperature.

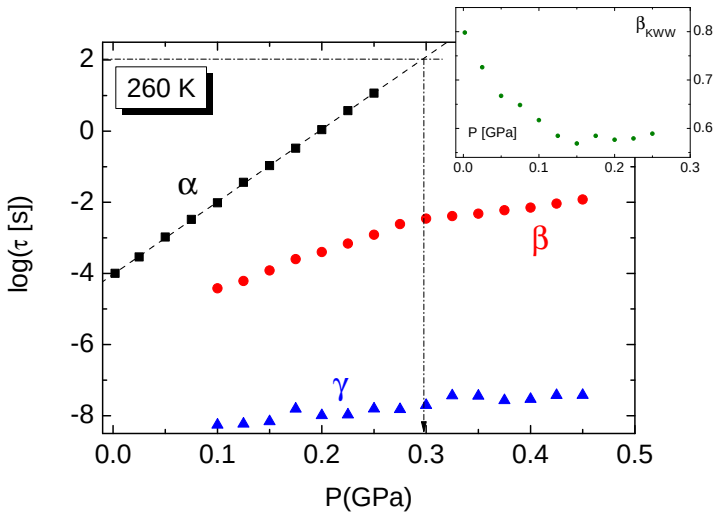

Figure 8.8: Plot of the relaxation times as function of the pressure for the different α, β, and γ processes at the temperature of 260 K. The grey half-filled circles corresponds to the theoretical Johari Goldstein relaxation times calculated according to the CM (see section 2.3.2). Insets: β_{KWW} stretched exponent derived from the fit of the α peak as a function of pressure.

function of pressure for different temperatures (lower panel). From the VFT fits of these curves (see section 1.2.1) it is possible to calculate the glass temperature for every isobar (upper plot in Figure 8.9). As expected, the glass transition temperature is higher at higher applied pressure. From the fits of the relaxation times of the isothermal measurements (lower panel in Figure 8.9) we can calculate the glass transition pressure P_g, defined as the pressure at which the system displays a relaxation time of 100 sec (at a given fixed temperature). The obtained glass transition parameters are summarized in Table 8.1.

The fragility m, which is an indication of the deviation from the Arrhenius behaviour, has been calculated for each pressure using eq. 1.4.

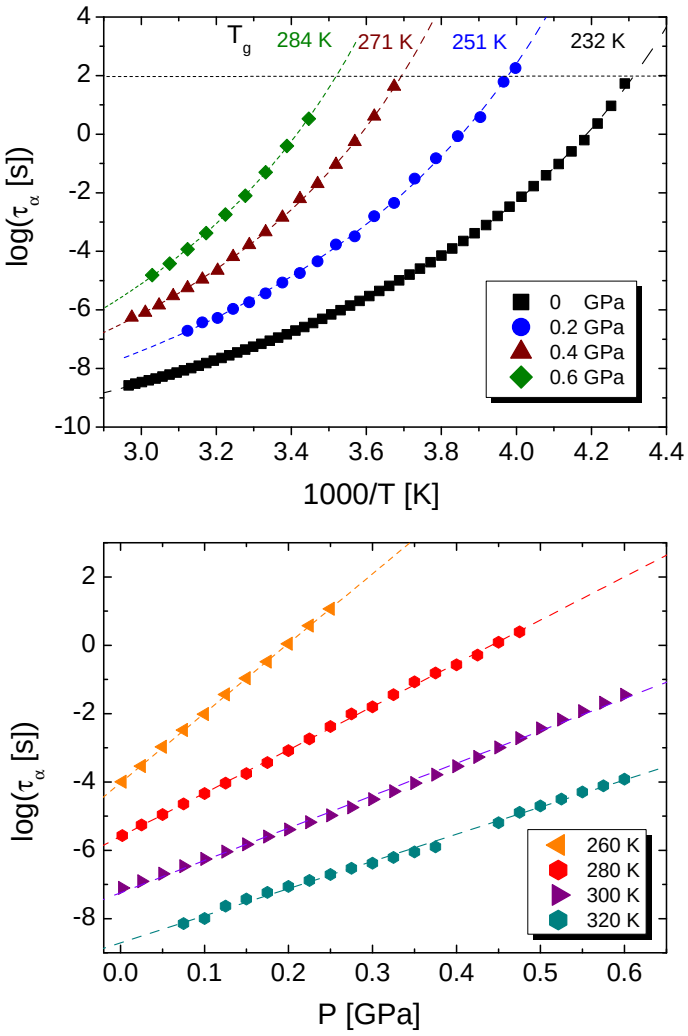

Figure 8.9: Upper panel: relaxation times of the α process as a function of the reciprocal temperature for a set of different pressures. The dotted lines correspond to the VFT fits. Lower panel: relaxation times of the α process as a function of pressure, for a set of temperatures. The dotted lines are linear fits.

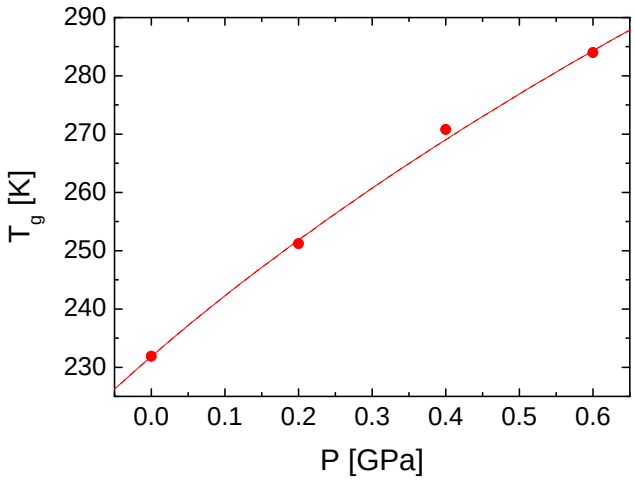

Figure 8.10: Calculated values of the glass temperature (T_g) as a function of pressure; the dotted line correspond to the fit of the data according to the Andersson and Andersson equation (eq. 1.19). Errors bars are within the size of the symbols.

The upper panel in Figure 8.11 shows the variation of the fragility as a function of pressure. Based on its relatively high m value, ternidazole can be considered as a fragile glass former. Moreover, the fragility is basically constant (decreases slightly) whit increasing pressure. This result indicates that the hydrogen bond scheme at high pressure remains almost unchanged or displays at most a slight increase of the hydrogen bond interactions, which is opposite to the usual behaviour observed e.g. for water [18] and some monohydroxy alcohols [19], where the number of hydrogen bonds is lower at higher pressure. According to the general expectation on the connection between the fragility and the cooperativity length scale ξ, the reduction of fragility is coupled to a reduction of the length scale of the dynamic heterogeneities. This hypothesis agrees with the decrease of the β_{KWW} exponent with increasing pressure (see the

inset to Figure 8.8). It should be mentioned however that some authors affirm that a correlation between fragility and cooperativity is not valid [20].

The relaxation time at constant temperature (lower panel of Figure 8.9) displays a linear pressure dependence. The activation volume $\Delta V^{\#}$ can be determined from the slope a of this graph as $\Delta V^{\#} = aRT/Log(e)$. The activation volume is lower at higher temperature (see lower panel in Figure 8.11), which implies that the free volume necessary for a molecular reorientation to occur is lower the higher the temperature, as expected.

Table 8.1 provides a summary of the values of T_g and of the fragility m as calculated from the measurements at constant pressure, and of the values of the activation volume $\Delta V^{\#}$ calculated from the measurements at constant temperature. The values of the β_{KWW} exponents, as calculated from the Cole-Davidson exponent of the fits to the α peaks, are also included in the table. The cooperativity of the α process results in a wide distribution of relaxation times as visible from the relatively small value of β_{KWW}. The more cooperative the α process, the smaller the value of the stretched exponent β_{KWW}. The shape of the α-relaxation peak for different (T, P) pairs with identical τ_α relaxation time (isochronal condition). Figure 8.12 shows that the shape of the α peak is invariant so that the β_{KWW} parameter is the same for all conditions.

We now turn to the discussion of the secondary relaxations, starting from the β process. The β relaxation has all the characteristic features of a Johari-Goldstein (JG) process. Figure 8.13 is a superplot of all the temperature- and pressure-dependent data of times of the three dynamic processes as a function of the reciprocal temperature normalized to the glass transition temperature $T_g(P)$ at the appropriate pressure value. For isobaric measurements, the horizontal scale of each Arrhenius plot was

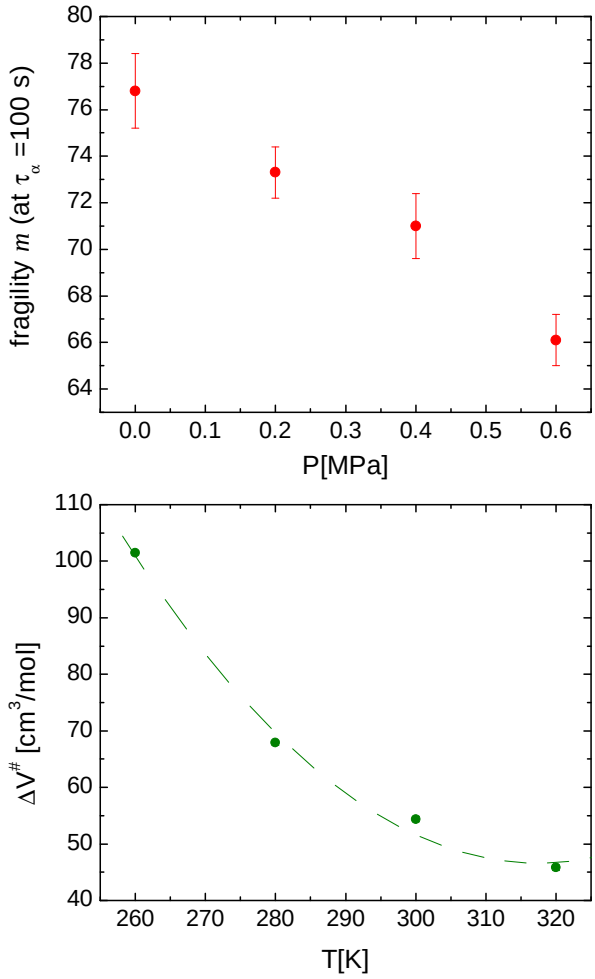

Figure 8.11: Fragility (m) as a function of pressure, calculated at $\tau_\alpha = 100$ (upper panel), and activation volume ($\Delta V^{\#}$) as a function of temperature (lower panel) for TDZ. The dotted line corresponds to a polynomial fit of the data. Errors are shown with bars in the upper panel, while for the activation volume the error bars are within the size of the symbols).

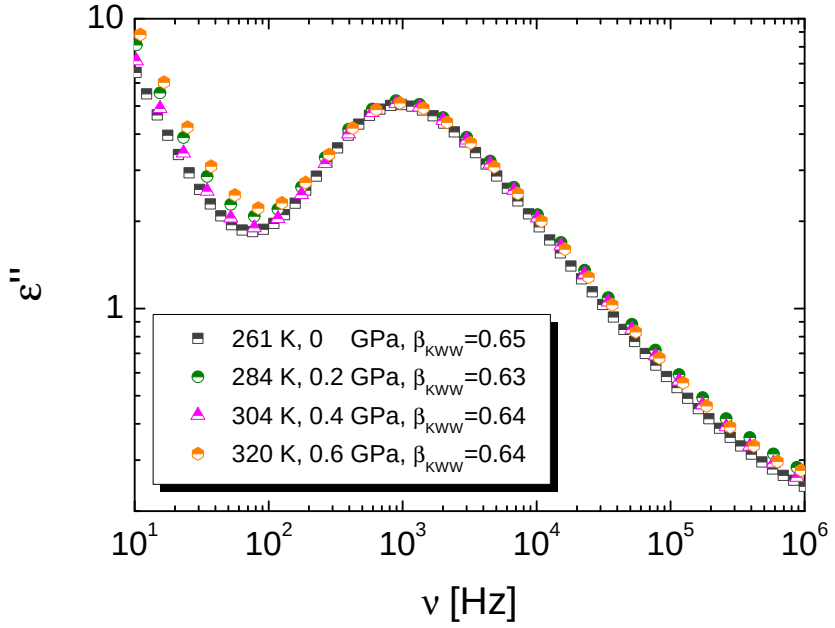

Figure 8.12: Superposed dielectric loss spectra for a set of different pressure and temperature conditions with the same τ_α relaxation time. The invariant stretched exponent β_{KWW} equals 0.64 ± 0.01 for all the spectra.

simply rescaled by the corresponding T_g. For isothermal measurements we took each point in the lower panel of Figure 8.9 and replotted it not as a function of P, but as a function of the corresponding T rescaled by the value of T_g for the given pressure. The latter was obtained from the Andersson and Andersson fit curve (eq. 1.19) to the $T_g vs. P$ curve shown in the upper panel of Figure 8.10. It may be observed from the resulting curves, displayed in Figure 8.13, that all α relaxations are superposed to one another, as are all β relaxations. This means that the separation in frequency between the α and β process is constant for all (P, T) values, that is, that the two processes have actually the same origin. In other words the β process is the JG precursor relaxation of the α process.

P [GPa]	T_g [K]	m	β_{KWW}
0	231.9 ± 0.1	76.8 ± 1.6	0.60-0.96
0.2	251.2 ± 0.2	73.3 ± 1.1	0.60-0.74
0.4	270.8 ± 0.3	71.0 ± 1.4	0.60-0.73
0.6	284.0 ± 0.2	66.1 ± 1.1	0.60-0.68
T [K]	P_g [MPa]	$\Delta V^{\#}[cm^3/mol]$	β_{KWW}
260	296 ± 1	101.5 ± 0.4	0.60-0.67
280	600 ± 5	67.9 ± 0.4	0.36-0.70
300	976 ± 13	54.4 ± 0.5	0.50-0.74
320	1397 ± 19	45.8 ± 0.5	0.50-0.76

Table 8.1: Values of the glass transition temperature (T_g) and pressure (P_g), fragility (m), activation volume ($\Delta V^{\#}$) and β_{KWW} parameter both for the measurements at constant pressure (top) and constant temperature (bottom).

This is further corroborated by comparing the fit parameters for the α and β processes with predictions of the coupling mode (CM) theory [21]. According to this theory, the β Johari-Goldstein relaxation is the primitive motion initiating the cooperative α-relaxation process in the disordered phase (in this case the supercooled liquid phase). The relation between the α-relaxation time τ_α and the β Johari-Goldstein relaxation time τ_{JG} is given by equation 2.26. The grey symbols in Figure 8.7 correspond to the τ_{JG} times calculated by means of eq. 2.26 from the experimental value of τ_α. A quantitative agreement is visible between the experimental τ_β values and the theoretical τ_{JG} times.

The Johari-Goldstein character of the β process is also confirmed by the crossover in the slope parameter of the Arrhenius plot of the β relaxation at the glass transition temperature [22, 23], which is observed

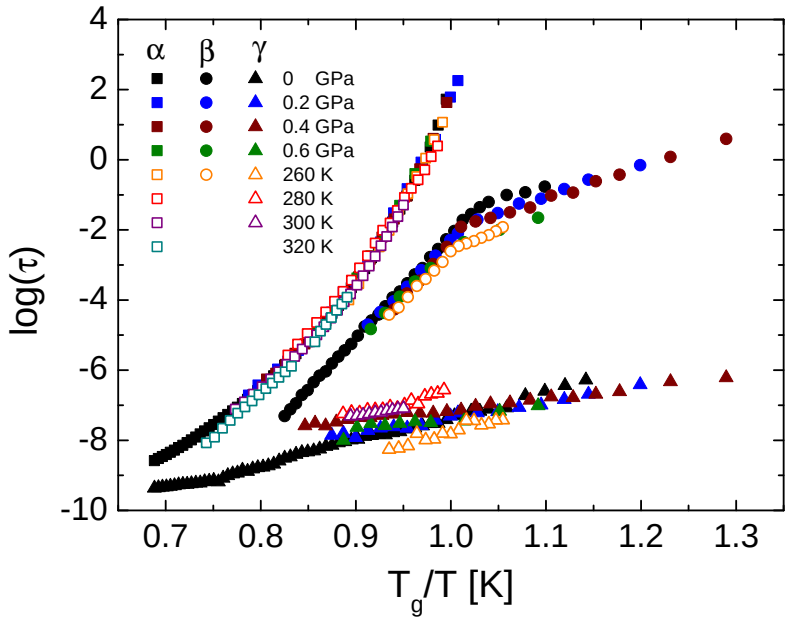

Figure 8.13: Relaxation times for the main (α), secondary Johari-Goldstein (β) and intramolecular (γ) processes as a function of the reciprocal temperature normalized by the glass transition temperature (T_g) calculated from the graph in the upper panel in in Figure 8.10 at each pressure.

for all experimental pressure values.

As for the the faster γ relaxation, it has been ascribed to an intramolecular dynamic process of the non-rigid TDZ molecules involving the propanol chain. Such intramolecular relaxation is always the fastest process whatever temperature and pressure conditions. The changes in the relaxation time of the γ process with the thermodynamic variables are not as dramatic as for the α and β processes. This γ relaxation does not obey a scaling law with the normalized temperature, as clearly visible in Figure 8.13, which shows that its origin is independent of the α and β processes [24].

As already mentioned in section 1.2.2, it is possible to provide a "thermodynamic scaling" of all the data $\tau_\alpha(T,P)$ as a function of the scaling factor $1000/TV^\gamma$, with a suitable value of the exponent γ. In order to do so it is necessary to find the equation of state $V(T,P)$ for ternidazole to calculate the volume at every pressure and temperature. This can be done by fitting the PVT measurements by means of the Tait equation (eq. 1.16). Figure 8.14 displays the specific volume of ternidazole as a function of pressure, measured at several fixed temperatures. The solid lines are the Tait equation fits (all data was fitted simultaneously). The result of the TV^γ scaling of the relaxation time data is shown in Figure 8.15, with a value of γ equal to 2±0.1. It can be seen that the β relaxation scales with the same factor used for the α relaxation, corroborating the JG origin of this secondary relaxation. On the other hand the relaxation times of the γ process are not superposed onto one another, confirming once more the intramolecular character of the fastest relaxation.

Once the assignment and dynamical map of the different relaxation processes have been settled, the crystallization dynamics at "isochronal conditions" can be studied. As isochronal condition, we considered (T_{ic},P_{ic}) thermodynamic pairs for which $\tau_\alpha \approx 0.2\ \mu s$ ($log\tau_\alpha \approx$ -6.7, see Figure 8.16). To reach such states TDZ was first heated at ambient pressure till the liquid state, pressurized to P_{ic} and then cooled down to T_{ic}. As soon as the desired thermodynamic condition was reached, the kinetics of the crystallization process was followed by measuring the dielectric permittivity, both real (ε') and imaginary (ε'') parts, as a function of time within the frequency range $10^2 - 10^7$ Hz. An example of spectral sequence corresponding to the recrystallization process is shown in Figure 8.17.

During the crystallization process, the number n_D of reorientating dipoles decreases with time and therefore the dielectric strength $\Delta\epsilon$ of the

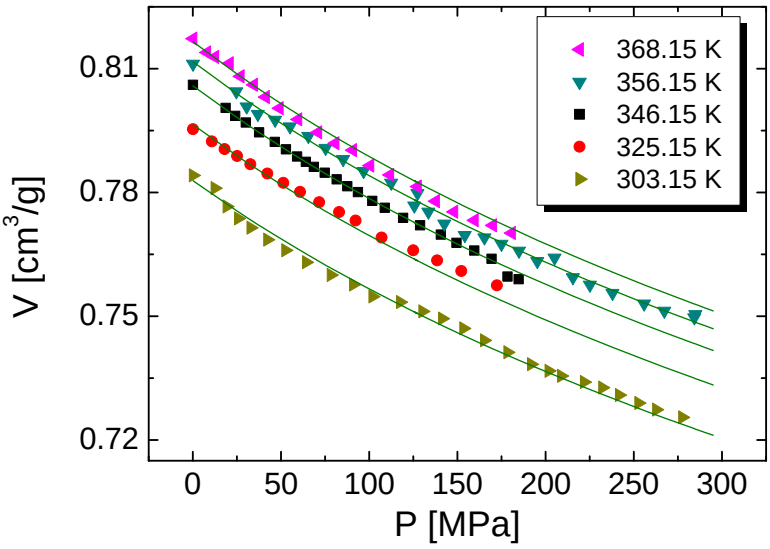

Figure 8.14: Volume measurements as a function of pressure at fixed values of the temperature (PVT measurements) for ternidazole. The solid lines correspond to the Tait equation used to fit all the data simultaneously.

α-relaxation process must also decrease in time (since $\Delta\epsilon \propto n_D\mu^2$). This is reflected in the reduction of the static permittivity increment in the real part of the dielectric permittivity (upper panel in Figure 8.17), and in a decrease of the intensity of the α peak in the imaginary part (lower panel in Figure 8.17). During the crystallization process the position of the relaxation peak moved slightly towards higher frequencies. For this reason the crystallization of ternidazole is better studied by considering the time evolution of the real part of the dielectric permittivity ($\varepsilon'(t)$) taken at a fixed value of frequency (corresponding at approx. 10^5 Hz). The behaviour of $\varepsilon'(t)$ is shown in Figure 8.18 for all the (T_{ic},P_{ic}) thermodynamic pairs under investigation. We can observe that the dielectric constant starts to decrease only after a certain time t_0: this is the so-called induction

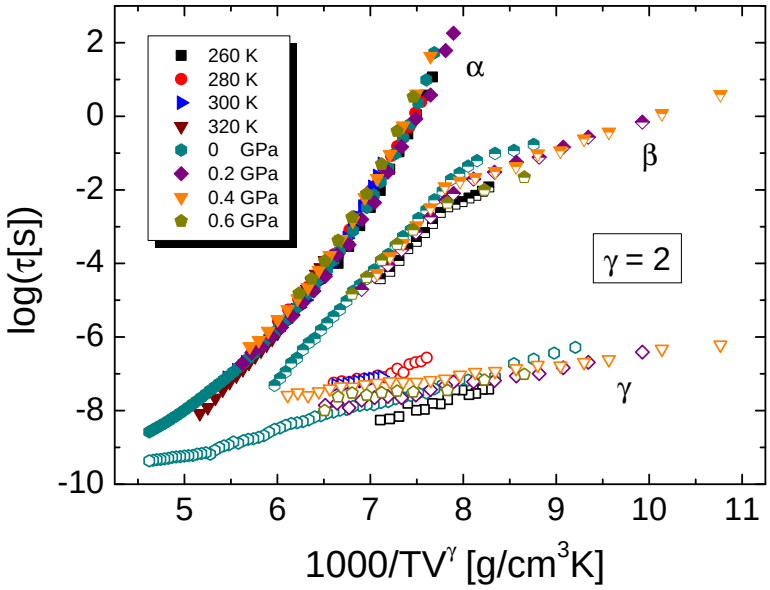

Figure 8.15: Thermodynamic scaling of the relaxation times for the α, β and γ processes as a function of the scaling quantity $1000/TV^{\gamma}$.

time of crystallization. If the crystallization onset were determined only by the molecular mobility of the α process (which is the same in all three cases) one would expect to find almost the same induction time. Instead t_0 is found to decrease with increasing pressure and temperature values (see Table 8.2), which means that the molecular mobility is not the sole responsible of the crystallization onset. To study the crystallization kinetics, a "normalized" dielectric constant is used [25]:

$$\varepsilon'_N(t) = \frac{\varepsilon'(0) - \varepsilon'(t)}{\varepsilon'(0) - \varepsilon'(\infty)} \tag{8.1}$$

where $\varepsilon'(0)$ is the value of the dielectric constant at the crystallization onset, $\varepsilon'(\infty)$ is the value at the end of the crystallization process and $\varepsilon'(t)$ is the dielectric constant at a time t in between. The normalized dielectric permittivity is shown in Figure 8.19(a) as a function of time. We

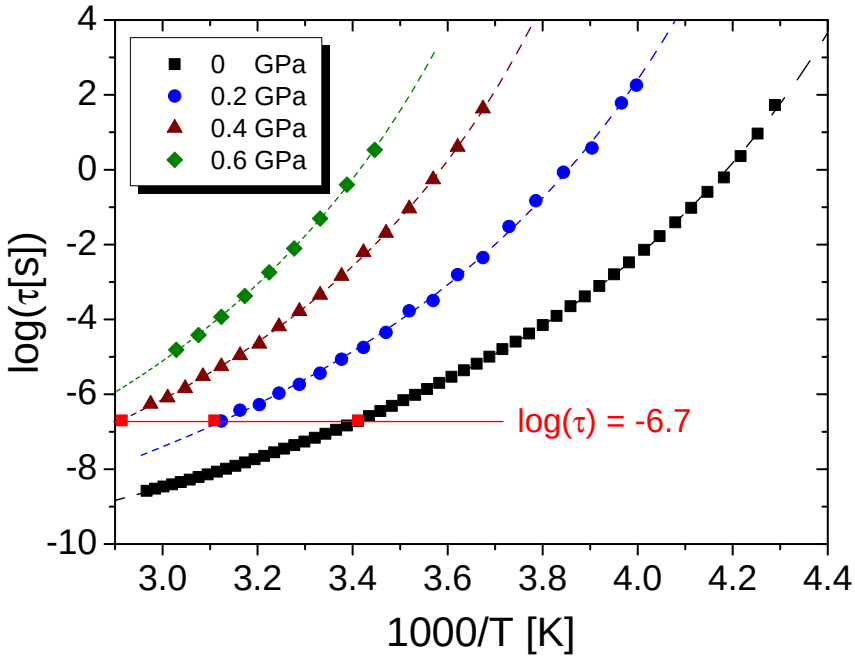

Figure 8.16: Relaxation map of the α process of ternidazole: the red squares indicates the values of (T_{ic}, P_{ic}) that corresponds to the value of $log\tau_\alpha \approx$ -6.7, at which the crystallization process was studied.

observe that the experimental curves shift to shorter times when P and T are increased, as reported also for 5-methyl-2-[(2-nitrophenyl)amino]-3-thiophenecarbonitrile [7] and indomethacin [8], but contrary to what is reported for ibuprofen [10]. Thus, at the moment there is no a general trend that describes the crystallization kinetics of supercooled liquids at different thermodynamic conditions with the same structural relaxation time.

The time dependence behaviour of the normalized $\varepsilon'_N(t)$ can be described by using the Avrami equation [26, 27]:

$$\varepsilon'_N(t) = 1 - exp[-k(t - t_0)^n] \tag{8.2}$$

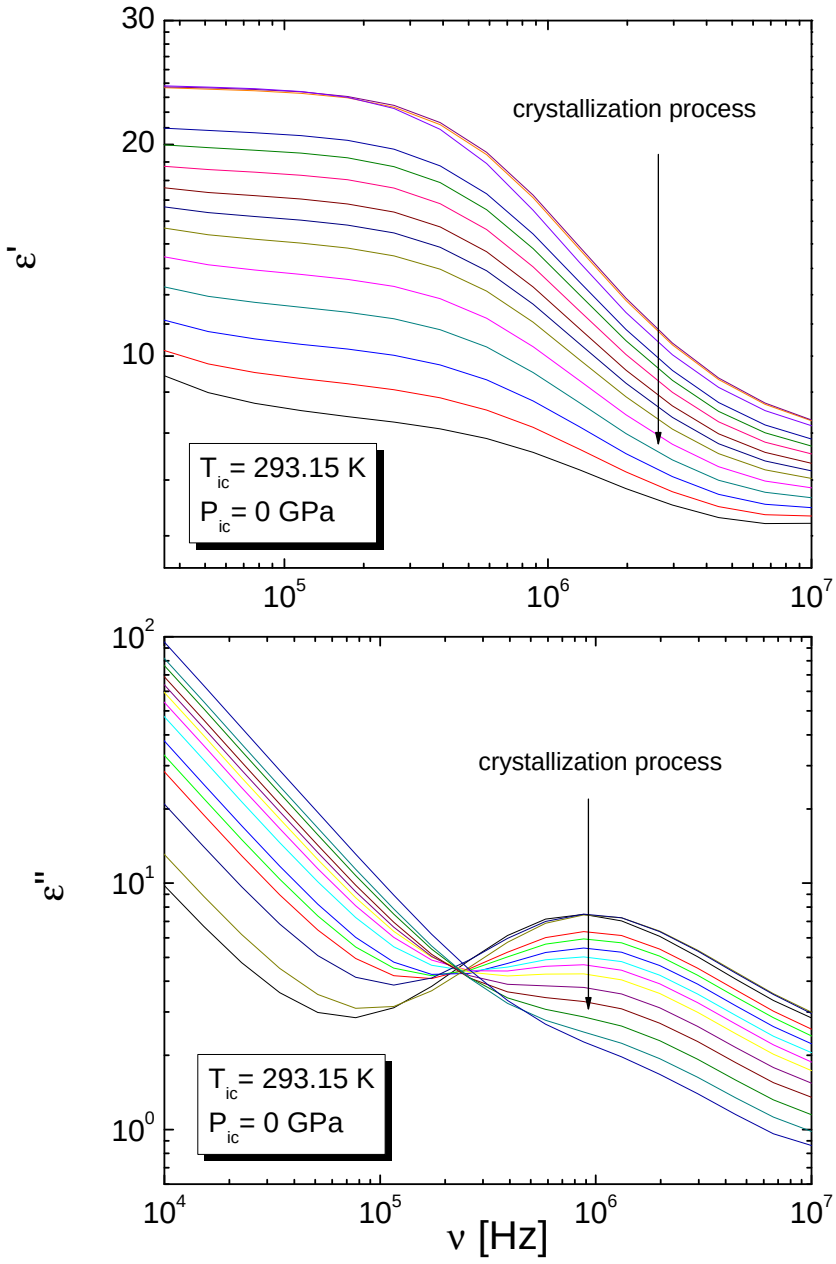

Figure 8.17: Examples of spectra of the real ε' (upper panel) and imaginary ε'' (lower panel) part of the dielectric permittivity of ternidazole during the crystallization at a temperature of 293.15 K and at ambient pressure.

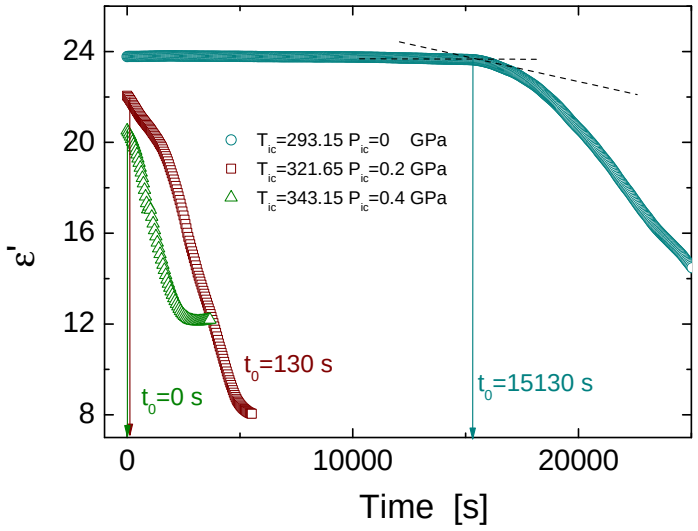

Figure 8.18: Time evolution of the real part of the dielectric permittivity at the fixed frequency value of 10^5 Hz during the crystallization process for the (T_{ic},P_{ic}) thermodynamic pairs. The arrows marks the induction time of the crystallization in each (T_{ic},P_{ic}) condition.

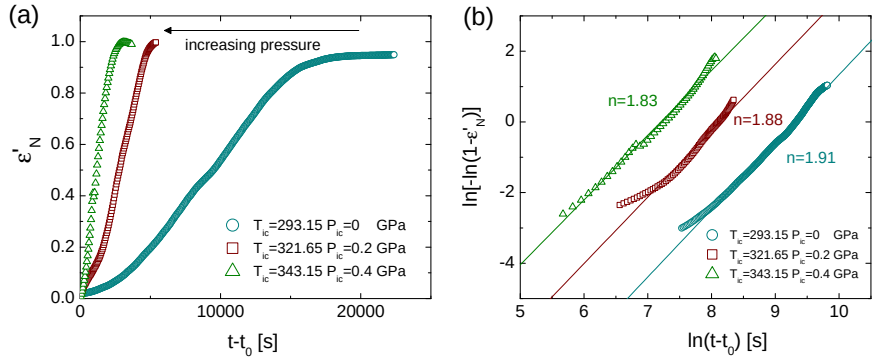

Figure 8.19: (a) Normalized dielectric permittivity $\varepsilon'_N(t)$ as a function of time for three (T_{ic},P_{ic}) thermodynamic states. (b) Avrami plot of the normalized dielectric permittivity $\varepsilon'_N(t)$; the solid lines represents fits using the Avrami equation 8.2.

T_{ic} (K)	P_{ic} (GPa)	t_0 (s)	n	lnk	$k^{1/n}$ (s^{-1})	V (cm^3/g)	$\Delta\mu$ (kJ/mol)
293.15	0	15130	1.91	-17.75	$1.96 \cdot 10^{-8}$	0.78	4.1
			±0.01	±0.07			
321.65	0.2	130	1.88	-15.29	$2.29 \cdot 10^{-7}$	0.75	3.4
			±0.03	±0.22			
343.15	0.4	0	1.83	-13.20	$1.85 \cdot 10^{-6}$	0.73	2.8
			±0.03	±0.18			

Table 8.2: Values of the crystallization induction time t_0, the Avrami parameters n and lnk, the crystallization rate $k^{1/n}$, the specific volume of the supercooled liquid V and the chemical potential $\Delta\mu$ for the crystallization process of ternidazole at different (T_{ic},P_{ic}) thermodynamic states.

where k is called "rate constant" and n is the Avrami exponent, which depends on the crystal morphology and crystallization mechanism [28]. From the plot of $ln[-ln(1-\varepsilon'_N(t))]$ versus $ln(t-t_0)$ it is possible to obtain the value of lnk as the intercept, and n as the slope, of the linear fit of the plot (see Figure 8.19(b)). The obtained parameters are summarized in Table 8.2.

In line with the lowering of the induction time with increasing pressure, the value of the crystallization rate $k^{1/n}$ increases by increasing the applied pressure. The value of the Avrami exponent n is not changing significantly under different thermodynamic conditions, which suggests that the shape of the growing crystallites is the same in all three cases. The value of n=2 indicates an athermal nucleation with a three-dimensional crystal growth. The crystals grow as truncated spheres, as shown in ref. [1].

From the Tait equation of state V(T,P) it is also possible to calculate the specific volume of the supercooled liquid at the (T_{ic},P_{ic}) conditions.

The result is that the volume decreases (*i.e.* the density increases) by increasing pressure. The calculated values are summarized in Table 8.2. Since the specific volume of the crystal (not shown) is not changing significantly with the pressure, the relative specific volume (i.e., the difference between the specific volume of the crystal and the supercooled liquid) is proportional to the specific volume of the supercooled liquid and, as expected, it is lower when the crystallization is faster.

We can analyse the effect of pressure on the crystallization rate at isochronal conditions by studying the chemical potential difference ($\Delta\mu$) between the liquid and the crystal phases, which is a thermodynamic driving force of crystallization. By definition it is:

$$d(\Delta\mu) = -\Delta S dT + \Delta V dP \tag{8.3}$$

In our case, the second term in eq. 8.3 is always zero because we want to calculate the chemical potential of the crystallization process at constant pressure.

By integrating, at $P = P_0$ from the melting temperature T_m to a generic temperature T one obtains the following formula for the chemical potential [29]:

$$\Delta\mu(T,P) = -\int_{T_m}^{T} \Delta S(T,P_0)dT \tag{8.4}$$

ΔS, which corresponds to the entropy difference between the crystal and the liquid phases, can be found from the Clausius-Clapeyron equation $dP/dT = \Delta S/\Delta V$, by knowing the pressure behaviour as a function of temperature as $P(T) = B_1T + B_2$ (B_1 and B_2 fitting constants). In the Clausius-Clapeyron expression $\Delta V = V_{liq} - V_{cry}$ is the volume difference between the crystal and the liquid phases and its behaviour, as a function

of pressure, can be determined from the PVT measurements across the melting transition (not shown). The obtained values for the chemical potential are reported in Table 8.2. The chemical potential difference decreases with increasing pressure, implying that the thermodynamic force driving crystallization diminishes with pressure. This result contrasts with the fact that on increasing pressure the crystallization kinetics is faster. However, there are too many parameters to be considered in the thermodynamic equations of nucleation and crystal growth [8] to be able to explain this inconsistency.

8.5 Conclusions

The dynamics of the supercooled ternidazole drug has been studied as a function of temperature and pressure. A primary (α) relaxation is observed followed by two secondary (β and γ) relaxations. By measuring the volume changes and the glass transition temperature T_g as a function of pressure, the non-equilibrium phase behaviour and the equation of state of TDZ have been determined experimentally. This information is used to obtain two masterplots of the relaxation times obtains at all studied (T,P) conditions, one versus the temperature normalized to T_g, and the other versus the thermodynamic scaling parameter TV^{γ}. From both masterplots we conclude that the β relaxation has the cooperative character proper of the JG relaxations, while the faster γ relaxation corresponds to an intramolecular process associated with the propanol chain motions. The γ scaling parameter is found to be equal to 2 ± 0.1.

By considering isochronal conditions, it is possible to study the effect of pressure on the crystallization kinetics. We found that increasing the pressure speeds up the crystallization process. This could be do to

the decrease in the relative specific volume (increase of the density) of the system upon increasing pressure and temperature under isochronal conditions.

Bibliography

[1] P. Negrier, M. Barrio, J. L. Tamarit, D. Mondieig, M. J. Zuriaga, and S. C. Perez *Cryst. Growth Des.*, vol. 13, p. 2143, 2013.

[2] J. Lu and S. Rohani *Org. Process Res. Dev.*, vol. 13, p. 1269, 2009.

[3] A. Saleki-Gerhardt, J. G. Stowell, S. R. Byrn, and G. Zografi *J. Pharm. Sci.*, vol. 84, p. 318, 1995.

[4] G. Q. Lu, E. Nygren, M. J. Aziz, D. Turnbull, and C. W. White *Appl. Phys. Lett.*, vol. 54, p. 2583, 1989.

[5] G. Devaud, M. J. Aziz, and D. Turnbull *J. Non-Crystal. Solids*, vol. 109, p. 121, 1989.

[6] D. R. Uhlman, J. F. Hays, and D. Turnbull *Phys. Chem. Glasses*, vol. 7, p. 159, 1966.

[7] K. Adrjanowicz, K. Kaminski, M. Paluch, N. K. L., and Y. Lian *J. Chem. Phys.*, vol. 136, p. 234509, 2012.

[8] K. Adrjanowicz, A. Grzybowski, K. Grzybowska, J. Pionteck, and M. Paluch *Cryst. Growth Des.*, vol. 13, p. 4648, 2013.

[9] K. Adrjanowicz, A. Grzybowski, K. Grzybowska, J. Pionteck, and M. Paluch *Cryst. Growth Des.*, vol. 14, p. 2097, 2014.

[10] K. Adrjanowicz, A. Grzybowski, K. Kaminski, and M. Paluch *Mol. Pharmaceutics*, vol. 8, p. 1975, 2011.

[11] N. Mahé, M. A. Perrin, M. Barrio, B. Nicolaï, I. B. Rietveld, J. L. Tamarit, and R. Céolin *J. Pharm. Sci.*, vol. 100(6), p. 2258, 2011.

[12] M. W. Miller, H. L. Howes Jr., R. V. Kasubick, and A. R. English *J. Med. Chem.*, vol. 13(5), p. 849, 1970.

[13] L. Jokipii and A. M. Jokipii *Antimicrob. Agents Chemother.*, vol. 28(4), p. 561, 1985.

[14] A. D. Bond *CrystEngComm*, vol. 10, p. 411, 2008.

[15] M. Kubicki, T. Borowiak, G. Dutkiewicz, M. Souhassou, C. Jelsch, and C. Lecomte *J. Phys. Chem. B*, vol. 106, p. 3706, 2002.

[16] M. Kubicki *J. Mol. Str.*, vol. 743, p. 209, 2005.

[17] N. M. Blaton, O. M. Peeters, and C. J. De Ranter *Acta Cryst.*, vol. B35, p. 2465, 1979.

[18] P. H. Poole, F. Sciortino, T. Grande, H. E. Stanley, and C. A. Angell *Phys. Rev. Lett.*, vol. 73, p. 1632, 1994.

[19] S. Pawlus, M. Paluch, and M. Dzida *Phys. Chem. Lett.*, vol. 1, p. 3249, 2010.

[20] L. Hong, V. N. Novikov, and A. P. Sokolov *J. Non-Cryst. Solids*, vol. 357, p. 351, 2011.

[21] K. L. Ngai *Phys. Rev. E*, vol. 57, p. 7346, 1998.

[22] S. Capaccioli, D. Prevosto, M. Lucchesi, S. Sharifi, and P. A. Rolla *J. Phys. Chem. B*, vol. 112, p. 4470, 2008.

[23] M. Mierzwa, S. Pawlus, M. Paluch, E. Kaminska, and K. L. Ngai *J. Chem. Phys.*, vol. 128, p. 044512, 2008.

[24] E. Kaminska, K. Kaminski, M. Paluch, and K. L. Ngai *J. Chem. Phys.*, vol. 124, p. 164511, 2006.

[25] A. D'Amore, J. M. Kenny, L. Nicolais, and V. Tucci *Polym. Eng. Sci.*, vol. 30, p. 314, 1990.

[26] M. Avrami *J. Chem. Phys.*, vol. 17, p. 1103, 1939.

[27] M. Avrami *J. Chem. Phys.*, vol. 8, p. 212, 1940.

[28] B. Wunderlich, *Macromolecular physics, Vol. 2, Crystal nucleation, growth, annealing.* New York: Academic Press, 1976.

[29] I. Gutzow, B. Durschang, and C. Rüssel *J. Mater. Sci.*, vol. 32, p. 5389, 1997.

CONCLUSIONS

In this thesis we study the effect of pressure and temperature on the dynamic processes characteristic of several pure compounds and binary mixtures forming structural or orientational glasses. Structural glasses are non-equilibrium states derivating from the cooling down of a liquid phase, which therefore display in general a tendency to crystallize into an ordered state. On the other hand, orientational glasses are formed by the freezing of molecular motions in plastic crystals, which are translationally ordered solids whose consituent molecules exhibit rotational motions. Plastic crystals are often the equilibrium phase between the liquid and a fully ordered, perfectly crystalline phase at low temperature.

From the comparison of the results obtained for all the compounds and mixtures under investigation we can conclude that in all cases a primary α relaxation is present, associated with the collective motion of the molecules, which freezes out at the so-called glass transition temperature. In most cases there are also other relaxation processes, usually less cooperative than the alpha process, which are referred to as "secondary relaxations". While the nature of the collective α process can be confirmed by carrying out a calorimetry study, the origin of these secondary processes is not unique and depends on the characteristics of the material under examination.

For example, we studied the dynamics as a function of temperature and pressure of a pharmaceutical drug, ternidazole. A primary (α) relaxation is observed followed by two secondary (β and γ) relaxations. The β relaxation has the cooperative character proper of a "precursor" primitive relaxation (usually called Johari-Goldstein relaxation), while the faster γ relaxation corresponds to an intramolecular process associated with the propanol chain motions. In this compound we also studied the effect of pressure on the crystallization kinetics under isochronal conditions and found that increasing the pressure speeds up the crystallization process. This effect might be due to the increase of the density of the system upon increasing pressure and temperature under isochronal conditions.

In two chapters of the thesis we focus on the solid phases of benzene derivatives containing polar or methyl sidegroups, namely the bis-substituted fluoroaniline and xylene derivatives, and the hexasubstituted pentachloronitrobenzene molecule. We have probed the molecular dynamics in mixtures of m-fluoroaniline (mFA) (which possesses H-bonding groups) with m-xylene (mX) (which does not). The increase of the m-xylene molar fraction results in a shorter relaxation time (faster dynamics) of the collective α relaxation of the mixture, indicating weaker intermolecular interactions and the reduction of the size of the H-bonded m-fluoroaniline clusters contributing to the relaxation process. At m-xylene content bigger than 60%, the mixtures have a strong tendency to crystallize, phase-separating into amorphous mFA-rich and crystalline mX-rich domains. The collective relaxation of the mFA-rich phases are consistent with a local mX concentration between 10% and 30%. All mixtures display a secondary relaxation with almost the same activation energy. The characteristic times are close to those of pure mFA for homogeneous mixtures, while for phase-separated samples they are smaller

by two decades. The constancy of the activation energy (also compared to pure mFA) suggests that the microscopic origin of the secondary process is always the same and is related to local dynamics involving the hydrogen bonds formed by mFA molecules. The slower β dynamics in phase-separated samples is likely due to mFA molecules trapped in mX-rich crystallites.

In the case of the low-dimensional disordered orientational glass formed by pentachloronitrobenzene, the dynamics reveals two primary relaxation processes very close in time scale, which we attribute, respectively, to the in-plane reorientational 60°-jumps of the molecules within the (001) plane of a rhombohedral lattice, and to tilting motions outside such plane, which results in a relaxation process involving the dipole component orthogonal to the planes.

We have studied the cooperative dynamics in mixed plastic crystals formed by two tetrahedral molecules, neopentyl alcohol and neopentyl glycol. By means of a derivative-based analyses, we have shown that the Cohen-Grest and the Vogel-Fulcher-Tamman equations, often used to describe the temperature dependence of the α relaxation time, fail to give a proper description of the data. Instead, the so-called Dynamic-Scaling Model (DSM), which describes the glass transition in terms of a critical-like behaviour (as in a real thermodynamic phase transition) is able to fully account for the temperature dependence of the primary relaxation time. In particular, the analysis indicates a power-law behaviour with exponent close to the DSM universal exponent $g = 9$. A ("critical"-like) exponent equal or close to 9 seems to be a general property of phases with only one kind of disorder (*e.g.*, translational for liquid crystals and orientational for plastic crystals). The perfect agreement with the DSM predictions allows determining the correlation length of the cooperative

rearranging regions for orientational disordered phases. The obtained correlation length is comparable with the lattice parameter of the high-symmetry unit cell (< 1 nm), so that the cooperative (α) dynamics should be thought of as corresponding to short-range fluctuations.

Finally, we have studied the dielectric response of the globular, cage-like 2-adamantanone molecule. This molecule forms, at low temperature, an orientationally-ordered metastable phase exhibiting an intrinsic statistical disorder involving the site occupancy of the carbonyl moiety of the molecule. Our dielectric study evidences the existence of an α relaxation, originating from strongly correlated large-angle dipole fluctuations of groups of molecules, and of a corresponding primitive (Johari-Goldstein) β relaxation, which could be analysed successfully in the theoretical framework of the so-called Coupling Model. The emergence of a glassy-like, double ($\alpha - \beta$) dynamics even in an "ordered" system is a surprising result and opens the way to further studies of non-conventional cooperative relaxation dynamics.

List of Publications

- M. Romanini, J. C. Martinez-Garcia, J. Ll. Tamarit, S. J. Rzoska, M. Barrio, L. C. Pardo, and A. Drozd-Rzoska, "Scaling the dynamics of orientationally disordered mixed crystals", *J. Chem. Phys.* 131, 184504 (2009)

- M. Romanini, Ph. Negrier, J. Ll. Tamarit, S. Capaccioli, M. Barrio, L. C. Pardo, and D. Mondieig, "Emergence of glassy-like dynamics in an orientationally ordered phase", *Phys. Rev. B* 85, 134201 (2012)

- P. Negrier, M. Barrio, M. Romanini, J. Ll. Tamarit,, D. Mondieig, A. I. Krivchikov, L. Kepinski, A. Jezowski, and D. Szewczyk, "Polymorphism of 2-Adamantanon", *Cryst. Growth Des.* 14, 2626 (2014)

- M. Romanini, M. Barrio, S. Capaccioli, M. D. Ruiz-Martin, R. Macovez and J. Ll. Tamarit, "Double primary relaxation in a highly anisotropic orientational glass-former with low-dimensional disorder", submitted to *J. Phys. Chem. Lett.*

- M. Romanini, S. Capaccioli, R. Macovez, M. Barrio and J. Ll. Tamarit, "Dynamics as a function of temperature and pressure for drug 3-(2-methyl-5-nitroimidazol-1-yl)-propan-1-ol", to be submitted.

- M. Romanini, S. Capaccioli, R. Macovez, M. Barrio and J. Ll.

Tamarit, “Suppression of hydrogen-bond-induced clusters in m-fluoroaniline by mixing it with m-xylene”, in preparation.

Acknowledgements

It has been a long trip and now that I'm at the end of it I would like to thank all the people that I crossed path with during these years and those who helped me expand my knowledge in the scientific world.

Great thanks to Josep Lluis and Maria, the supervisors of my thesis, for taking me as PhD candidate, for teaching me how to perform experiments and work in a laboratory and for giving me a lot of freedom to carry out my research. Thanks for giving me the opportunity to continue working longer in the group, and of course, also for their friendship.

I thank Dr. Peter Lunkenheimer for hosting me in his laboratory in Augsburg where I started understanding what dielectric spectroscopy is all about.

Thanks to Simone, for inviting me to carry out experiments in his laboratory in Pisa, for teaching me a lot of things and answering all my doubts and questions. You have been and are, to me, a friend and not only a scientifically knowledgeable person to collaborate with.

To all the GCM members, the old ones, the new ones and the ones that just stayed briefly during these years: thanks for your friendship, the chats, the coffees, the beach camping, the barbecues (or the "asados" as someone would say!) and for all the fun inside and outside the lab.

Alla mia famiglia, lontana ma sempre nel mio cuore. A papá, mamma,

Matteo e Martina: é difficile raggiungere tanti obiettivi e non avervi sempre vicino a me per festeggiarli.

A Roberto, un compagno meraviglioso, grazie per essere sempre pronto a sostenermi e incoraggiarmi e per essere uno splendido papá per il nostro cucciolo. E grazie anche per il duro lavoro di revisione della tesi che ti ho "costretto" a fare.

E a Leonardo, il mio piccolo tesoro, semplicemente grazie per essere il meraviglioso bimbo che sei, per riempire le mie giornate di pura felicitá (assieme al tuo papi che altrimenti si ingelosisce) e per farmi ridere come nessuno sa fare, il piú delle volte senza essere consapevole di farlo.